⬛ NTNU
Norwegian University of
Science and Technology

TEM characterization of GaAs/GaAsSb heterostructured nanowires for laser applications

Ingrid Marie Andersen

Abstract

III-V type semiconductor nanowires (NW) are currently subjects of high interest due to their unique optoelectronic properties and the prospect of further miniaturization, integration and optimization of optoelectronical devices, such as LEDs, in the future. In this study, the structure of self-catalyzed GaAs NWs (length ~10 μm and thickness ~400 nm) with six GaAsSb/GaAs superlattices (SL), have been analyzed. Four samples with varying Sb flux and GaAsSb well growth time, which all depicted lasing when optically pumped, were studied by conventional transmission electron microscopy. Crystal phase analysis has been done by dark-field imaging, and compared to high-resolution lattice images. The aim of this work was to quantify the crystal phases in the different NWs for all the SLs and link the findings to the growth conditions and observed lasing. The sample with the lowest Sb flux has a very high stacking fault density along the entire NW, and phase distribution is not further analyzed. The spacers between SLs are wurtzite (WZ) GaAs, and the SLs consist of defect-free zinc-blende (ZB) phase segments separated by regions of high stacking fault density and mixed phases (ie. twinned ZB, stacking faults and in cases WZ). When considering crystal phase, SL-3, -4 and -5 are quite similar, while SL-6 is in general shorter than other SLs. The ZB segments become larger and more stable, mixed phase regions reduce in size, over all stacking fault density goes down and the amount of defect-free WZ phase increases with Sb concentration. In addition, some specific structural features have been observed; SL-1 has quantum dot-like features, the NW tips have distinct facet planes, and one sample has surface damage from oxidation of the AlGaAs shell due to incomplete, or absence of, the GaAs protective cap. The structural characterization carried out in this work helps to understand the observed lasing behavior and compositional analysis from other studies on the same NW batches. Together these findings can contribute to optimize the growth of NWs with GaAs/GaAsSb SLs and the understanding as well as performance of NW-based lasers based on these heterostructures.

Cover image: False color image (RGB) of a GaAs/GaAsSb superlattice in a self-catalyzed GaAs nanowire. Blue is wurtzite, red and green are two different orientations of the zinc blende.

Sammendrag

III-V type halvleder nanotråder (NT) får om tiden mye oppmerksomhet grunnet deres unike optoeletroniske egenskaper, samt potensialet for ytterligere forminsking, integrering og optimering av optoelekronisk utstyr, slik som LED, for fremtiden. I denne studien har selvkatalyserte GaAs NTer (lengde ~10 μm, tykkelse ~400 nm) med seks GaAsSb/GaAs supergittere (SG), blitt analysert strukturelt. Fire prøver med varierende Sb-fluks og GaAsSb brønngrotid, som alle har påvist laserevne under optisk pumping, har blitt studert ved konvensjonell transmisjons elektronmikroskopi. Krystallfaseanalyse har blitt utført ved bruk av mørkefeltsavbilding, og sammenlignet med høyoppløsningskrystallgitterbilder. Målet med denne avhandlingen var å kvantisere krystallfasene for alle SGere i de forskjellige NTene og knytte funnene opp mot vekstbetingelser og observerte laseregenskaper. Prøven med lavest Sb fluks har relativt høy stablefeiltetthet langs hele NTen, og krystallfasedistribueringen dermed ukjent. Segmentene som skiller SGene er wurtzite (WZ) GaAs, og SGene består av defektfrie zinc-blende (ZB) krystallfasesegmenter, separert av områder med høy stablefeiltetthet og blandede krystallfaser (ie. twinned ZB, stablefeil og noen ganger WZ). Krystallfasemessig er SG-3, -4 og -5 veldig like. ZB segmentene blir lengre og mer stabile, blandede krystallfaseregioner blir kortere, stablefeiltettheten minsker og mengden defektfri WZ krystallfase øker ved økt Sb-konsentrasjon. I tillegg har noen spesifikke strukturelle trekk blitt observert; SL-1 viser quantum dot-aktige trekk, tuppen av NTene har destinkte overflateplan, og en av prøvene har overflateskader fra oksidering av AlGaAs-skallet grunnet utilstrekkelig dekke av beskyttende topplag. Den strukturelle karakteriseringen utført i dette studiet bidrar til forståelse av observerte laseregenskaper og den kompositoriske analysen utført i andre studier av samme NTpartiene. Sammenlagt vil disse funnene bidra til vekstoptimaliseringen av NTer med GaAs/GaAsSb SGe, og dermed også til å øke forståelsen og prestajonen av denne typen SG-baserte lasere.

Preface and Acknowledgement

This master thesis work is part of the 5 year study program "Teacher Education with Master of Science" (LUR), with specialization in Physics and Mathematics, at the Norwegian University of Science and Technology (NTNU). The study has been carried out at the TEM Gemini Center in the Department of Physics (IFY). The experimental work was done part-time during the academic year of 2016/2017 under the supervision of Prof. dr. A.T.J. van Helvoort. The NWs studied in this work are grown in the MBE lab at NTNU by PhD candidate Dingding Ren. All experimental work and writing has been done by the author, unless explicitly stated otherwise.

First of all, let me thank my supervisor for always finding a spot for me in his ever tighter schedule. Ton, thank you for our discussions, for joining me during sessions on the microscope, and for all the help and feedback you have given during this year. Your passion for the field is contagious, and has inspired and motivated me throughout this process. I have learned a lot from you. I could never have wished for a better advisor.

I would also like to thank PhD candidate Dingding Ren. First of all for providing the NWs and teaching me the sample preparation steps, but also for many interesting discussions in Ton's office. Thank you for giving me feedback, and for answering my emails even during weekends.

Finally, I would like to thank my friends and family for always believing in me.

I hereby declare this an independent work in accordance with the regulations of the Norwegian University of Science and Technology.

Trondheim, 2017-06-01

Ingrid Marie Andersen

Acronyms

AlGaAs Aluminium gallium arsenide

BF Bright-field

BG Bandgap

DF Dark-field

DP Diffraction pattern

ESF Extrinsic stacking fault

FCC Face centered cubic

FP Fabry-Pérot (cavity)

GaAs Gallium arsenide

GaAsSb Gallium arsenide antimonide

HCP Hexagonal close-packed

HR High resolution

ISF Intrinsic stacking fault

LASER Light amplification by stimulated emission of radiation

LED Light emitting diode

MBE Molecular beam epitaxy

MD Misfit dislocations

NW Nanowire

OLTF Optical lens transfer function

QW Quantum well

SAED Selected area electron diffraction

SF Stacking fault

SL Superlattice

SPED Scanning precession electron diffraction

TP Twin plane

TEM Transmission electron microscope

VLS Vapour-liquid-solid

WPOA Weak phase-object approximation

WZ Wurtzite

ZB Zinc blende

Contents

Chapter 1

Introduction and motivation

The nanowire (NW) structure has been predicted to be the base for the future for nanoscale devices, with applications for devices such as LEDs[1], solar cells [2, 3], transistors [4] and lasers [5, 6, 7]. With an exponential increase of published papers on the topic, NWs have become one of the most researched areas of the 2000's within the field of nanotechnology [8]. Their small volume, well defined geometry, relaxed growth substrate lattice matching and superb strain tolerance allows for the integration of direct bandgap III-V semiconductors to Si-based technologies. So many of these unique and desirable properties make scientists interested in III-V NWs for developing the integrated optical devices of tomorrow [9].

The use of semiconductor NWs for laser applications is a hot topic in today's nano-research community, as they can offer improved, i.e. defect-free single crystal phases and atomically smooth surfaces compared to planar thin films and heterostructures [8]. One of the most attractive properties that makes the NW lasers so intriguing is that they would offer high intensity coherent light sources for a broad range of applications in fields ranging from health to communication. Through size (confinement effects) or composition alterations the wavelength can be tuned. The growth of a semiconductor heterostructure within NWs is one such way, where lasing of a variation of wavelengths have been reported by the implementation of single or multiple radial quantum wells [10, 11, 12]. However, nanowire lasers are a relatively new concept, and futher studies regarding the growth control and lasing mechanisms are still required understand and optimize structure design and fabrication of semiconductor NWs for laser application.

The Nanowire group at NTNU (Weman/van Helvoort/Fimland) has recently developed su-

perlattice (SL) structured nanowires that have exhibted lasing abilities [13]. The group has so far studied the lasing properties and compositional variations within these heterostructured NWs (see Appendices D and E), but the crystal structure was not yet systematically studied. As the crystal phase (i.e. structure can be either zinc-blende (ZB) or wurtzite (WZ), with different types of stacking faults) affects the material bandgap, this will directly affect the lasing properties of the NWs. The crystal phase can be controlled by the NW growth conditions [14]. In general, for planar optoelectronic devices, the external efficiency and pumping efficiency is strongly dependent on the defect density and thus defect-free crystal phases are desired [15, 16]. Mapping of crystal phases, WZ and ZB, and the defect density of the NWs is thus of interest to better understand the lasing properties of NWs grown under different parameters. The aim of this master work is to quantify the crystal phases of the SLs of four different NW samples and study anomalies like lattice defects by the use of conventional transmission electron microscope (TEM), and link the findings to the growth conditions and detected lasing properties. Because of their size, TEM is the most common technique to characterize crystal phase and planar defects of NWs. To achieve this, dark-field (DF-TEM) images of entire NWs are made with special focus on their SL structures. The DF-TEM results are supplemented with high-resolution (HR) TEM lattice images and diffraction patterns (DPs) from selected regions for verification.

In this work, the samples studied are GaAs/GaAsSb core-shell NWs grown under different Sb_2 flux and growth time for the GaAbSb inserts. The crystal phase characterization of the sample NWs has been executed using conventional TEM techniques (bright-field (BF), DF and HR-TEM). Please note the long length and relatively large thicnesses involved. All the samples were grown from self-catalysed vapour-liquid-solid technique using molecular beam epitaxy (MBE) by PhD candidate Dingding Ren at the Department of Electronic Systems (IES) at NTNU.

The NWs studied are part of a larger research where PhD candidates Dingding Ren and Lyubomir Ahtapodov have studied the optical properties. PhD candidate Julie Stene Nilsen has done detailed compositional analysis of NW samples from the same batches. These three studies are complimentary, and the combined knowledge gathered should contribute to an increased understanding of the growth of these heterostructures and the lasing mechanism, and thereby further improve the lasing and realization of room-temperatured tunable NW lasers based on GaAs/GaAsSb heterostructures.

Chapter 2

Theory

In this chapter the theoretical background for the work in this thesis is presented. First, an introduction to crystallography and properties of crystals is presented. Theory on electron-matter interaction will then be given. These two topics make the base of understanding structural analysis of semiconductor nanowires (NW). In this work the NWs internal structure will be analyzed from data collected using a transmission electron microscopes (TEM). The instrumental setup of a TEM and the characterization techniques used in this thesis will be presented. Further, some semiconductor and laser theory will be introduced to explain why NWs can be used for laser applications.

2.1 Crystallography and scattering

Crystallography is a tool to describe crystal structures by studying the atomic and molecular structures of crystals with a long range-order. The following theory is based on the book *Introduction to Solid State Physics* [17] and compendium *Materials physics* [18] unless stated otherwise. Section 2.1.2 is based on [19], the theory in Section 2.1.3 in from [20], while Section 2.1.4 is based on the book *Faste Stoffers Fysikk* [21] unless stated otherwise.

2.1.1 Crystalline materials

The atoms in a crystal make up repetitive units called the *crystal basis.* If the entire material structure is described by translating this basis we call this an ideal crystal. By representing each basis in the crystal structure with a mathematical point one get the *crystal lattice*, described by the translation vectors $\mathbf{a}_1$, $\mathbf{a}_2$ and $\mathbf{a}_3$. These vectors define a parallelepiped called the primitive cell, or the *unit cell* of the crystal structure. This is the smallest basis one can define for a crystal structure. Each unit cell is associated with exactly one lattice point. A given crystalline material have a characteristic unit cell for it's crystal structure. The basis may be monoatomic or contain several atoms, which can be of different elements. The atomic position relative to the associated lattice point for an atom j in the base is

$$\mathbf{r}_j = x_j\mathbf{a}_1 + y_j\mathbf{a}_2 + z_j\mathbf{a}_3 \tag{2.1}$$

Lattice types

There are 7 different types of 3D *lattice systems* describing the cells of a crystal system, for example cubic and hexagonal lattice system. Of these 7 systems there are all in all 14 different subtypes, called *Bravais lattices.* Examples of these are face-centered, body-centered or simple cubic. Each Bravais lattice has certain characteristics, like constant volume of the cell and the primitive cell of the lattice, a constant number of lattice points per cell and unit volume, and constant packing fraction for monoatomic structures.

A conventional cubic cell that is often found in semiconductor materials is the face-centered cubic (FCC) space lattice . By definition, one unit cell contains only one lattice point, while the FCC lattice cell contains four points described by the translation vectors $\mathbf{a}_1 = \frac{1}{2}a(\hat{\mathbf{x}} + \hat{\mathbf{y}})$, $\mathbf{a}_2 = \frac{1}{2}a(\hat{\mathbf{y}} + \hat{\mathbf{z}})$ and $\mathbf{a}_3 = \frac{1}{2}a(\hat{\mathbf{x}} + \hat{\mathbf{z}})$ from the lattice point at the origin, as illustrated in (a)Figure 2.1. In this way, the basis atoms' coordinates $(x_n y_n z_n)$ in an FCC include (000), $(0\frac{1}{2}\frac{1}{2})$,$(\frac{1}{2}0\frac{1}{2})$ and $(\frac{1}{2}\frac{1}{2}0)$, where x_n, y_n and z_n describe the fractional coordinated in the unit cell.

A diamond crystal structure can be described by two identical FCC structures where one is shifted $(x, y, z) = (\frac{1}{4}, \frac{1}{4}, \frac{1}{4})$ with respect to the other. Thus, the diamond structure is a FCC lattice with two base atoms with positions $(x_j, y_j, z_j) = (0,0,0)$ and $(\frac{1}{4}, \frac{1}{4}, \frac{1}{4})$, as seen in (b) of 2.1.
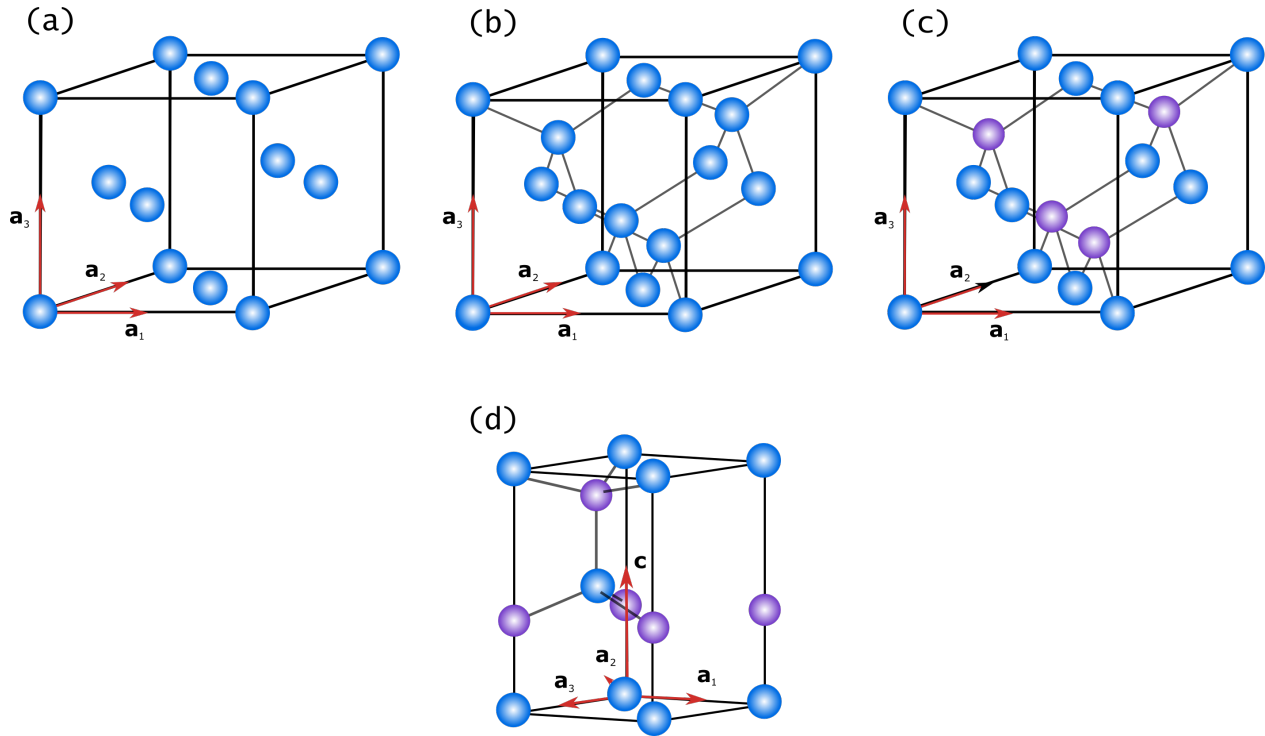
Figure 2.1: Illustration of the unit cell of the (a) FCC, (b) diamond, (c) ZB and (d) WZ structure. FCC and diamond are monoatomic while ZB and WZ are diatomic structures. WZ belongs to the hexagonal system while the other three belongs to the cubic.

This far, only monoatomic structures have been described. The NWs analyzed in this works consist in large parts of gallium arsenide (GaAs), which contains two different atoms, Ga and As, in the basis. Thus, the structures described from now on are no longer monoatomic.

The *Zinc blende* (ZB) and the *Würtzite* (WZ) structures are two common crystal phases of GaAs. A ZB structure is a diamond sturcture where the shifted FCC consist of a different element than the non shifted FCC. This is shown in Figure 2.1. In this way, the two structures may be expressed as two-based FCCs with basis at x_n, y_n, z_n = (000) and at $(\frac{1}{4}\frac{1}{4}\frac{1}{4})$, with identical basis atoms for diamond and different elements for ZB, as seen by comparing (b) and (c) in Figure 2.1.

The WZ structure, on the other hand, is a diatomic hexagonal close-packed (HCP) structured with base atoms in positions (x_j, y_j, z_j) = (0,0,0) and $(\frac{2}{3}, \frac{1}{3}, \frac{1}{2})$, as presented in (d) in 2.1.

2.1.2   Description of planes and directions

A *crystal plane* is defined by three non-collinear points, one in each spatial directions. The co-ordinates of crystal planes are defines in terms of the lattice constants a_1, a_2 and a_3. The orientation of a crystal plane is expressed by the *Miller index* system, and is denoted (hkl). h, k and l are called the *crystal plane indexes* and are derived by taking the reciprocals of the lattice constants and reducing them to three integers between 0 and 1 while maintaining the ratio between the lattice constants. Infinity is denoted as 0 (zero) and negative numbers are denoted with a bar above the integer. A crystal plane intercepting the lattice points 1,1,$\frac{1}{2}$, with reciprocals 1 , 1, 2, would be described by the Miller index (112). The family of same planes, the set of all equivalent (hkl)-planes, are denoted {hkl}.

Direction in a crystal is expressed on the form [uvw] where the integers are in the ratio of the vector components in the desired direction. These integers refer to axes such that the directions of the translations vectors $\boldsymbol{a}_1$, $\boldsymbol{a}_2$ and $\boldsymbol{a}_3$ have indexes [100], [010] and [001] respectively. In a cubic lattice the *crystal direction* [hkl] stands perpendicular on the (hkl) crystal plane. A family of same directions is denoted <uvw>

For a hexagonal lattice an additional crystal plane index, i or t, is introduced to represent the planes and crystallographic directions, also known as Miller-Bravais indexing. The representation of the crystal direction in an hexagonal lattice the becomes [$uvtw$], while a plane is represented by ($hkil$). It is also possible to use only the thee crystal plane Miller index using respectively the translation vectors $\boldsymbol{a}_1$, $\boldsymbol{a}_2$ and $\boldsymbol{c}$(Figure 2.1).

To convert the Miller indices for cubic lattice [$u'v'w'$] into the notional values [$uvtw$] for a hexagonal system one may use the relations

$$u = \frac{1}{3}(2u' - v') \tag{2.2}$$

$$v = \frac{1}{3}(2v' - u') \tag{2.3}$$

$$t = -(u + v) \tag{2.4}$$

$$w = w'. \tag{2.5}$$

The spots appearing in a diffraction pattern (DP) corresponds to a certain set of planes that are positioned almost parallel to the incident beam direction. Miller indices are used to indicate the reflection spots of the DP.

Crystals can alternatively be described by their stacking order in the crystal's close packed direction. ZB and WZ structures have close packed planes of atoms in the [111] and [0001] directions respectively. The close packed structure of ZB is said to gave stacking sequence of –ABCABCABC–, while WZ has an –ABABABAB– stacking sequence [17]. This is illustrated in Figure 2.2.
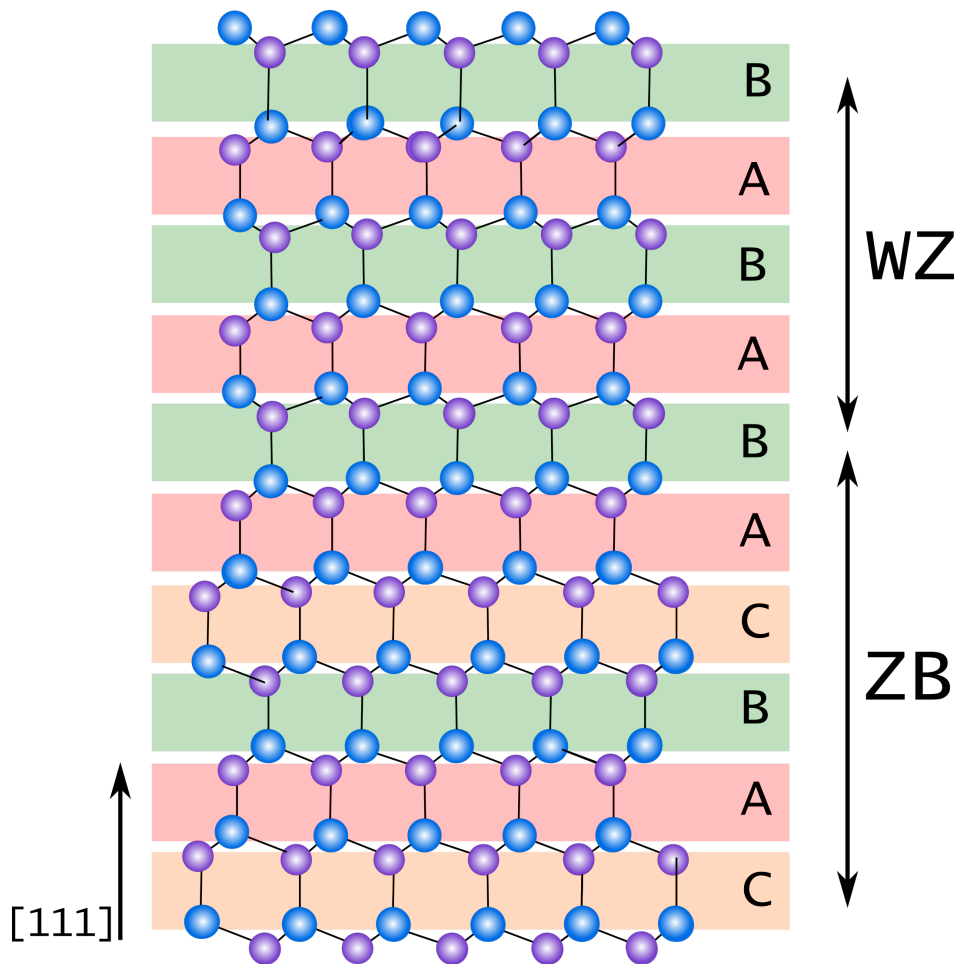

Figure 2.2: Schematics of stacking order in close packed directions for WZ-phase (1120) and ZB (110) showing a SF resulting in a phase shift.

2.1.3   Planar crystal defects

In reality, for large volumes, far from all crystal are ideal structures. Real µm-long NWs may contain defects and irregularities in the stacking sequence.

Cases where this stacking sequence is repeated for a long range in the stacking direction before a defect is present is called *polyptism*. It occurs where the close-packed crystal structure only differs in one dimension. In this way the stacking sequence of the structure varies without the overall geometry of the bilayers changing.

From Ramsdell notation ZB and WZ structure can be denoted as a 3C and 2H polytype, respectively [22]. The C stands for the cubic structure of ZB, while H stands for the hexagonal structure of WZ. The numbers represent the number of bilayers, denoted A, B and C.
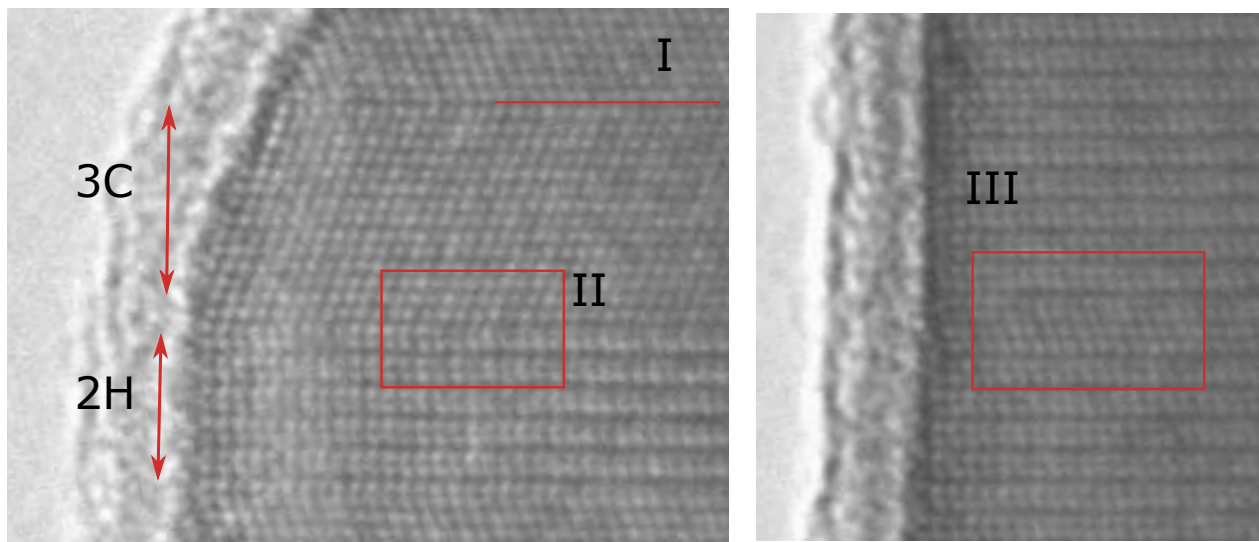

Figure 2.3: High resolution TEM image of GaAs/GaAsSb NW. I indicates the twinning boundary between two ZB stacking structures. II shows area with stacking fault that transitions from ZB to a WZ stacking structure, and III a WZ area with extrinsic stacking fault.

Twinning

Twin planes (TPs) are common defects in ZB structures. A TP is where two differently oriented crystal lattices intersect. An example of a TP is indicated as I in Figure 2.3. The stacking sequence then becomes –ABCAB|C|BACBA–, where the || marks the TP. This is the notation that will be used in this report. The stacking sequence after the TP will in this text be referred to as the twinned ZB structure, or ZBt.

Stacking faults

There are instances when single layers are added or absent in a stacking sequence. These planar defects are called *stacking faults* (SF). There are intrinsic stacking faults (ISF) and extrinsic stacking faults (ESF). An intrinsic stacking fault occurs when one {111}-type plane is missing in an otherwise perfect crystal structure. This results in a stacking sequence –ABCAB<u>CB</u>CABC– in a 3C ZB structure. In contrast, an extrinsic stacking fault is formed when an additional close-packed plane is added to the structure, making the stacking sequence of a 3C ZB structure – ABC<u>B</u>ABC–. An example of ESF is shown in Figure 2.3 marked III. These defects often form in ZB and WZ semiconductor structures to reduce strain energy when the growth conditions are not optimized, because of the low formation energy in such structures. Such crystal defects can be a transition from one crystal phase to another(Figure 2.2); a *phase change*. An example of a phase change from ZB to WZ is indicated in Figure 2.3 marked II.

Misfit dislocations

Misfit dislocations (MDs) are created when one material is grown on top of another and there is a lattice miss match. By introducing an extra plane, omitting one or more complex defects, the binding energy is reduced. The difference in lattice constant between the two materials then give rise to misfit dislocations at the material interfaces. Misfit of the lattice constants can also cause strain between two materials.

2.1.4   Reciprocal space

A crystal lattice can be represented in reciprocal space. This allows for application and under-standing of techniques such as diffraction patterns, which can be used to identify and analyze crystal structures. More on this will be elaborated in further sections.

The reciprocal lattice of a given Bravais lattice is the set of vectors $\boldsymbol{g}_{hkl}$ that gives a plane wave $e^{i\boldsymbol{g}_{hkl}\boldsymbol{r}}$ with the periodicity of the Bravais lattice. For $\boldsymbol{R} = n_1\boldsymbol{a}_1 + n_2\boldsymbol{a}_2 + n_3\boldsymbol{a}_3$ representing the lattice points of the Bravais lattice, for integers n_i, one can define a new set of vectors

$$\boldsymbol{a}_1^* = \frac{2\pi}{V_{uc}}(\boldsymbol{a}_2 \times \boldsymbol{a}_3) \tag{2.6}$$

$$\boldsymbol{a}_2^* = \frac{2\pi}{V_{uc}}(\boldsymbol{a}_3 \times \boldsymbol{a}_1) \tag{2.7}$$

$$\boldsymbol{a}_3^* = \frac{2\pi}{V_{uc}}(\boldsymbol{a}_1 \times \boldsymbol{a}_2). \tag{2.8}$$

Here $V_{uc} = |\boldsymbol{a}_1 \cdot \boldsymbol{a}_2 \times \boldsymbol{a}_3|$ is the volume of the primitive unit cell. These vectors $\boldsymbol{a}_i^*$ are the primitive vectors of the reciprocal lattice where every plane wave $\boldsymbol{g}_{hkl}$, that is constant over a translation with every lattice vector, is expressed as [17]

$$\boldsymbol{g}_{hkl} = h\boldsymbol{a}_1^* + k\boldsymbol{a}_2^* + l\boldsymbol{a}_3^* \tag{2.9}$$

with h, k and l being the Miller indices. The vector $\boldsymbol{g}_{hkl}$ is a reciprocal lattice vector, and all points in reciprocal space are mapped by this set of vectors.

The interplanar distance d_{hkl} is related to the length of the lattice vector $\boldsymbol{g}_{hkl}$ and the lattice constant a, for a cubic material

$$d_{hkl}^2 = \frac{a^2}{h^2 + k^2 + l^2}, \tag{2.10}$$

2.2 Elastic electron-matter interaction

A solid understanding of electron-matter interaction and it's effects is important to better use and analyze TEM images and DPs. A diffraction pattern can be described as the Fourier transform of the crystal structure. Each point in a diffraction pattern corresponds to a set of crystal planes parallel to the incident electron beam. The spots can therefore be labeled by the Miller indices for crystal planes, $(hkil)$, as presented in the section 2.1.2. The Fourier transform maps out the frequencies, or the atomic distances, from the specimen. A Fourier transform of a 3D specimen gives the 3D reciprocal lattice of all the specimen frequencies. One such resiprocal lattice point corresponds to an inter-atomic distance of a certain direction, and is denoted using the Miller indexes hkl. Which reciprocal lattice points that will have a non-zero intensity in the diffraction pattern assuming kinematic conditions is given by kinematic extinction rules. This is dependent on the material crystal structure and the geometry between the specimen and the incident beam. This is formulated as Bragg's law in real space, or as the Laue condition in reciprocal space. All the theory in this section is based on [23] and [17] unless stated otherwise.

2.2.1 Diffraction

Diffraction can be roughly defined as an interaction between a wave and an obstacle in it's path. When the incident beam scatters off parallel atom planes, and the reflected beams interfere constructively, we get diffracted beams. In a TEM environment, electrons scatter on atom plane spacings d_{hkl} in the crystal. Each d_{hkl} spacing give rise to a diffraction peak hkl in reciprocal space.

When considering electron diffraction, one must look at the wave nature of the electron, and how it interacts with matter. Bragg's law describes the scattered electron beams as if they were reflected off atomic planes of a perfect crystal with an interplanar distance d. The law states that incident waves that scatter with a scattering angle θ_B off of adjacent scattering centers must have a difference in path length equal to an integer times the wavelength λ, in order to remain in phase. This is expressed as,

$$2d \sin\theta_B = n\lambda. \tag{2.11}$$

This shows that constructive interference occurs when the waves are in phase. This is called Bragg scattering and θ_B is called the *Bragg angle*.

2.2.2 Kinematic scattering

In the kinematic scattering approximation one assumes that only single scattering events take place in the specimen for each electron, and that all scattering is coherent . This means that a *scattering vector* can be defined as

$$\boldsymbol{Q} = \boldsymbol{k}_d - \boldsymbol{k}_i, \tag{2.12}$$

where $\boldsymbol{k}_i$ and $\boldsymbol{k}_d$ are the wave vectors of respectively the incoming and diffracted beam. From this, a *scattering amplitude, F*, can be defined [17]

$$F = \sum_{\boldsymbol{g}} \int f \cdot e^{i(\boldsymbol{g} - \boldsymbol{Q}) \cdot \boldsymbol{r}} dV, \tag{2.13}$$

where f is the atomic scattering factor. This scattering amplitude maps the electric or magnetic field vectors in the scattered electromagnetic wave. Maximum scattering amplitude is achieved when $\boldsymbol{Q} = \boldsymbol{g}$. From this we get the *diffraction condition*

$$\boldsymbol{Q} = \boldsymbol{g}_{hkl}, \tag{2.14}$$

as Equation (2.11) stated that diffracted beams only appears for $\boldsymbol{g} = \boldsymbol{g}_{hkl}$. Equation (2.14) represent Bragg's law in reciprocal space.

Ewald's sphere

The lattice points that fulfill the diffraction condition in Equation (2.14) can be illustrated using the Ewald sphere construction in reciprocal space. The Ewald sphere radius is determined by the wavelength λ of the incoming wave by [23]

$$\mid \boldsymbol{k}_i \mid = \mid \boldsymbol{k}_d \mid = \frac{1}{\lambda}, \tag{2.15}$$

where $\boldsymbol{k}_i$ represents the wave vector of the incoming beam and $\boldsymbol{k}_d$ is any radius vector. In combination with the reciprocal lattice, as illustrated in Figure 2.4, the Ewald sphere shows which reflections that are present in the diffraction pattern for a certain orientation. The lattice points that are intersected by the Ewald sphere are the ones that fully satisfy the Bragg condition Equation (2.11).
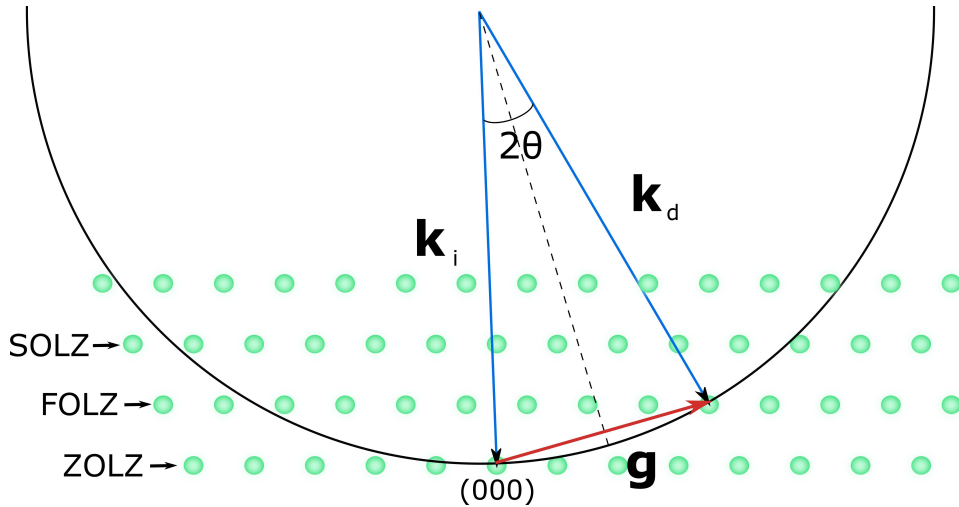
Figure 2.4: 2D representation of the Ewald's sphere construction with zero, first and second order Laue zones (ZOLZ, FOLZ and SOLZ) indicated. Illustration adapted from [23]

The small wavelength of accelerated electrons in a TEM (0.0251 Å at 200kV) results in an Ewald sphere that locally can be considered close to planar. This means that there are several reciprocal lattice points located on, or close to the sphere, for each crystal position [18]. This allows for several reflections to be seen. Also higher order Laue zones (HOLZ) can be seen.

What is small in real space will be large in reciprocal space and vice versa. Due to the small specimen sizes in the TEM, the reciprocal lattice consist of extended rods with center in each lattice point, known as *relrods*. The relrods have a finite thickness with extension parallel to the incident beam. This means that a diffraction spot can still appear when the diffraction condition is not fully satisfied, but the Ewald sphere intersects the relrod a distance $|s|$ from the relrod's center. The intensity of the diffraction spot, or reflection, depends on the deviation s from the ideal Bragg condition such that [23]

$$K = g + s. \tag{2.16}$$

$s = 0$ when the Ewald sphere intersects the reciprocal lattice point at the center of the relrod. When the intersection point is not exactly at the relrod's center, s will be of positive value if relrod center is located inside the Ewald sphere, while it will have a negative value for center positions outside of the sphere. Maximum reflection intensity is achieved for $s = 0$, and the intensity decreases as $|s|$ increases. If thickness is large and s is low there is a high chance of several scattering events taking place. For this, the kinematic assumption is not valid, which will be addressed further in Section 2.3.

2.2.3   Structure factor and extinction rules

For a random reflection characterized by a reciprocal lattice vector $\boldsymbol{Q}$, the relative phase factors for units with positions $\boldsymbol{r}_n$ will be given by $e^{i\boldsymbol{g}\boldsymbol{r}_n}$ for $n = 1, 2, 3...s$, like defined earlier for $\boldsymbol{g}$.

The *form factor* $f_n(\boldsymbol{Q})$ characterizes the atomic scattering factor for atom n. The total *scattering amplitude* for all lattices is the *structure factor*

$$F(\boldsymbol{Q}) = \sum_{n=1} f_n(\boldsymbol{Q}) e^{-i\boldsymbol{Q}\boldsymbol{r}_n}. \tag{2.17}$$

.

The intensity of the reflections from a crystal is proportional to the square of the structure factor. Scattering to a certain reflection hkl in a crystalline material

$$F_{hkl} = A_0 \sum_n^{basis} f_n e^{-2\pi i (hx_n + ky_n + lz_n)}, \tag{2.18}$$

where f_n is the atomic scattering factor, describes which reflections that will be present in a diffraction pattern. The cases when $F_{hkl} = 0$ are called kinematically forbidden reflections and will not be present under kinematic conditions.These reflections may, however, sometimes be present due to dynamical scattering.

An FCC structure can be considered a simple cubic basis with an atom at the origin $x_n, y_n, z_n = (000)$ and at the three adjacent faces $x_n, y_n, z_n = (\frac{1}{2}\frac{1}{2}0), (\frac{1}{2}0\frac{1}{2}), (0\frac{1}{2}\frac{1}{2})$. With this in mind, 2.18 can be rewritten as

$$F_{hkl}^{FCC} = A_0 f_n (1 + e^{-i\pi(h+k)} + e^{-i\pi(h+l)} + e^{-i\pi(k+l)}), \tag{2.19}$$

This leads to the extinction rules that if the h,k,l are of mixed odd and even values, there is no reflection, but if they are all odd, or all even, the structure factor is $4 A_0 f_n$.

By treating a ZB structure as an FCC with a basis of the first type of atom at (000) and the second atom type at $(\frac{1}{4}\frac{1}{4}\frac{1}{4})$, the structure factor can be written as a product of the structure factor of an FCC and the structure factor of the basis, with the atomic scattering factor of the different atoms, i.e.

$$F_{hkl}^{ZB} = A_0 (1 + e^{-i\pi(h+k)} + e^{-i\pi(h+l)} + e^{-i\pi(k+l)})(f_1 + f_2 e^{-\frac{i\pi}{2}(h+k+l)}). \tag{2.20}$$

For this case, the same extinction rules apply as for the FCC structure.

The structure factor for ZB crystal structure for diatomic structure can them be expressed as

$$
F_{hkl}^{ZB} = \begin{cases}
0 & h, k, l \text{ mixed} \\
4(f_1 + f_2) & h, k, l \text{ all even and } h + k + l = 4n \\
4(f_1 - f_2) & h, k, l \text{ all even and } h + k + l = 4n + 2 \\
4(f_1 + i f_2) & h, k, l \text{ all odd and } h + k + l = 4n + 3 \\
4(f_1 - i f_2) & h, k, l \text{ all odd and } h + k + l = 4n + 1
\end{cases}
$$

where n is an integer. Examples of kinematically allowed reflections are (000), (111) and (002) (Figure 2.5(a)). The intensity of the reflections will depend on the atomic scattering amplitude of atoms 1 and 2, as well as the thickness of the crystall as it increase the chance of multiple scattering events (dynamical effects). However, Friedel's law states that the intensities $I(h, k, l)$ and $I(\bar{h}, \bar{k}, \bar{l})$ are equal. This is a property of the Fourier transform of a real function.

The structure factor for WZ phase can be derived by a similar method as used for ZB, by considering hexagonal close-packed (HCP) structure with the basis of the first atom type in $(\frac{1}{3}, \frac{2}{3}, 0)$ and $(\frac{2}{3}, \frac{1}{3}, \frac{1}{2})$, and the second atom type in $(\frac{1}{3}, \frac{2}{3}, \frac{3}{8})$ and $(\frac{2}{3}, \frac{1}{3}, \frac{7}{8})$. The structure factor of WZ of a diatomic base can thus be expressed by

$$
F_{hkl}^{WZ} = A_0 (e^{-2\pi i (\frac{1}{3} h + \frac{2}{3} k)} + e^{-2\pi i (\frac{2}{3} h + \frac{1}{3} k + \frac{1}{2} l)})(f_1 + f_2 e^{-\frac{i3\pi}{4}(h+k+l)}). \tag{2.21}
$$

As the intensity of the scattered beam, $I(\boldsymbol{Q})$, can be expressed as the square of the scattering amplitude, the kinematically allowed and forbidden reflections for WZ crystal phase can be summarized as

$$
| F_{hkl}^{WZ} |^2 = \begin{cases}
0 & l \text{ odd, } h - k = 3n \\
3(f_1^2 \pm \sqrt{2} f_1 f_2 + f_2^2) & l \text{ odd, } h - k \neq 3n \\
4(f_1 \pm f_2)^2 & l = 4m, h - k = 3n \\
(f_1 \pm f_2)^2 & l = 4m, h - k \neq 3n \\
4(f_1^2 + f_2^2) & l = 4m + 2, h - k = 3n \\
(f_1^2 + f_2^2) & l = 4m + 2, h - k \neq 3n
\end{cases}
$$

where n and m are integers. Examples of kinematically allowed reflections are (000), ($1\bar{1}0$), and (002) (respectively (0000), ($1\bar{1}00$) and (0002) in Miller-Bravais index as seen in Figure 2.5(b)). The kinematically forbidden reflections, marked with cross in Figure 2.5 (b), for example reflection (001), or (0001) in Miller-Bravais indexation, often appear in DPs of thicker samples as they are a subject of multiple diffracted beams.
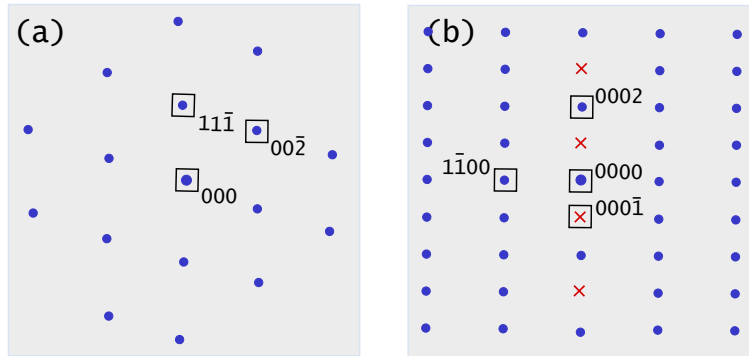

Figure 2.5: DPs of (a) ZB [$1\bar{1}0$] and (b) WZ [$11\bar{2}0$]. The crosses mark kinematically forbidden reflections.

2.3   Transmission electron microscopy

The following theory is based on the book *Transmission electron microscopy* [23] unless stated otherwise.

A transmission electron microscope (TEM), allows for higher spatial resolution, combines imaging, diffraction and spectroscopy application in one instrument. This makes it arguably the most important tool for studying materials down to the atomic level in for example nanotechnology and solid state physics [18, 23].

However, TEM is expensive and a time consuming technique. Special lenses and detectors are needed, as well as a highly stable environment and requires thin samples (< 100 nm specimen), which sometimes calls for complicated specimen preparations. An understanding of how the microscope works and the physical principles behind it is important to purposefully operate a TEM and use it to gather and interpret data.

Resolution

The classical way of calculating the resolution of a microscope is by using the Rayleigh criterion [23],

$$\delta = \frac{0.61\lambda}{\text{NA}}.$$ (2.22)

This equation gives the smallest distance δ that can be resolved in a visible-light microscope with radiation wavelength λ and numerical aperture NA.

In contrast to the traditional optical microscopes that uses visible-light as a source, the TEM uses electrons. From Equation (2.22), this means that TEM can achieve a much higher resolution since the wavelength of the electron is much smaller than that of visible light.

The wavelength of an electron is dependent on it's energy. Clasically, this relationship is represented in the de Brogile equation [23]

$$\lambda = \frac{1.22}{E^{\frac{1}{2}}}$$ (2.23)

where the electron wave length, λ, in nm is dependent on the electron energy E expressed in eV. For a 100keV electron beam this corresponds to a wavelength of around 4 pm. However, electrons with an energy of 100 keV and above, like the ones accelerated in a TEM, have a relativistic velocity of over $1.644 \cdot 10^8$m/s [23] and need to be considered relativistically.

Relativistically, the momentum of an electron is given by [23]

$$p = \text{m}v = (2\text{me}V)^{1/2}$$ (2.24)

where m is the electron mass and v is it's relativistic speed, expressed by the electron charge e. From Equation (2.24) and the particle-wave duality of the electrons, the wavelength can be expressed as Planck's constant over the electron momentum. By combining this with de Brogile's equation, the relativistic wavelength of a high energy electron can be expressed by [23]

$$\lambda = \frac{\text{h}}{\left(2\text{me}V_a\left(1 + \frac{\text{e}V_a}{2\text{mc}^2}\right)\right)^{1/2}},$$ (2.25)

where c is the speed of light and h is the Planck constant. From Equation (2.25) the relativistic wavelength of an electron accelerated with a voltage V_a of 200 kV is 2.51 pm [23]. Using Equation (2.22) and numerical aperture (NA)= 1, the resolution in such a TEM would amount to 1.53 pm. The real resolution in a TEM is, however, far poorer. As opposed to an optical light microscope, it is the small NA that is the limiting factor for the resolution in a TEM, and especially the spherical aberration C_s. Still, the resolution of a TEM amounts to approximately 2Å. This gives resolution good enough to distinguish two neighboring atoms, but the lenses used are highly imperfect and only the electrons near the optical axis are used. More on this will be elaborated in Section 2.3.

Column

The concept of TEM is that a beam of accelerated electrons is sent down on a thin sample, where the transmitted electrons are detected on a CCD camera or a fluorescent viewing screen.

The *column* makes up the most important part of the hardware of a TEM. Essentially, the TEM column is made up of an electron beam source, a condenser system, an objective system, intermediate and projector lenses and a detection system, as illustrated in Figure 2.6.

In TEM, the lenses are made of electromagnetic coils that generates magnetic fields in the bore, which deflects and shapes the charged electrons that travel through it. By varying the electric current through the coils, the magnetic field, and thus strength of the lenses, can be controlled. In this way, the lens is fixed in space while the strength can be varied, which is opposite for that of a conventional visible light lens.

The electrons spiral through the lens field with a helical trajectory as the electrons feel Lorentz force. This results in a rotation of the image of the sample for different magnifications, unless corrected for. The beam gets shifted and tilted by deflector pairs at different positions in the column, while stigmators correct for beam astigmatisms to make sure it stays circular.

A conventional TEM, and the one used in this works, have three adjustable apertures; condenser lens aperture, objective lens aperture and selected area aperture. These strategically block out some parts of the beam from contributing to the resulting signal. All apertures have a variation of sizes (10-150 μm) that can improve the specification and quality of the desired image, but at the cost of intensity.
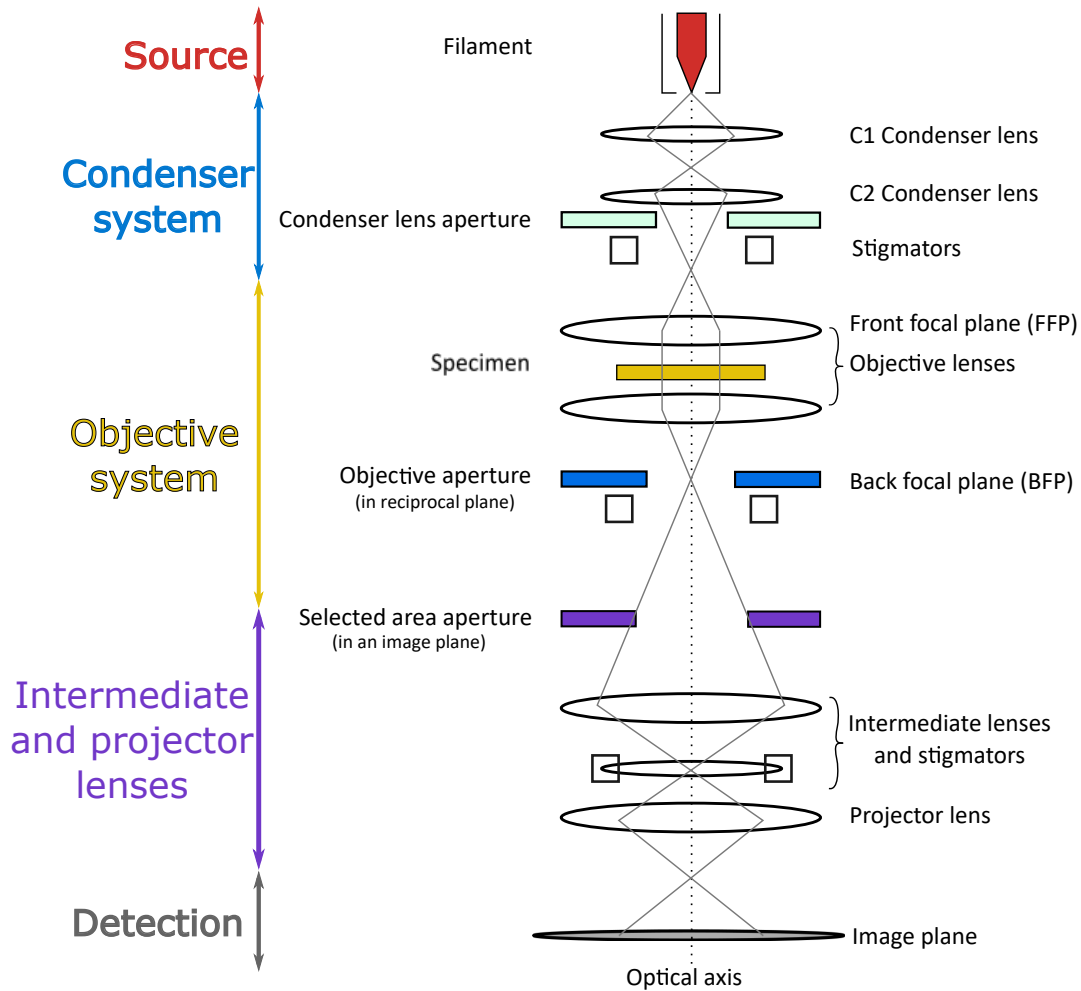
Figure 2.6: Simplified schematics of the TEM column adapted from [23, 24]

Working from the top-down of the TEM column in Figure 2.6, first stop is the *electron beam source*. In the TEM used in these works a thermo-ionic filament LaB_6 is used as a source to emit electrons. After that comes the *condenser system*, which consist of at least two condenser lenses, C1 and C2, condenser stigmators and the *condenser lens aperture*. The C1 lens regulates the beam spot size while C2 adjusts the beam brightness. The electromagnetic lenses work best for the electrons close to the optical axis as the beam gets more bent the further away from the optical axis it gets. The condenser lens aperture limit the angular distribution by blocking out electrons that deviates more than a certain angle from the optical axis. This keeps the electrons close to the optical axis, and thus improves the resulting images by scarifying some of the beam intensity.

Next is the *objective system*. The objective lens is the strongest of all the lenses, and it is the most important one to create the image and DP from the specimen sample. The *objective lens aperture* is located in the back focal plane of the objective lens, or in reciprocal space. It selects which scattered beam, or scattering angles, contributes to the final image. (The specimen is placed *in* the objective lens as a might magnetic field is needed to focus fast electrons.) In this way, the objective aperture can select specific beams after the interaction with the specimen has occurred. The *selected area aperture* can be inserted in the first image plane of the objective lens to get a DP of a limited area (down to 100-150 nm in diameter) of the image. It selects what part of the specimen image, that contributes to make the DP.

After this, a series of intermediate lenses and projection lenses are placed. These select the image mode or diffraction mode, and magnifies the intermediate image or DP. The final image plane is detected by the use of a fluorescent screen or a CCD camera for recording. Here, there are several issues to consider. For example pixel size and field of view limits the resolution and accuracy of the recorded data.

There are many other components that also makes up the TEM, like the vacuum system, the electronics, software and sample holders, but these will not be discussed further here.

Electron-specimen interaction in TEM

The following subsections are based on [18, 23] unless stated otherwise. Electrons are low in mass and negatively charged particles that are easy to create, handle and detect. They interact strongly with matter, which results in a low penetration depth, even for high voltages. Thin samples, up to a few hounded nanometers, are therefore needed for transmission of the high energy electrons used in a TEM. However, it also means that small specimen volumes can be inspected. An other criteria that derives from the strong interaction is the need for an ultra-high vacuum environment inside the TEM column. This is necessary to keep the electrons from interacting with the air on their path down to the specimen.

The base principle that makes TEM feasible is the fact that electrons experience Coulomb interactions and scatters. In TEM the scattering intensity is measured, but the phase is lost. Up until now, only kinematic scattering conditions have been considered. However, if the specimen is thicker than just a few nanometer, the incoming electron beam will undergo multiple

scattering before leaving the it. The NWs analyzed in this work are around 400 nm thick. If such a sample is oriented so that the direct beam is Bragg diffracted off of the atom planes, then it has the perfect orientation for the beam to rediffract by an other set of atom planes in the specimen and scatter back into the direct beam. The rediffracted beam will thus rescatter again and again and give rise to *dynamical scattering effects*. Because of this, the description of diffraction effects, as presented in Section 2.2, is not sufficient. A refinement of scattering theory is therefore required to fully describe the interactions.

The *extinction distance ξ_g* of the diffraction vector g has magnitude expressed by

$$\xi_g = \frac{\pi V_c \cos\theta_B}{\theta F_g}, \tag{2.26}$$

where F_g is the structure factor for reflection g, V_c the potential of the lattice parameter b and λ is, for the TEM case, the electron wavelength. ξ_g is measured in ångströms, Å. From Equation (2.26) it becomes clear that ξ_g is dependent on the material lattice parameter through the value of V_c, the atomic number through the structure factor and the electron wavelength which is defined by the applied voltage. If the voltage increase, λ will become smaller and thus ξ_g will become larger.

The intensity of the Bragg-diffracted beam for dynamical scattering conditions is expressed by [23]

$$I_g = \left(\frac{\pi t}{\xi_g}\right)^2 \cdot \frac{\sin^2(\pi t s_{\text{eff}})}{(\pi t s_{\text{eff}})^2}, \tag{2.27}$$

where s_{eff} is the effective excitation error of dynamical scattering, defined as

$$s_{\text{eff}} = \sqrt{s^2 + \frac{1}{\xi_g^2}}. \tag{2.28}$$

Diffraction contrasts in, BF or DF, images of the specimen occurs because of the difference in intensity of the diffracted beams in different parts of the specimen either as s or t changes. $I_g = 0$ for $t = n\xi_g$, for an integer n, hence the name extinction distance. As the specimen thickness increases, so does the probability of dynamical scattering. The variations of intensity may therefore come from difference in the thickness of the different parts of the specimen, from bending of the specimen or from change in diffraction conditions.

TEM modes

In TEM mode, a broad, close to parallel beam of electrons is used to illuminate a thin specimen. The beam intensity is considered uniform throughout the area that is illuminated. In a TEM it is the electrons that eventually hits the specimen that are considered the incident beam. The scattered beam is the collective name for the electrons are scattered off the specimen. The electrons that pass through the specimen without deviating from the incident angle, as seen in Figure 2.7 are referred to as the direct beam.

Electrons interact strongly with both atom cores and the electron cloud of the atoms. This leads to various of signals created simultaneously from electron specimen interactions, as illustrated in Figure 2.7, that can be detected in a TEM. From these signals, a lot of different information about the specimen can be retrieved.
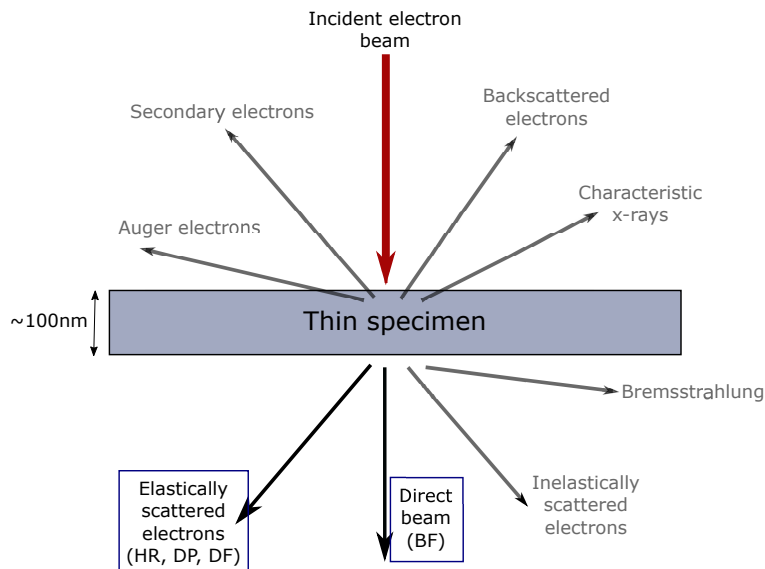
Figure 2.7: Illustration of the incident beam, the scattered beam and the direct beam relative a specimen in a TEM. The figure is adapted from [23].

For each kind of radiation there exist several different types of spectra that can be detected in different TEM modes. All these various techniques make TEM not only able to provide images of diffraction patterns of the specimen, but present other information about the specimen, like chemical composition and electronic structure. The combination of several techniques that can be applied on the same space of the specimen, and almost simultaneously is one of the primary advantages of TEM. Most important for the techniques used in this work are the elastically scattered electrons and the direct beam, shown in Figure 2.7.
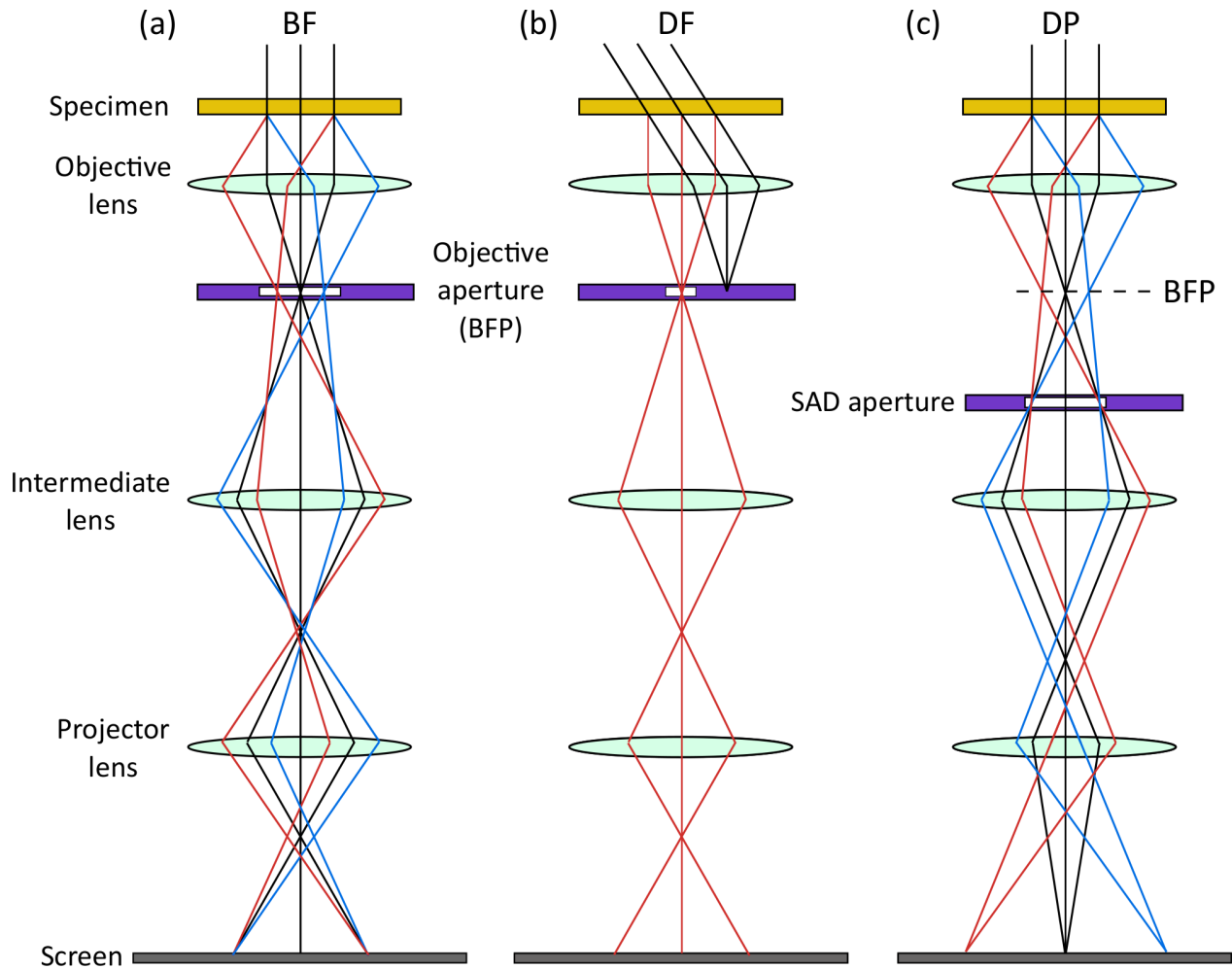
Figure 2.8: Schematics of (a) BF imaging, (b) centered DF (c) SAED . Adapted from [23]

Because of the scattering events that some of the electrons in the incident beam encounters, the electrons that exit the specimen no longer has a uniform distribution. It is by detecting this distribution that the structural properties of the specimen can be analyzed. This distribution of signals can be displayed in two main ways; *spatial distribution* and *angular distribution*. The spatial distribution provides the specimen images, while the angular spread of the beam gives the scattering pattern, or the DP. This is illustrated in Figure 2.8 where (a) and (b) displays the spatial resolution in two different ways, and (c) shows the DP. Forward scattering of fast electrons is the cause of most of the signals used in TEM [23]. In these TEM modes are used to make diffraction patterns, bright-field (BF) images and dark-field (DF) imagesof the specimen. This will be elaborated further in the following paragraphs.

Diffraction patterns are maps of the electron distribution at the back focal plane of the objective lens. This is the reciprocal image plane, and show the reflections of the crystal structure of the specimen as described in Section 2.2. These are retrieved in diffraction mode, illustrated in Figure 2.8 (C). By spreading the electron beam, the illumination will become close to parallel. A selected area aperture can be placed in the first image plane below the objective lens, as indicated in illustration (c) in Figure 2.8, to select an area of this image that will contribute to the diffraction pattern. This is called to perform *selected area electron diffraction* (SAED) [18]. SAED show sharply focused spot patterns. The sharpness of a diffraction spot is dependent on the number of unit cells within the scattering volume [18].

Bright-field images map the specimen using the electrons from the direct beam only. For this, the objective aperture may be inserted, as illustrated in Figure 2.8 (a). As only the direct beam or the electrons with a low scattering angle are selected, the image contrast will be dominated by mass-thickness contrast. In this way, the specimen areas with high thickness will appear dark, while thinner sections are lighter in the BF image. A NW imaged in BF mode will thus appear dark against the thin sample film.

Dark-field images are formed by the selection of certain scattered electrons. This is done by tilting the incident beam so that selected reflections from a scattered beam get on the optical axes, rather than the incident beam. The selected scattered beam will then go through the optical aperture that is centered around the optical axes, filtering out the direct beam as well as the other reflections. This is called *centered dark-field* imaging and is shown in Figure 2.8(b). As this is the only DF operation used in this work, it will from here on only be referred to as dark-field imaging. Diffraction contrast is the dominating image contrast when applying DF mode, as the coherently scattered electrons at a certain Bragg angle are selected to form the DK image.

HR-TEM

There is another TEM technique, namely the High Resolution TEM (HR-TEM), where the fact that one never manage to conserve all the information of the specimen into one TEM image becomes evident. As discussed earlier in this chapter, the TEM lens system is not perfect. Some of the information of the sample will be distorted or lost before the image representing it is formed. One distortion of the image is known as smearing, where a point on the specimen becomes a disk on the image of the sample. This smearing effect is expressed by the *point-spread function* $h(\boldsymbol{r})$. As a point on the specimen becomes a disk in the image, one point in the image will consist of the overlapping contribution of the disks from many points of the specimen. This contribution can be described mathematically by the image function $g(\boldsymbol{r})$, which is the convolution of the specimen function $f(\boldsymbol{r})$ and the transfer function $h(\boldsymbol{r})$. From the convolution theorem, this relation can be expressed by the Fourier coefficients [23]:

$$G(\boldsymbol{u}) = F(\boldsymbol{u})H(\boldsymbol{u}) \tag{2.29}$$

where $\boldsymbol{u}$ is the reciprocal lattice vector. $H(\boldsymbol{u})$ is the contrast transfer function and contains contributing factors from the TEM apertures ($A(\boldsymbol{u})$), the wave attenuation ($E(\boldsymbol{u})$), and the objective lens aberrations ($B(\boldsymbol{u})$). $H(\boldsymbol{u})$ can thus be expressed as

$$H(\boldsymbol{u}) = A(\boldsymbol{u})E(\boldsymbol{u})B(\boldsymbol{u}) \tag{2.30}$$

To express a simpler term to describe the HR-TEM imaging we simplify the expressions using the weak phase-object approximation (WPOA). This gives a linear relation between the transmitted wave function amplitude, and the projected potential of the specimen, assuming a thin specimen. The abberation function $B(\boldsymbol{u})$ can be then expressed as

$$B(\boldsymbol{u}) = 2\sin\chi(\boldsymbol{u}) \tag{2.31}$$

where the term $\chi(\boldsymbol{u})$ is called the phase distortion function, and is written as

$$\chi(\boldsymbol{u}) = \pi\Delta f\lambda u^2 + \frac{1}{2}\pi C_s\lambda^3 u^4 \tag{2.32}$$

where Δf is the overfocus of the objective lens, so the focus on a plane above the specimen. λ is the electron wavelength and C_s is the spherical aberration from the lens. When taking an HR-TEM image, what we observe is the contrast. From this, an *objectve lens transfer function* (OLTF) can be formulated as a simplified version of $H(\boldsymbol{u})$, to describe this contrast, by

$$T(\boldsymbol{u}) = A(\boldsymbol{u})E(\boldsymbol{u})2\sin\chi(\boldsymbol{u}). \tag{2.33}$$

For negative $T(\boldsymbol{u}$, atoms appear brighter against a dark background, while for a negative $T(\boldsymbol{u})$ the atoms appear dark against a light background. No image contrast is visible for $T(\boldsymbol{u}) = 0$. $T(\boldsymbol{u}$ is, thus, sometimes also referred to as the contrast transfer function (CTF), although it is based on a simplified model based for very thin samples (WPOA). When plotting the CTF, the resolution limit is where the function first crosses the x-axis (Figure 2.9), in $\boldsymbol{u}_1$. It is desirable to have $\boldsymbol{u}_1$ as large possible to get a high resolution to more orless directly interpret the HR-TEM images.
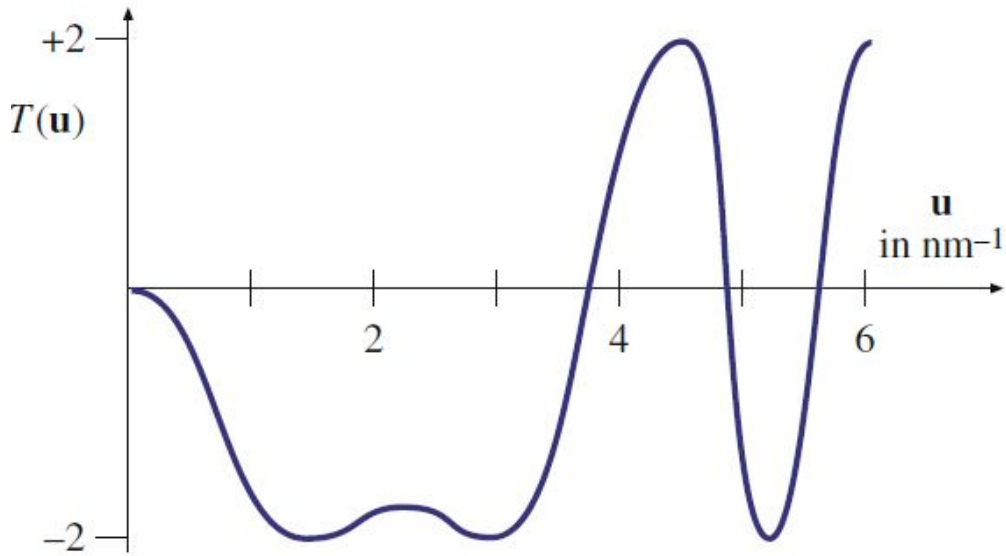

Figure 2.9: Plot of $T(\boldsymbol{u})$ for $C_s = 1\text{mm}$, $\Delta f = -58\text{nm}$ for an electron beam at 200kV. The figure is taken from Wiliams and Carter, Chapter 28[23].

2.4 Nanowires

GaAs NWs can be grown using vapor-liquid-solid (VLS) growth mechanism on a Si(111) sub-strate by the use of Ga-assisted molecular-beam epitaxy [25]. The following theory on VLS is based on [26], while description of MBE is from [16], unless otherwise stated.

The VLS mechanism principle is that atomic vapor is deposited on to a liquid alloy droplet on the sample, formed by an impurity at the surface. The vapor causes the liquid to become super-saturated with the desired material (for example GaAs or Si) and the NW grow by precipitation of the material from the droplet as illustrated in Figure 2.10. The standard VLS process uses gold (Au) as catalyst droplet on a silicon (Si) wafer to grow a Si NW. In this case the Au is heated un-til a liquid Au-Si alloy is formed on the wafer surface. Vapor is then introduced, hydrogen (H) and silicon chloride (SiCl). However, the liquid droplet acts as a catalyst for chemical processes leading to Si entering the liquid and being freezed out with a very low Au concentration in the resulting solid solution. As this process is continued, the alloy droplet will be displaced in <111> direction away from the substrate surface as the NW continues to grow underneath it, as seen in Figure 2.10. The side faces of the NW are normally {112} or { 110}. This growth will continue until the Au droplet is consumed by the process or until termination of vapor introduction.
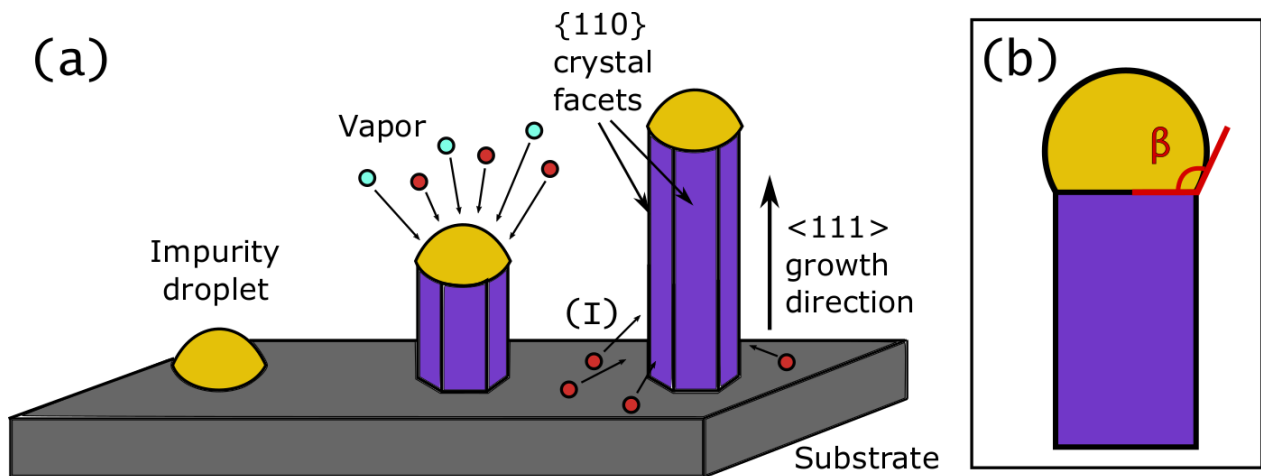

Figure 2.10: (a) Schematics illustrating growth of NW by VLS. (I) show diffusion from substrate. Figure is adapted from [26] (b) indicate the contact angle β of the catalyst droplet.

One concern when using Au catalyst droplet is that the Au may get incorporated in the grown crystal structure. In VLS growth of compound crystals like GaAs, incorporation of Au may create deep energy levels and prohibiting recombination processes. To avoid this, self-catalyst VLS growth can be a solution. For this method, a Ga droplet is used as catalyst particle. This solves the Au contamination of the nanostructure grown. However, Ga is affected by growth, changing it's size and shape, and thus the resultant nanostructure grown [27].

Molecular-beam epitaxy (MBE) is one of the most conceptually easy ways to make a heterostructured semiconductor structure. The ultra-high vacuum environment enables the growth of high quality substrates and nanostructures of atomic precision. It is essentially a two-step procedure carried out in an ultra-high vacuum environment illustrated in Figure 2.11. In step one, atoms that are the constituents of the growing material, for example Ga and As_2 or As_4 for GaAs, are evaporated from solid sourced in heated cells, known as Knudsen cells at a rate controlled by the heating temperature. The particles are then collimated into beams and deposited onto the surface of the heated substrate. Since this is a directional process, the substrate is often rotated to assure a more uniform deposition. The composition is controlled by shutters at each Knudsen cell, that shuts off the beam from the undesired cell.

Step two of the process concerns the migration of the deposited species on the surface prior to their incorporation into the growing material. This depends on various factors, mainly deposition rates and thermal factors. This second step determines the morphology, or the profile, of the deposited film or growing nanowire. In practice, however, the diffusion of elements from the substrate onto the growing nano-object is an additional growth factor that has to be considered. As illustrated in Figure 2.10, not only the vapor coming straight from the Knudsen cells will contribute to growth close to the substrate.

It has been found that changes in the structural composition at the interfaces between the inserts of the heterostructured nanowire will affect the bandgap (BG) and the carrier concentration of the system. This means that the optical properties of the nanowire structure depends on the structural composition at the heterostructural interfaces [25]. Accurately analyzing the NW for characterization of the interfaces is therefore needed in order to understand why a NW laser has a certain optical property.
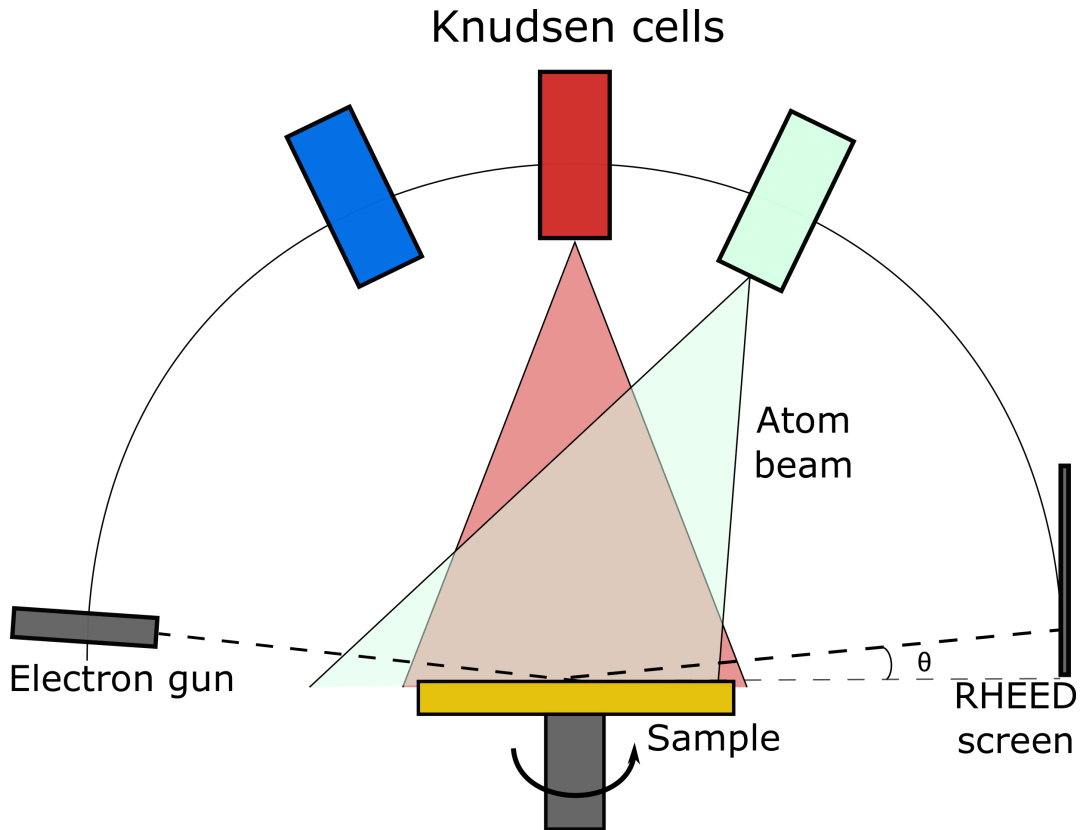
Figure 2.11: Schematics illustrating the MBE technique. Figure is adapted from [16]

2.5 Lasers

The invention of Light Amplification by Stimulated Emission of Radiation devices, or lasers, have revolutionized science and industry, and small semiconductor lasers have become a part of every day life [28]. Compact semiconductor lasers have given birth to a vast specter of new technological equipment, ranging from bar code scanners and laser printers to optical fiber communication and laser eye surgery [28]. The following theory is based on [16] chapter 8 and 6 unless stated otherwise.

A laser, as the name suggests, takes advantage of the principle of stimulated emission, a phenomena first predicted by Einstein in 1917 [29]. When a photon of a certain energy interacts with an atomic electron of an excited state this may cause it to drop to a lower energy state. In a material with a direct bandgap, like GaAs, this liberation of energy results in the emission of a "daughter" photon, which will be coherent to the incident "mother" photon. This process is what is called stimulated emission [29]. The recombination does not necessarily only take

place from the lowest conduction band. Higher energy electrons can recombine as well, creating a blue shift in the emitted wavelength. The process of stimulated emission is illustrated in Figure 2.12. This recombination of a higher energy electron, causing the emission of a photon, can also happen without the stimuli of an incoming photon. This is called spontaneous emission, and is a process that occurs at random, as opposed to stimulated emission. However, the spontaneous emission of a photon with sufficient energy can result in stimulated emission in a laser structure.
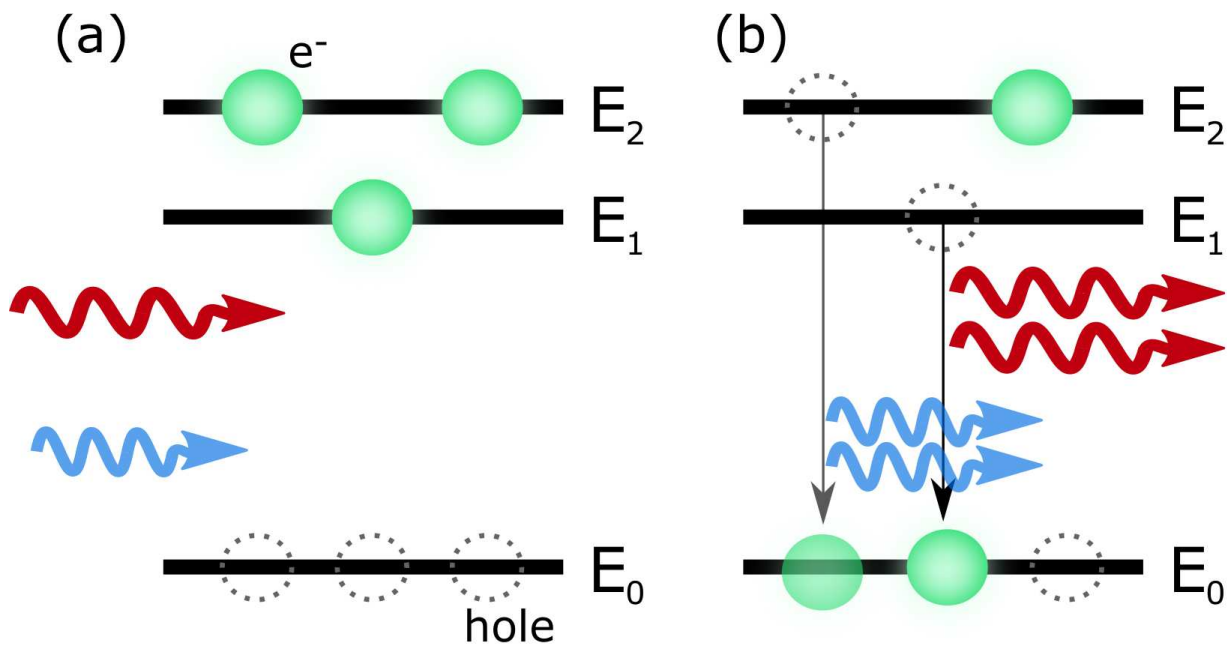

Figure 2.12: Illustration of the process of stimulated emission. An incoming photon in image a) triggers an electron at an excited energy level E_1 to drop to a lower energy state E_0, showed in b, by releasing the same energy as the energy of the incoming photon. The release of energy results in emission of an additional photon coherent with the incident photon. Incoming photons of higher energy can trigger electrons from higher energy bands.

2.5.1 Semiconductor laser

To achieve lasing in a semiconductor laser one essentially need to have an active region, population inversion, and an optical cavity. The active region is where electrons and holes recombine, making stimulated emission possible. A criteria is that the semiconductor should have a direct bandgap so that the quantum efficiency is sufficiently high to overcome losses within the laser cavity, as is present in for example GaAs. A system has population inversion if there are more electrons occupying higher energy states than lower states. This means that when interacting with a photons the stimulated emission of the semiconductor exceeds the absorption, which is the inverse of a normal media in thermal equilibrium. Population inversion is crucial for stimulated emission to be possible, and therefore the first criteria for lasing that needs to be fulfilled. An optical cavity is necessary to create an optical feedback for the emitted photons as it is stimulated. This reflects the photons back into the active region causing one photon to make several round trips and thereby amplifying the optical signal. The photon can then contribute to stimulated emission several times before the photon escapes the system. Such a cavity can be formed by cleaving the crystal structure of the laser material, creating a reflective mirror in end facets [31].

2.5.2 Nanowire laser

Ever since Meiman produced the first working laser in 1960 [5], there has been an interest in optimizing and downscaling lasers. This development has now taken technology to quasi 1D semiconductors; nanowires. The reasons of this downscaling are numerous. Some advantages include quality improvements, less material required and more possibilities in highly local integration into other devices. This, with the purpose to develop lasers for optoelectronics and on-chip photonic devices on the nanoscale. The following theory is based on the review article [28] unless stated otherwise.

The first use of semiconductor nanowires laser application was described in a paper by Huang et al. published in 2001 in Science [7], and was a breakthrough in downsizing of laser devices. However, the nature of the optical cavity of the NW laser was not determined. Since then, three main types of laser cavities have been suggested for semiconductor NW lasers; optically pumped cavity, plasmonic laser and electrically pumped cavity. The first one is relatively easy, the others much more challenging. In this text, only the first and last type will be considered.

Optically pumped lasers   were the first types of NW lasers formed. The earliest versions showed properties of a Fabry-Pérot (FP) optical cavity. Later, various modified versions of the FP cavity have been developed. In a FP cavity one has a gain medium with reflective mirrors forming an optical cavity [32, 16]. In a nanowire laser, the NW itself acts as the gain medium, and it is thus the end facets of the NW that should work as reflective mirrors [32]. The quality of the cavity can be described by the Q-factor of the laser [32],

$$Q = \frac{\lambda}{\Delta\lambda}.$$ (2.34)

The gain of the optical cavity can be expressed as [32]

$$g = \frac{1}{2L_c}\frac{1}{ln(R_1 R_2)},$$ (2.35)

where L_c is the cavity (in this case the NW) length and R_1 and R_2 are the reflectivity of the two end facets of the NW [32]. Nanowires with a FP cavity need waveguided emission to enhance feedback in the optical cavity [33] . This means that if the NW's diameter is less than a certain threshold, then the wave guide confinement will be insufficient and lasing will not be possible. The gain of one photon round trip has to be larger than the structural losses and losses because of imperfections in mirrors for lasing to occur [16]. These lasing criteria can be expressed in a simplified expression [16, 28]:

$$\Gamma g > \alpha_m + \alpha_p = \frac{1}{2L}\ln\left(\frac{1}{R_1 R_2}\right) + \alpha_p$$ (2.36)

Equation (2.36) is a simplified expression, but it states that the confinement factor of the nanowire, Γ, and the gain g, has to be larger than the loss terms α_m and α_p for mirror imperfections and propagation through the crystal structure respectively. The confinement factor is defined as the ratio between the optical energy of the gain medium and the total guided mode [6]. In Maslov 2004 [6], the confinement factor of a nanowire is believed to to become higher than unity, and that it is this that makes lasing possible in a nanowire.

Alternatively and preferably (for practical devices) the lasers can be electrically pumped, in contrast to optically pumped NW lasers, which are excited by external photons. For most laser applications it would be more practical with electrical pumping. The principle behind electrically pumped lasers is that lasing is achieved by electrically injecting electrons and holes into the laser structure. This is, however more complicated to achieve than optically pumped lasers, as electrical contacts have to be connected to the nm-sized structures.
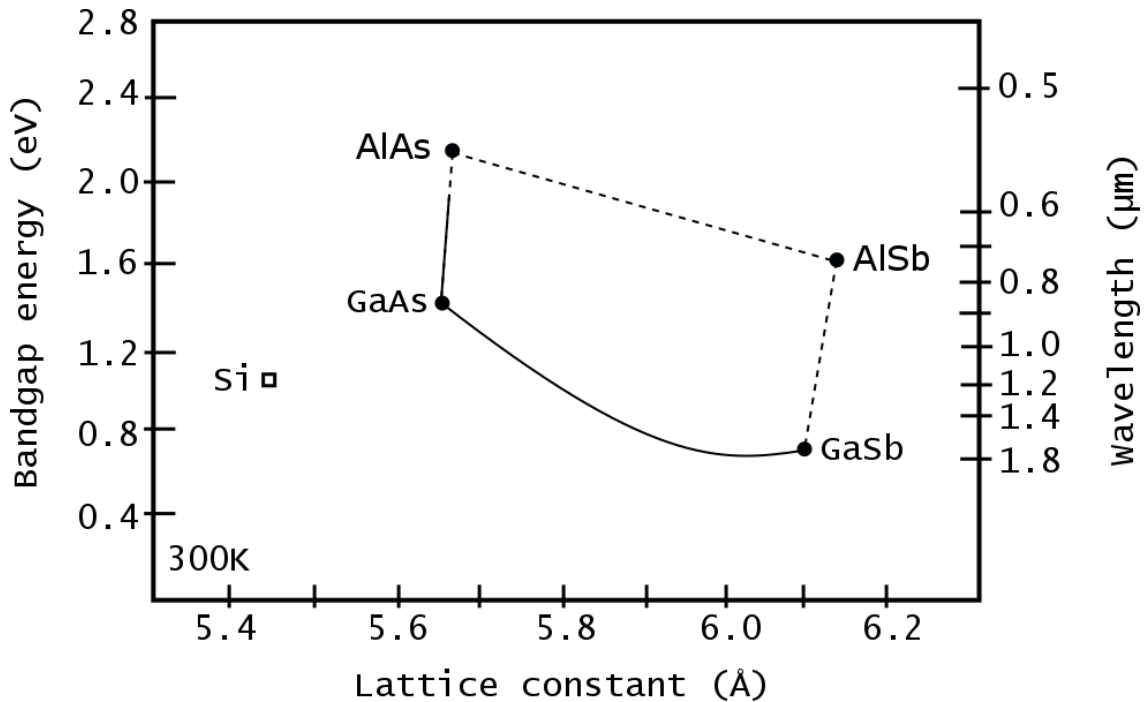

Figure 2.13: The bandgap energy E_g versus the lattice constant a at room temperature of the semiconductor alloys used in the NWs presented in this thesis. The curves represent the used alloys, where a solid line represents a direct bandgap and a dashed line represents an indirect bandgap. Adapted from [16]

Quantum well (QW) nanowire lasers have been emerging in different versions the last two decades [11, 12]. Here, the simplest semiconductor heterostructure system, the quantum well, is exploited. A quantum well consist off a thick (several houndred nm) layer of a semiconductor material with a larger bandgap, as for example GaAs. Then a 2-100 nm thick layer of a semiconductor material of a smaller bandgap, like GaAsSb (Figure 2.13), will be added, before another layer of GaAs is followed. The low BG material (GaAsSb) will serve as a potential well between the two stretches of higher BG material (GaAs), which serve as barrier material. Such an insertion of GaAsSb into a GaAs structure, will become a QW. A series of such QW is called a semiconductor superlattice (SL). The barrier material has to be thin enough to let the carriers tunnel between the QWs. This result in conduction band and valence band edges as illustrates in Figure 2.14. Transitions between holes and electron sub-bands will cause optical absorption or emission of a QW.

QWs are often used for opto-electronic applications, such as making of lasers and LEDs, for several reasons. One reason is that the optical transition energy can be tuned by varying the width of the QW, as well as it can provide a more efficient recombination process and eliminating some of the complications regarding scattering. Nanowire designs with multiple quantum wells have been made with both axial NW heterostructures [27] and radial heterostructures[12]. The NWs to be discussed in this text have an axial superlattice heterostructure of GaAs/GaAsSb. The crystal band structure, the effective bandgap and the lattice constant of a semiconductor material (Figure 2.13) determines which combination of materials that are suited for a heterostructure, like the superlattice. As opposed to the ruby laser, witch has a fixed wavelength, the emitted wavelength of a QW laser can be tuned. This is done by changing the size of the wells in case of confinement effects or by modifying composition to change the material bandgaps.
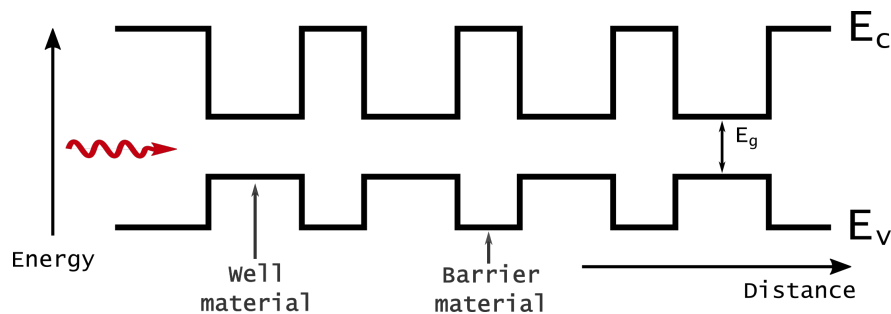

Figure 2.14: Schematics of the band edges in a semiconductor superlattice. Illustration adapted from [16]

Chapter 3

Experimental details

3.1 Nanowire structure

The NWs used in this works displayed lasing (Appendix E). In the theory on lasers from Chapter 2, heterostructured lasers with superlattice (SL) structure was mentioned. As NW lasers act as both gain region and FB cavity, and based on earlier growth trials, the intended NW design consisted of six regions with a GaAs/GaAsSb superlattice structures of length L, as illustrated in Figure 3.1. Each Superlattice consists of ten GaAsb wells of length l_W, and nine GaAs barrier regions of length l_B (Figure 3.1). These six SLs are separated by larger GaAs spacers, that were grown with the initial intention to stabilize the growth conditions. The superlattices are numbered from 1 to 6, with SL-1 at the bottom of the NW, and SL-6 near the tip. Spacers are numbered after the SL it follows, as marked in Figure 3.1. More details are given in [34]
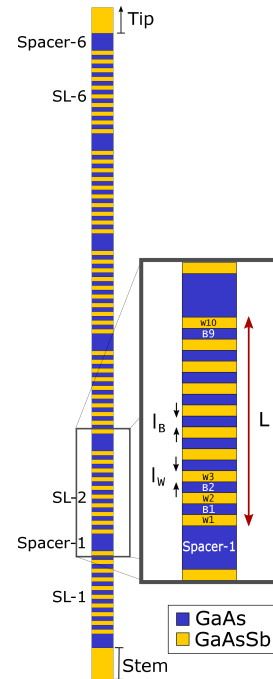

Figure 3.1: Schematics of the target structure for the NW superlattices structures and the terminology of the different regions.

3.1.1 MBE and Growth details

The NWs studied in this text were grown in the MBE laboratory at NTNU, using a a Vecco GEN 930 system. This MBE machine has effusion cells and valved cracker cells for introducing respectively the group-III elements and group-V elements to the growth chamber.

In this works, nanowires from four different batches with growth process variations were examined; SCN 40, SCN 43, SCN 45 and SCN 34. All the sample batches were grown at a temperature of 625°C. For all the samples, there was a step with Ga pre-deposition for 45 seconds with a Ga deposition rate of 0.7 ML/s. This step was followed by the growth of a GaAsSb stem with growth time of 1 minute, Ga depostion rate of 0.7 ML/s, and As_2 and Sb_2 fluxes of $2.5 \cdot 10^{-6}$ Torr and $1 \cdot 10^{-7}$ Torr respectively, as this gives a higher yield of vertical NWs [35]. After this, a GaAs segment was grown before the GaAsSb-based superlattices were grown under growth parameters represented in Table 3.1. An error occured during the programming of the growth conditions of sample SCN 34, and the excact Sb flux and GaAsSb growth time is therefore not known. However, the sample is included as it displayed interesting properties to be presented and discussed in further chapters.

The superlattice structure was made by growing segments of GaAs by opening the Ga and As knudsen cell shutters and segments of GaAsSb by opening the As and Sb shutters, systematically for 10 repetitions. A GaAs spacer was grown for 5 minutes with Ga rate of 0.7 ML/s and As_2 fluxt of $2.5 \cdot 10^{-6}$ Torr, before a new SL was grown. Six such SL growth processes were executed, creating six fields of GaAsSb-superlattices separated by GaAs spacers. After all six superlattices were grown, the Ga catalyst droplets were solidified under As_2 flux of $1 \cdot 10^{-5}$ Torr for 15 minutes.

An 14 nm thick $Al_{0.3}Ga_{0.7}As$ (nominal composition) shell and a GaAs cap of 6 nm were then grown on to the NW consecutively, at 625°C, after solidification of the Ga catalyston to the NW. This was done to passivate surface states an improve the optical properties [14]. The shell Al-GaAs shell is to prevent surface states, as the bandgap energy of AlGaAs is much larger than GaAs and GaAsSb, see Figure 2.13. The $Al_{0.3}Ga_{0.7}As$ shell was grown under an Al flux of 0.1 ML/s, a Ga flux of 0.2 ML/s and As_2 flux of $1 \cdot 10^{-5}$ Torr for 30 minutes. The GaAs cap was grown under a Ga flux of 0.2 ML/s and an As_2 flux of $1 \cdot 10^{-5}$ Torr for 15 minutes. The cap is to protect the shell from being oxidized, revealing the bare NW core and allowing trapped surface states.

Table 3.1: Growth parameters for the GaAsSb-based superlattices

Intern label	Sample	Sb_2 flux (Torr)	As_2 flux (Torr)	Ga rate (ML/s)	GaAsSb growth time (s)	GaAs growth time (s)
SCN43	A	$3 \cdot 10^{-7}$	$2.5 \cdot 10^{-6}$	0.7	10	96
SCN 40	B	$1 \cdot 10^{-6}$	$2.5 \cdot 10^{-6}$	0.7	10	96
SCN 34	C	NA	$2.5 \cdot 10^{-6}$	0.7	NA	96
SCN 45	D	$1 \cdot 10^{-6}$	$2.5 \cdot 10^{-6}$	0.7	20	96

3.1.2 Specimen preparation

The NW specimen were put on a 300 mesh holey carbon TEM grid. The sample was prepared by scraping a small part of a wafer with NWs grown, and then gently swipe the carbon side of a holey carbon grid over the scraped area. The NWs that were broken off the wafer after scraping, would then be transferred to the holey carbon grid. An optical light microscope was used to inspect the grid to make sure that a sufficient amount of NWs had landed on the grid. If so, the specimen would be ready for TEM inspection. Otherwise, the procedure is repeated.

A crucial part of the sample preparation is to thoroughly clean the tweezers and the scraping tool both before handling a sample and in between handling different samples. This is, firstly, to avoid as much contamination as possible, but, more crucially, to prevent any mixing of specimen from different batches by transfer of old sample residue onto a new sample of another NW batch.

3.1.3 Microscopy, Structual characterization and Data processing

The data in this work was gathered using a JEOL JEM-2100 transmission electron microscope (TEM) with an LaB_6 filament and an electron beam energy of 200 kV. The specimen were placed in a double tilt low background (Be) holder for TEM inspection (JEOL EM-31640).

The DF, BF, DP and HR TEM images were captured by the use of a Gatan 2k Orius^{TM} CCD camera. Gatan's Digital Micrograph (2.32.888.0) has been the primary software for TEM image processing [36]. Inkscape (0.91) was used to merge images and edit them for a presentable layout [37].

Chapter 4

Results

This chapter will present the structural characterization of nanowires from the four samples with different growth conditions presented in Chapter 3. Firstly, the general overview of the NW morphology and dimensions will be presented, followed by qualitative and quantitative phase mapping of the NWs based on DF-TEM images. This is followed by a presentation of other particular observations for these NW structures.

4.1   General observations

The four different sample NWs were studied using conventional TEM, where all samples showed a similar morphology, but with slight variations in length and diameters (Table 4.1). All the NWs are relatively straight and thick. The thickness changes throughout the NWs with an increasing trend towards the tip. Thus, all the sample NWs have (to some degree) an anti-tapered morphology. Table 4.1 shows the measured lengths of the representative NWs from sample A-D. The measured projected thicknesses of the NWs at the six different SL positions of the NWs are also shown in Table 4.1. In general, the NWs have a length of around 10 μm and a diameter of around 400-450 μm. HR-TEM lattice images of local shapes and surfaces of NWs will be presented in Section 4.3.

Table 4.1: Measured dimensional values of the representative nanowires from sample A-D. The projected widths of the NWs are measured at the end of each SL close to the following spacer.

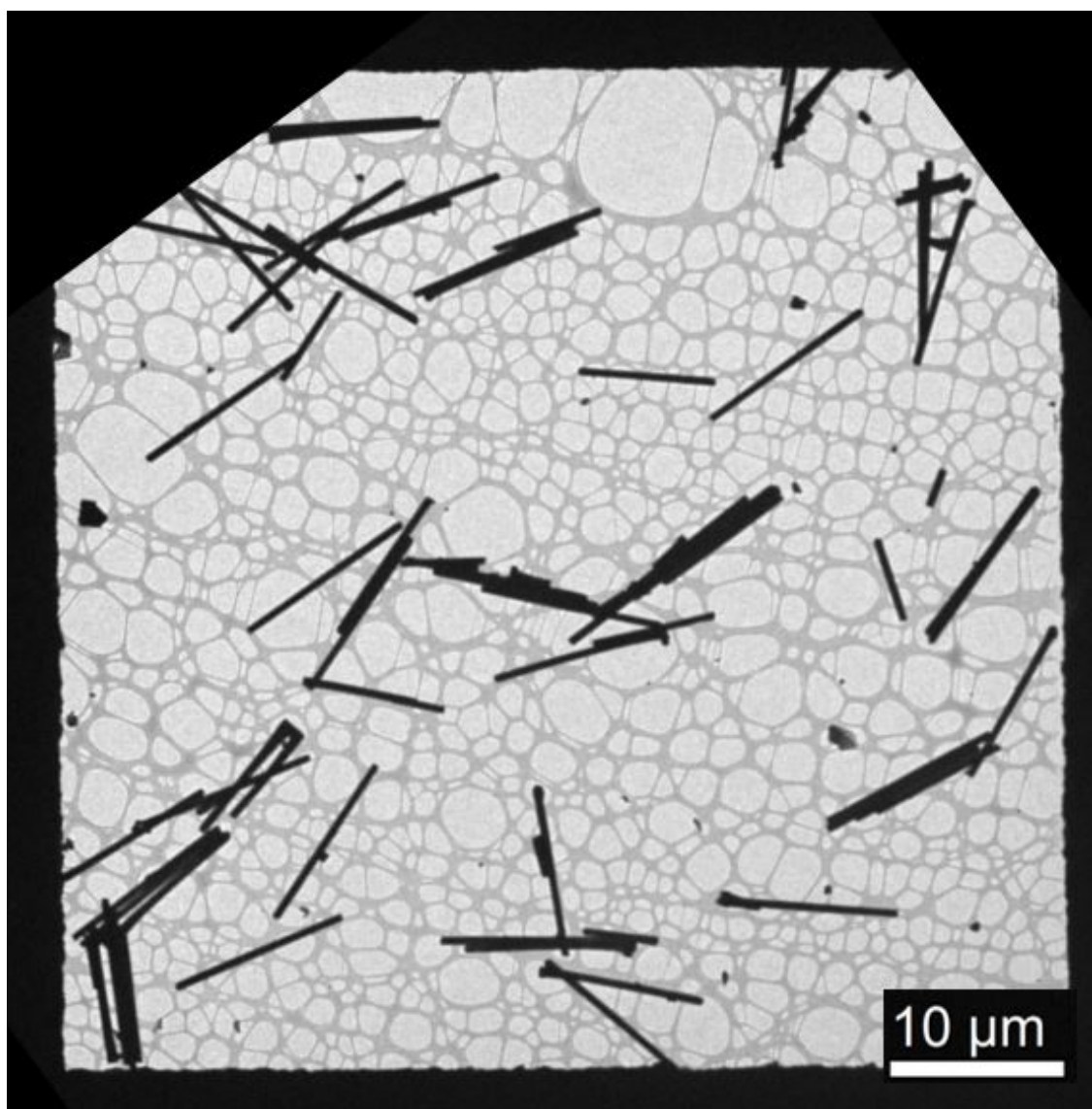| Sample	Length (µm)	Proj. width SL-1 (µm)	Proj. width SL-2 (µm)	Proj. width SL-3 (µm)	Proj. width SL-4 (µm)	Proj. width SL-5 (µm)	Proj. width SL-6 (µm)
A	11.15	0.38	0.37	0.38	0.41	0.46	0.45
B	10,45	0.40	0.41	0.41	0.43	0.46	0.47
C	9.75	0.42	0.42	0.44	0.44	0.45	0.46
D	9.51	0.39	0.39	0.41	0.43	0.42	0.42

Figure 4.1: Low magnification BF-TEM of a square of the mesh grid with NWs from sample B.

The NWs within one sample are similar in the sense that they are straight with seemingly similar thickness, as seen in Figure 4.1. Some NWs are shorter, and are believed to have broken off above SL-1. Other NWs have grown together with another NW, which might be a result of two NWs grown from the same substrate hole, but most are long and single NWs. Overall, the NWs within one sample seem to have the same general morphology in the way that they are straight and long with similar thickness.

The BF-TEM images in Figure 4.2 shows the tips and bottoms of the NWs from sample A-D. Facets with certain angles are dominant for the NW tips. Angles of around 19 degrees and around 35 degrees (with respect to the 111-plane) are reoccuring for all four NWs (marked with respectively purple and green arrows in Figure 4.2). The foot shape of (e) was found in other samples as well, but the bottoms displayed in (f)-(g) were most commonly found, and also present in sample A. All four NW bottoms display a chipped or cut edge on one side of the projected image of the NWs (marked with dotted circles in Figure 4.2). Figure 4.3 show HR-TEM lattice images taken of the sample D NW tip.
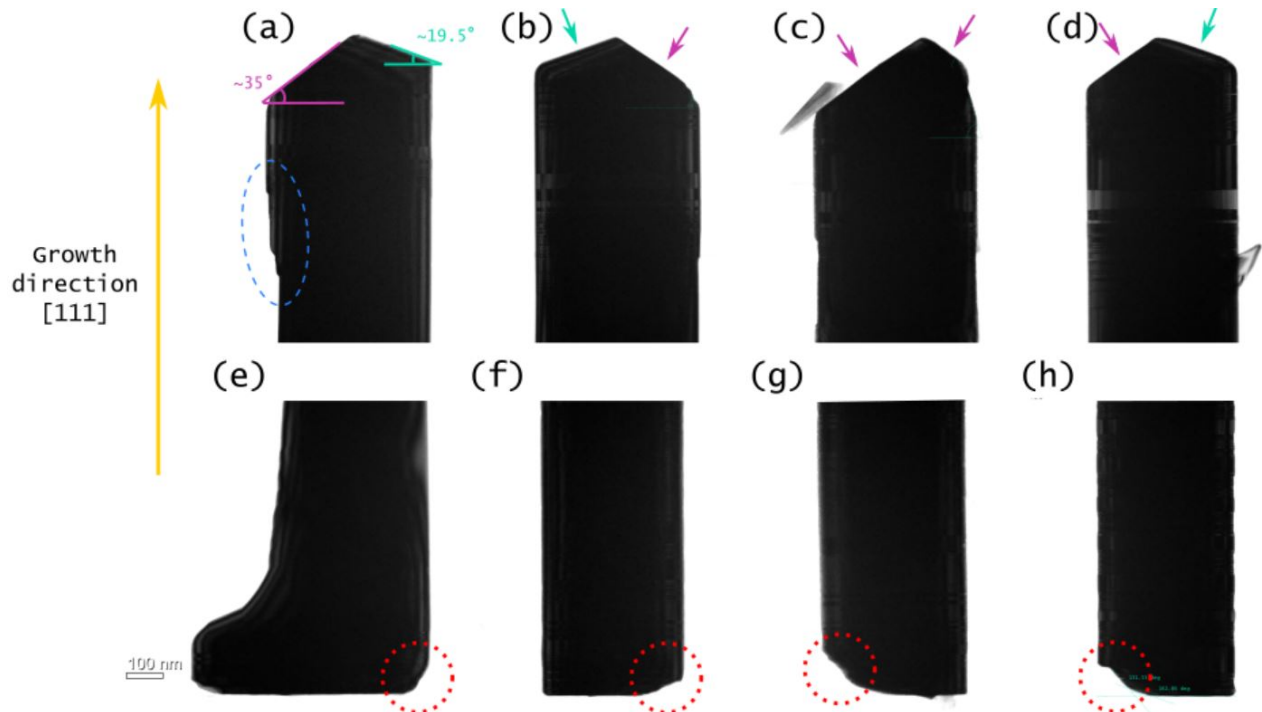

Figure 4.2: The tips ((a)-(d)) and bottoms ((e)-(h)) NW samples A-D. (a) and (e) is sample A, (b) and (f) is sample B, (c) and (g) is sample C, and (d) and (h) is sample D.
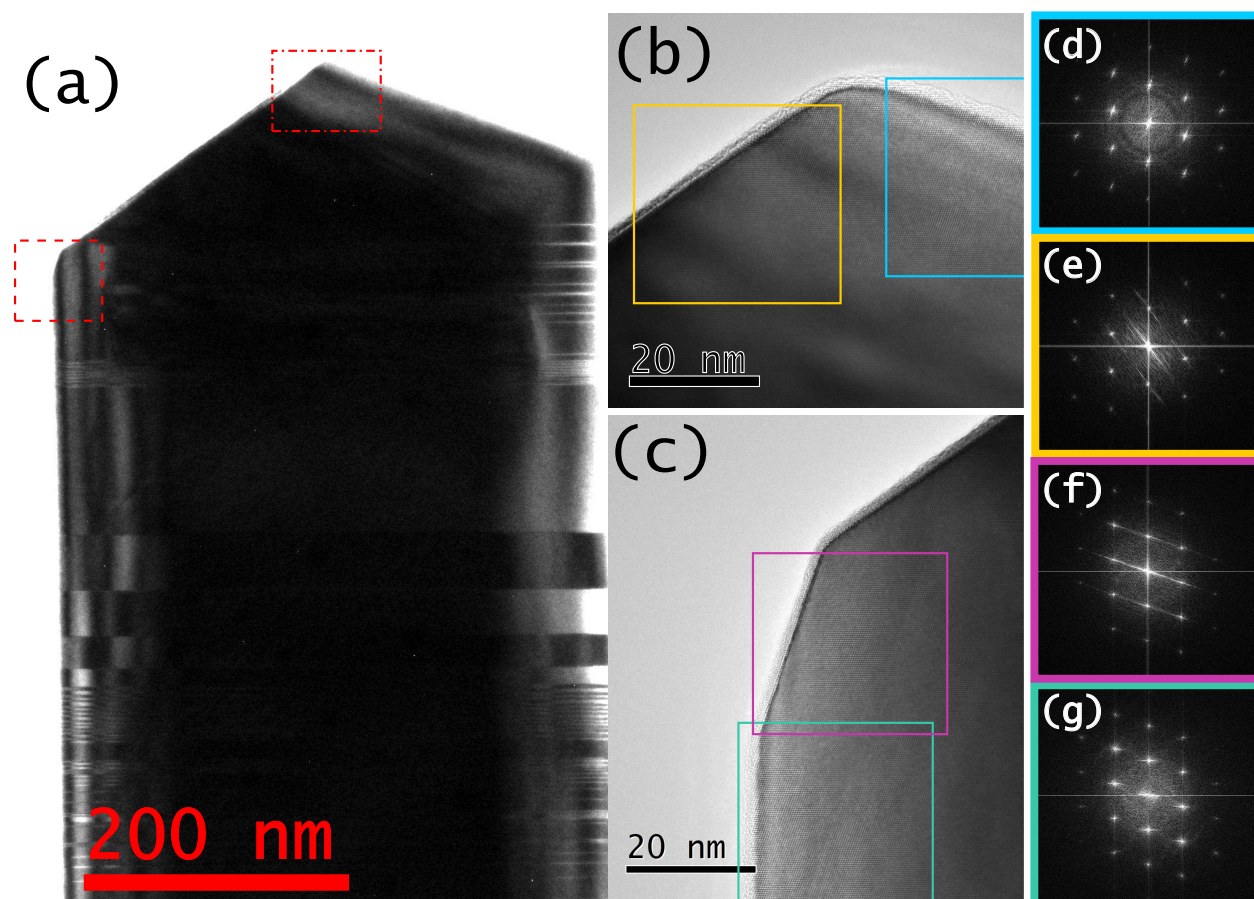
Figure 4.3: (a) BF-TEM of a sample D NW. (b) and (c) HR-TEM of respectively upper and lower square in (a). (d)-(g) FFT of the areas in (b) and (c) marked with respective color squares. The TEM images were taken by Ton van Helvoort on a JEOL 2100F.

4.2 Crystal phase mapping

The NWs characterized are relatively thick for TEM (400 nm). Entire NWs were imaged by DF-TEM, mapping the edges of the NWs, as the core is too thick for the electron beam to pass through. Some of the following DF images presented are therefore oversatuated to give a better presentation and overview. However, the measurements are based on the raw TEM images. In addition, HR-TEM was achieved at the projected edges of the NWs, where the NW is thin and the beam only passes through the AlGaAs shell. The shell is assumet to adapt the identical crystal structure of the NW core (including SFs), and is thus representative to map the crystalstructure of the NW [38].

The NWs were observed to have longer regions of WZ richer segments. These are concidered the spacer regions of the NW structure based on the target structure in Figure 3.1. The stretch between these WZ rich regions will be refered to as the superlattice. There are ten stretches of pure defect-free ZB phase in each SL. These will be refered to as the quantum wells, and the mixed phase segments separating them are the barriers (Figure 3.1). This will further be elaborated on in Chapter 5.

One representative NW from each of the four samples were analyzed in detail. These were NWs that contains all six supperattices, and are therefore considered to be whole NWs. The observed crystal phases within these NWs are considered to be representative for the sample. In the following subsections NWs from each of the four samples are presented.

4.2.1 Sample A

In Figure 4.4 a NW from sample A is presented. It was measured to be 11.21 µm long, with a measured thickness of 400 nm by the end of SL-1 and 450 nm by SL-6. This NW is the longest of the four concidered samples.

Sample A consists almost entirely of mixed phase regions, as phase shifts, stacking faults and twin planes dominates the SLs. The well regions are too small to destinguish from the barriers. Therefore, it has not been possible to measure the lengths of pure ZB segments and finite mixed phase lengths of the superlattices. There are regions of the NW that shows a higher concentration of WZ phase, which are concidered to be the spacer regions. However, their outstretch is too ill-defined to be measured.
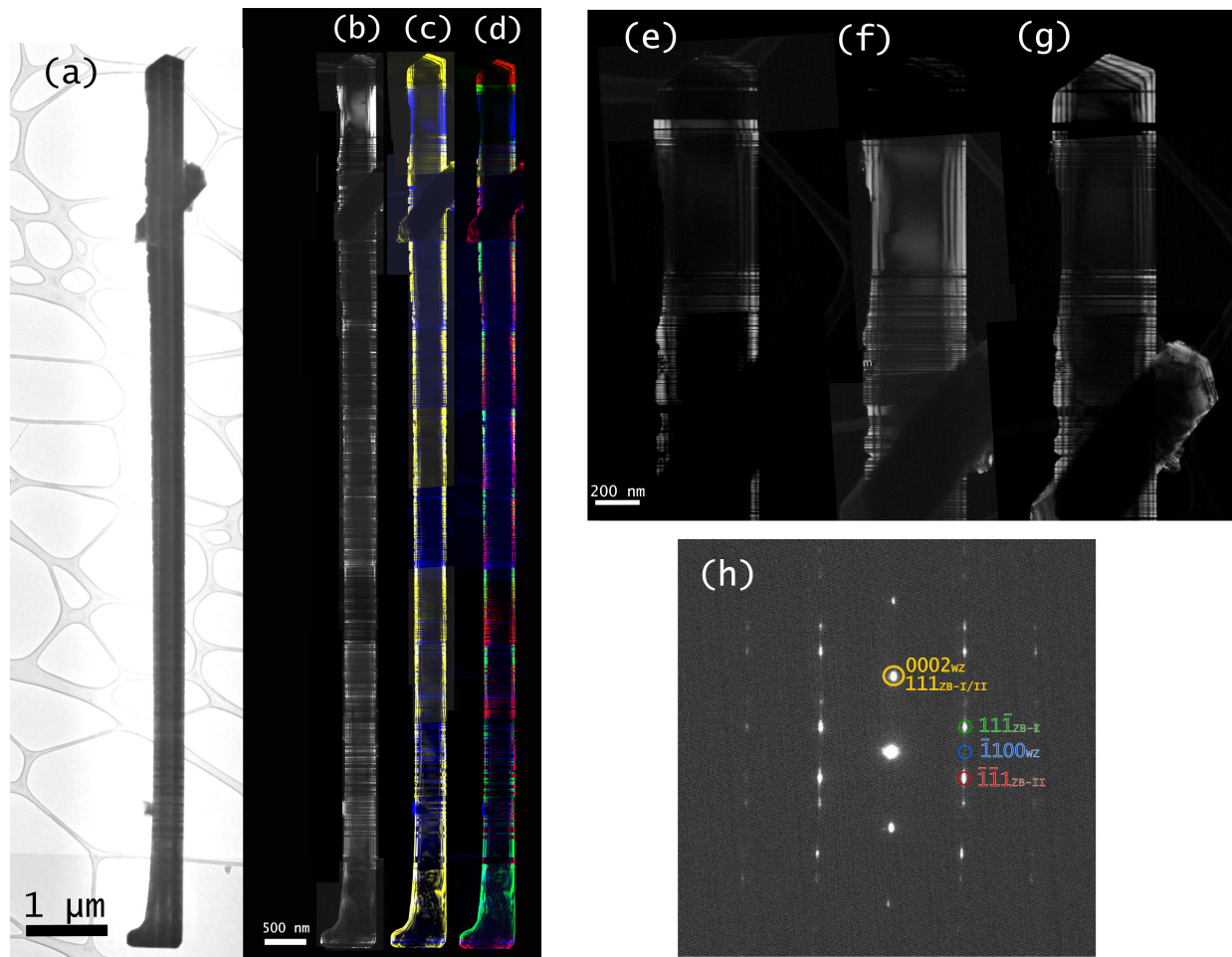

Figure 4.4: Overview of sample A NW. (a) BF-TEM of entire NW. (b)-(c) Entire NW constructed of 11 DF-TEM images from reflections from DP in (h). (b) $DF_{\bar{1}110WZ}$. (c) DF_{WZ} (blue) and DF_{ZB} (yellow). (d) DF_{WZ} (blue), DF_{ZB-1} (green) and DF_{ZB-2} (red). (e)-(g) DF images from spacer 5 and to the tip of the NW. (e) $11\bar{1}_A$. (f) $\bar{1}110$. (g) $\bar{1}\bar{1}1_B$.

4.2.2 Sample B

The sample B NW is 11.12 µm long, and is presented in Figure 4.5. The thickness of the NW was measured to 380 nm by the first spacer, and 470 nm by the sixth spacer. The average length of SL-3-5 is 1200 nm for sample B. The wells in these SLs were on average 65 nm long, while the barriers were on average 60 nm. Spacers between these SLs are on average 265 nm long.

Sample B is longer and has a smaller diameter than sample C and D. It also has more TPs and SFs, and the lowest ZB-to-mixed phase length ratio in the superlattices, as compared to the sample C and D NWs.
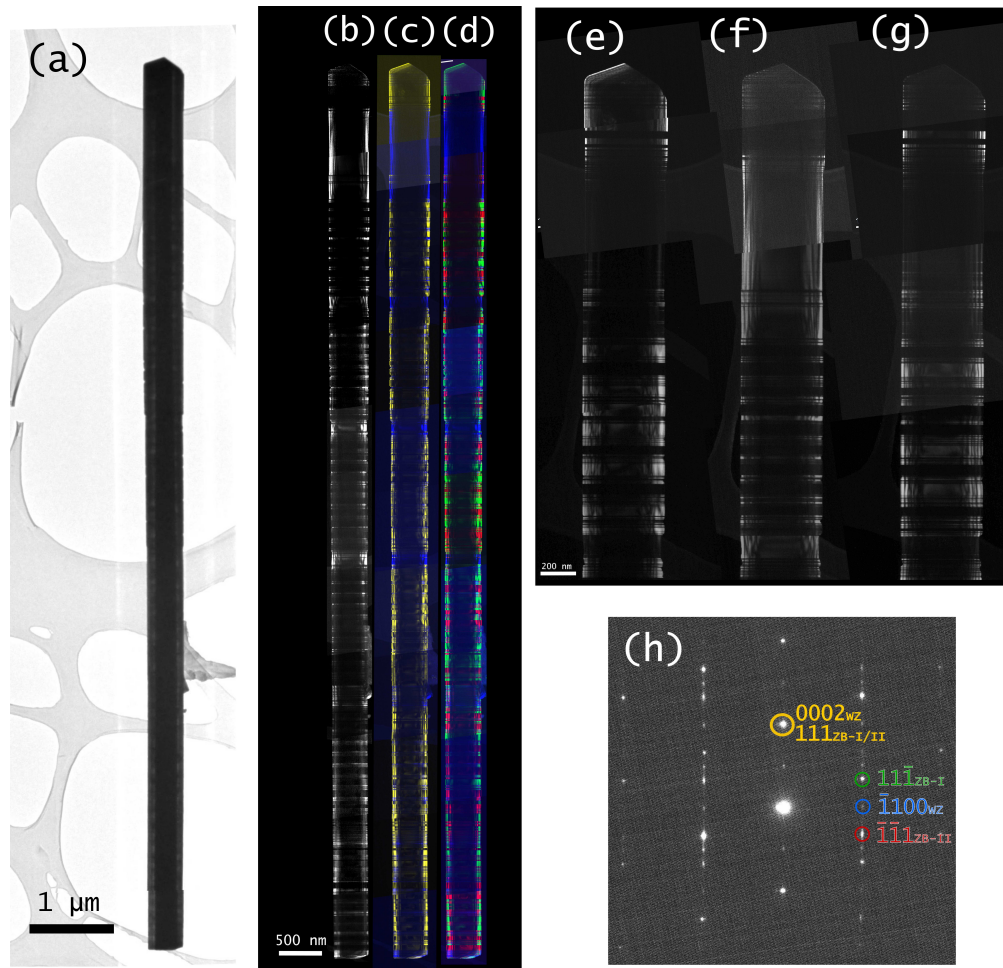

Figure 4.5: Overview of sample B NW. (a) BF-TEM of entire NW. (b)-(c) Entire NW constructed of 11 DF-TEM images from reflections from DP in (h). (b) $\text{DF}_{\bar{1}110WZ}$. (c) DF_{WZ} (blue) and DF_{ZB} (yellow). (d) DF_{WZ} (blue), DF_{ZB-1} (green) and DF_{ZB-2} (red). (e)-(g) DF images from spacer 5 and to the tip of the NW. (e) $11\bar{1}_A$. (f) $\bar{1}110$. (g) $\bar{1}\bar{1}1_B$.

4.2.3 Sample C

The NW representing sample C is 10.44 µm long, with a thickness of 420 nm near the bottom of the NW (SL-1) and 480 nm near the tip (SL-6), as displayed in Table 4.1, and is presented in Figure 4.6. The average superlattice length of SL-3-5 was found to be 1260 nm, with average well segment length of 75 nm and average barrier length of 55 nm. Average length of spacer-3-5 is 225 nm.
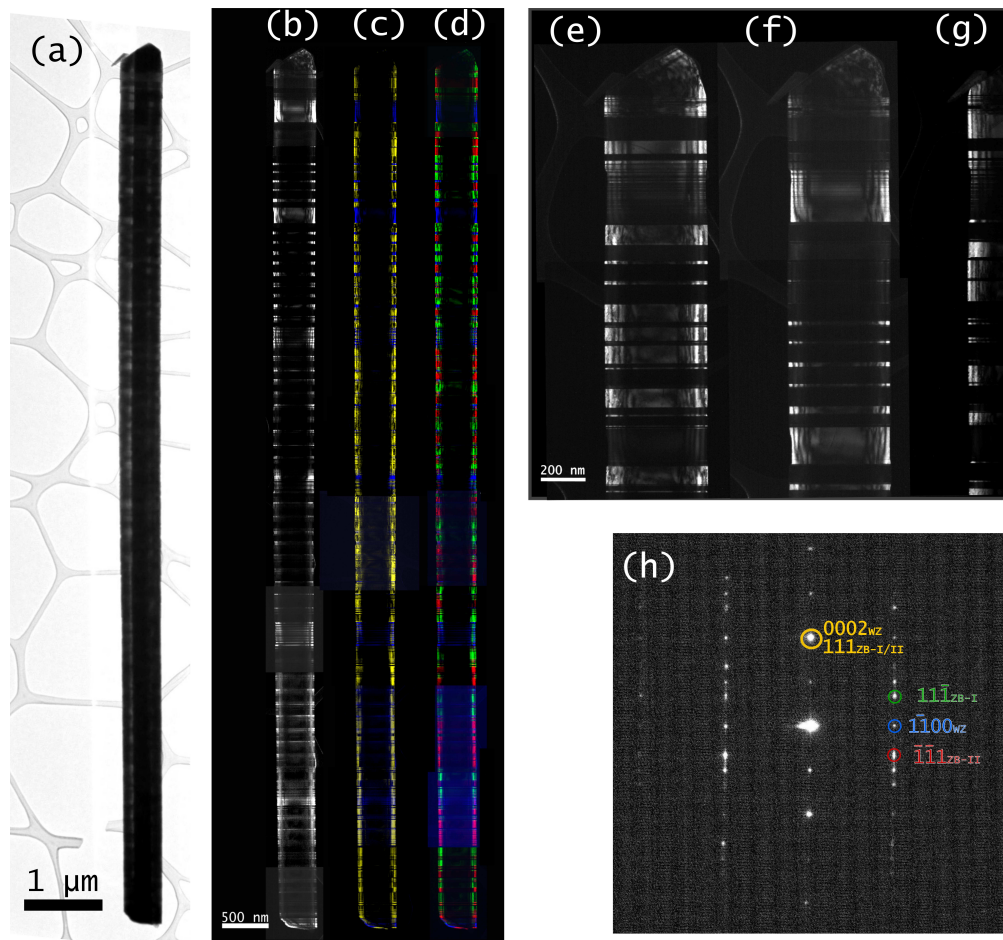

Figure 4.6: Overview of sample C NW. (a) BF-TEM of entire NW. (b)-(c) Entire NW constructed of 11 DF-TEM images from reflections from DP in (h). (b) $DF_{\bar{1}110WZ}$. (c) DF_{WZ} (blue) and $DF_{ZB}B$ (yellow). (d) DF_{WZ} (blue), DF_{ZB-1} (green) and DF_{ZB-2} (red). (e)-(g) DF images from spacer 5 and to the tip of the NW. (e) $11\bar{1}_A$. (f) $\bar{1}110$. (g) $\bar{1}\bar{1}1_B$.

4.2.4 Sample D

The sample D NW was measured to be 9.85 μm long, with a thickness of 430 nm near the bottom of the NW (SL-1), and 470 nm near the tip (SL-6) (Table 4.1). Sample D has generally less defects than samples A-C. When concidering SL-3-5, sample D has an average SL length of 1110 nm, while spacer-3-5 has an average length of 200 nm. In these SLs, the average length of the ZB segments is 80 nm, leading to a calculated average length of 30 nm for the mixed phase segments. The analyzed NW from sample D, is presented in Figure 4.4.

Sample D has the most stable WZ and ZB phase segments of the four samples. In the SL-1 and SL-2, the ZB and the mixed phase segments have similar lengths. In SL-1, $l_W < l_B$, while in SL-2, $l_W > l_B$. For the following superlattices, the l_W becomes larger while l_B reduce in size. The length of the SLs stay more or less constant throughout all six regions, ±100nm.
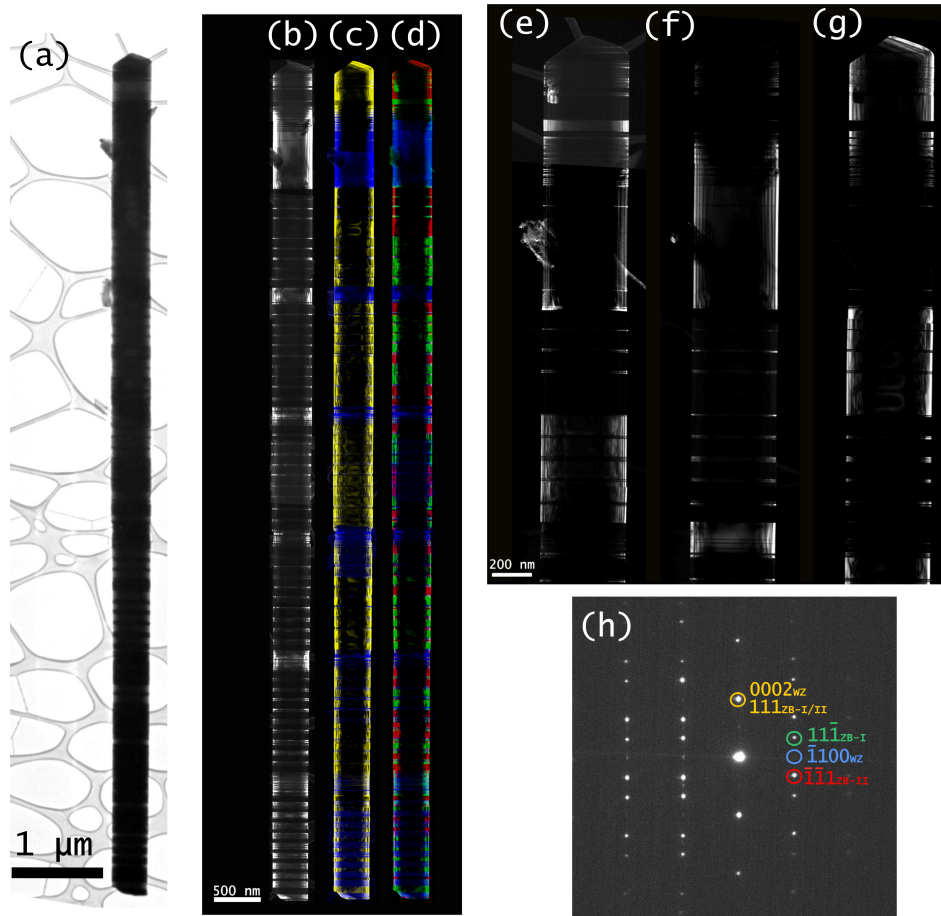

Figure 4.7: Overview of sample D NW. (a) BF-TEM of entire NW. (b)-(c) Entire NW constructed of 11 DF-TEM images from reflections from DP in (h). (b) $DF_{\bar{1}110WZ}$. (c) DF_{WZ} (blue) and DF_{ZB} (yellow). (d) DF_{WZ} (blue), DF_{ZB-1} (green) and DF_{ZB-2} (red). (e)-(g) DF images from spacer 5 and to the tip of the NW. (e) $11\bar{1}_A$. (f) $\bar{1}110$. (g) $\bar{1}\bar{1}1_B$.

4.2.5 Compared results

Two ZB phases are present in the NWs, denoted ZB_1 and ZB_2 for the two different orientations. The occurences of the two different ZB phases were counted in samples B-D and is presented in Figure 4.8, where ZB_1 is represented in green and ZB_2 in red (which is the color code used throughout the text). Some wells consisted of ZB phase with a TP occuring around the middle of the ZB segment. These are represented in gray in Figure 4.8. The occurence of ZB_1 versus ZB_2 seem to be random, as no pattern was found as to when either phase was prefered. Thus, no further inspection was conducted on this matter. However, the presence of TPs in the wells is higher in sample B than in sample C, with no occurences in sample D. Because of the mixed phase dominated phase structure of sample D, it's phase measurements are not in this, nor the following, comparisons.
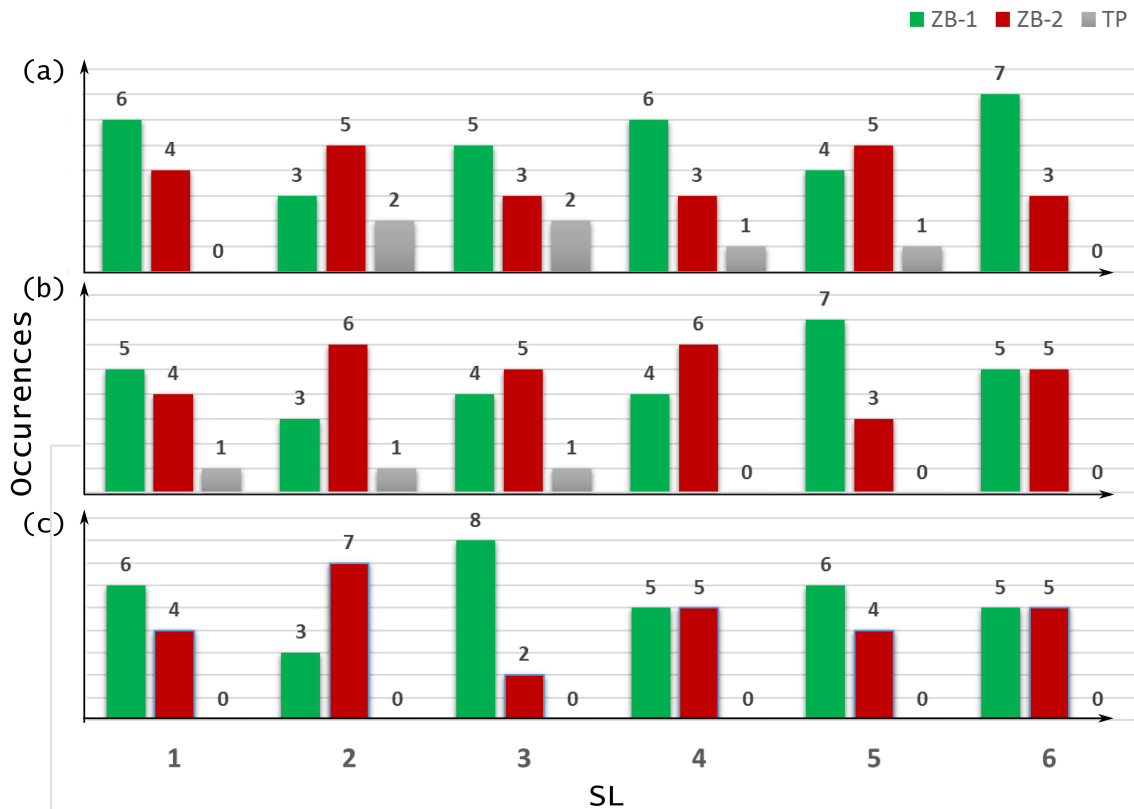

Figure 4.8: Diagram of the ZB_1 (green), ZB_2 (red) and TP (gray) occurences in the various SLs for (a) sample B, (b) sample C and (c) sample D.

The length of each superlattice of the sample B-D NWs, and the length of each complimentary spacers are plotted for each NW in respectively Figure 4.9 (a) and (b).
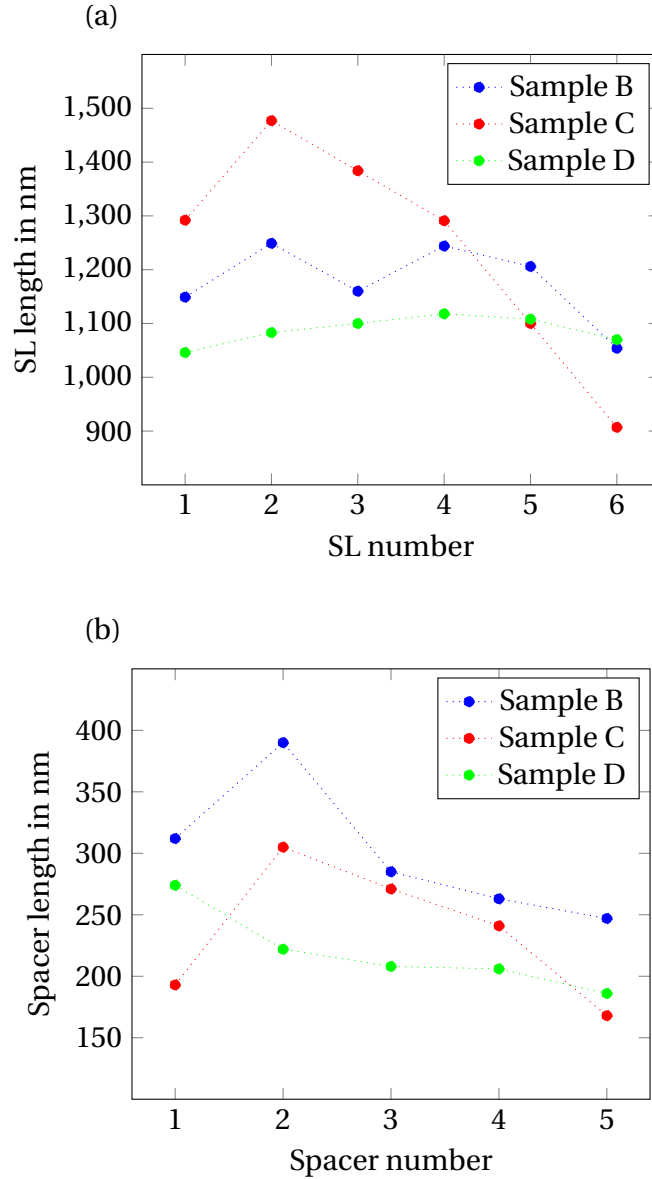

Figure 4.9: (a) measured length of each SL of samples B-D. (b) measured length of each spacer of samples B-D. All lengths are retrieved from the NWs respective RGB DF-TEM images.

For each superlattice, the average lengths of the wells (the defect-free ZB phase segments) were determined for samples B-D. These are displayed in Figure 4.10 (a). Figure 4.10 (b) shows the plotted values of the calculated average length of the mixed phase regions (barriers) separating the wells in the SLs, of the same samples. The l_B are estimated from the measured SL lengths and the average l_W of each SL. The data from these phase measurements can be found in Appendix A
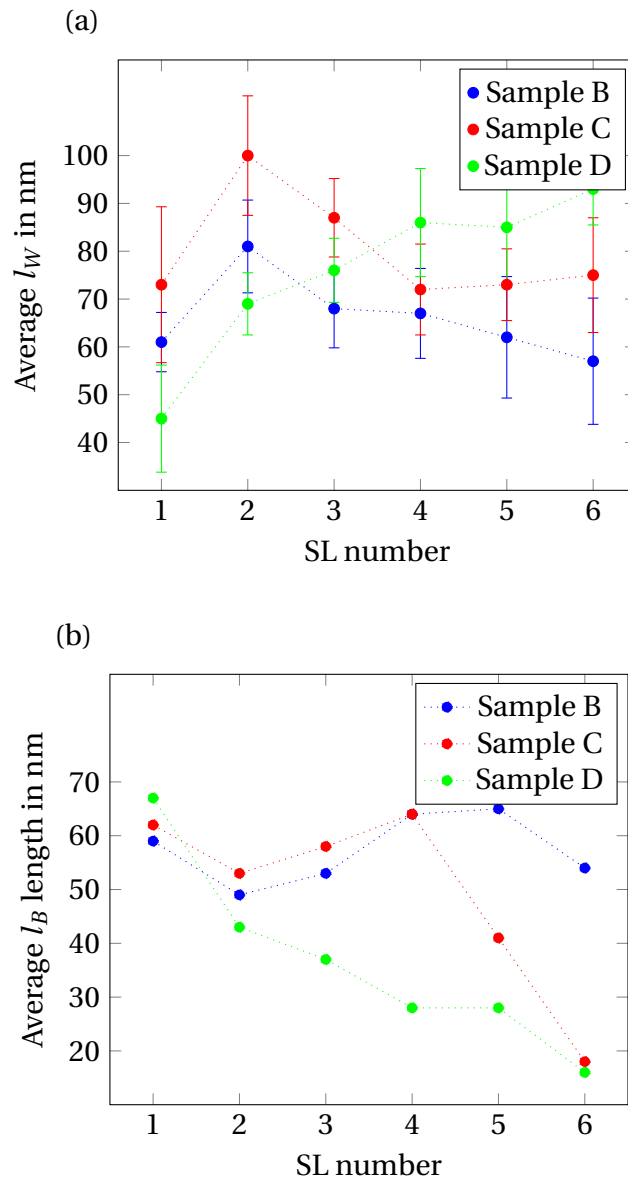

Figure 4.10: (a) the average (l_W) for each SL. (b) estimated (l_B) for each SL. The values are based on measurements from the NWs respective RGB DF images.

In Figure 4.11, the WZ phase DF-TEM image of SL-5 is displayed for comparison of each of the four samples. The Sb flux during NW growth increase from (a)-(b). Figure 4.11(d) has a longer GaAsSb growth time than (a) and (b), but the same Sb flux as (b). The growth parameters of Figure 4.11(c) are unknown. The length of the WZ segments in spacer-4 and spacer-5 was measured for each samples, and compared with the total spacer length $l_{spacer-n}$, for spacer number n, and can be found in Table 4.2.
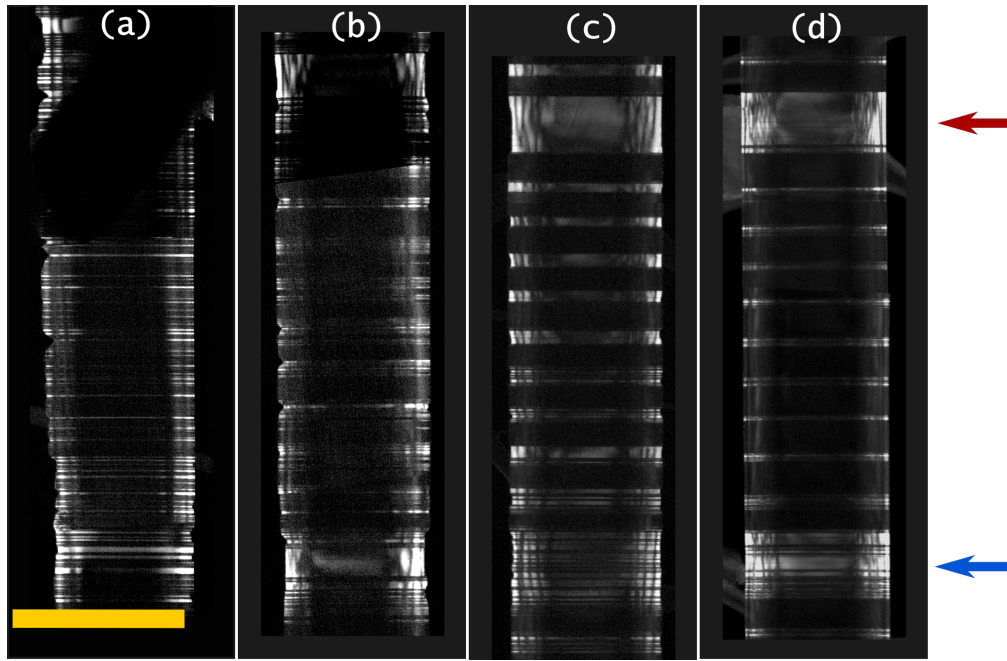

Figure 4.11: DF images of reflection $\bar{1}100$ (WZ) showing spacer-4 (blue arrow) to spacer-5 (red arrow) of (a) NW from sample A, (b) sample B, (c) sample C and (d) sample D. Scalebar is 500 nm

Table 4.2: Measured length of WZ phase segments of spacer-4 and spacer-5 of sample B-D, compared with the total spacer lengths $l_{spacer-n}$ of the corresponding samples.

Sample	$l_{spacer-4}$ (nm)	spacer-4 WZ (nm)	$l_{spacer-5}$ (nm)	spacer-5 WZ (nm)	Total WZ (nm)	WZ% of total l_{spacer}
B	275	145	255	160	305	57%
C	260	105	180	160	265	60%
D	200	110	180	155	265	70%

4.2.6 HR-TEM images

To further investicate crystal structure and defects of the sample NWs and as comparioson to DF-TEM , HR-TEM lattice images were taken of the sample NWs represented previously in this section. As sample D shows the most stable phase properties, some of it's HR images are presented in this section. The HR-TEM images gathered from sample A-C can be found in Appendix B, and some are presented in Section 4.3 to be discussed later in the text. The HR images compilation of sample D depicted in Figure 4.12 maps the end of SL-4 to the start of SL-6. 20 HR images were needed to map the whole length of superlattice 5 and spacer-5.
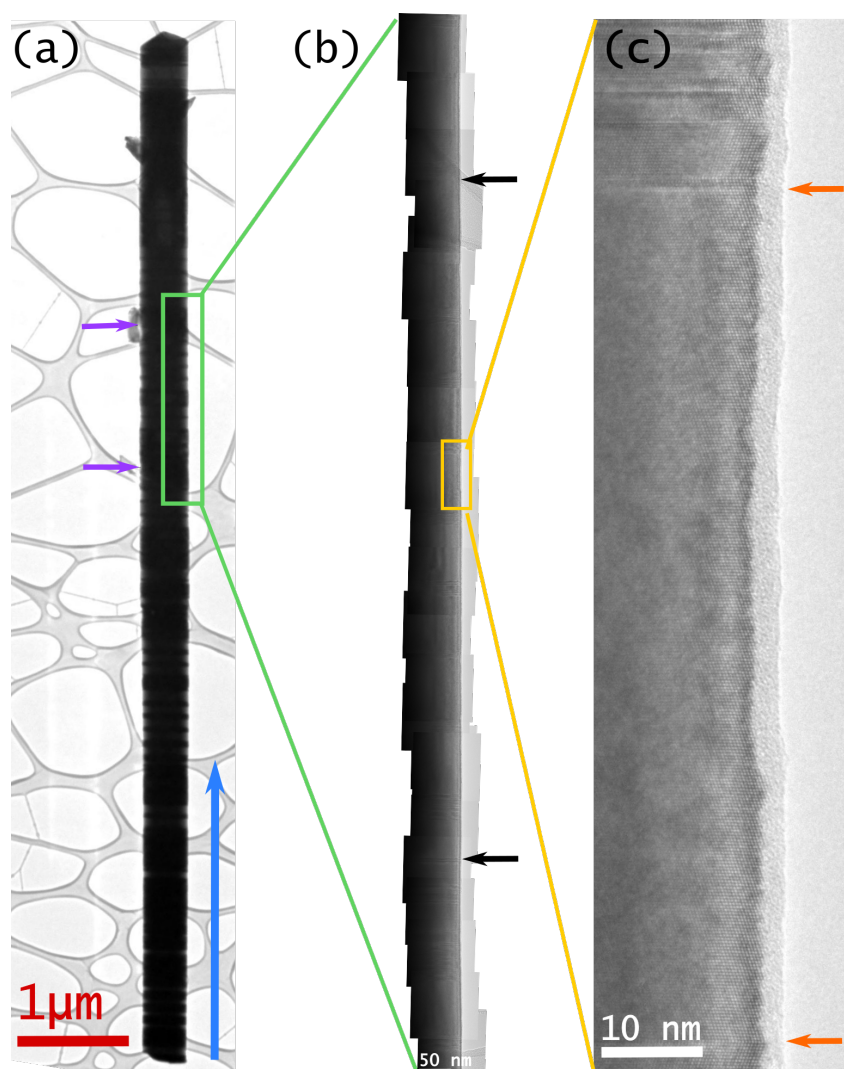

Figure 4.12: (a) BF-TEM image of Sample D NW. Blue arrow mark 111_B growth direction. Purple arrows indicates start and end of SL-5. (b) compilation of 23 HR-TEM images marked by green square in (a). Black arrows mark start and end of SL-5. (c) HR-TEM image of area within yellow square in (b). Orange arrows mark start and end of well-6 and SL-5.
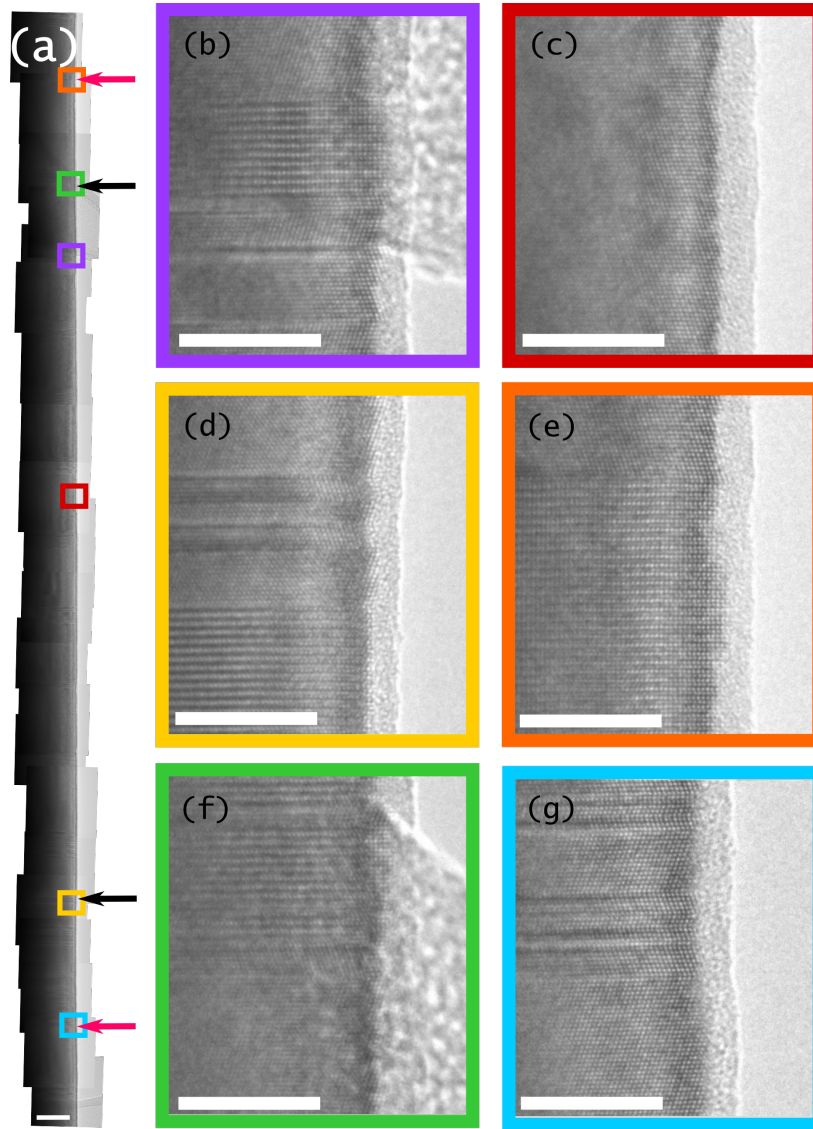
Figure 4.13: (a) compilation of HR-TEM images of sample D NW. Black arrows mark start and end of SL-5. Red arrows mark transition from SL-4 to spacer-4 (bottom), and spacer-5 to SL-6 (top). Colored squares in (a) mark locations of HR-TEM images (b)-(g), displaying the following regions: (b) B9 in SL-5, (c) middle of W6 in SL-5, (d) spacer-4 end, (e) spacer-5 end, (f) spacer-5 start, (g) spacer-4 start. White scale bars indicate 10 nm.

Figure 4.13(d)-(g) displays the HR-TEM images of the crystal planes at the start and end of spacer-4 and -5. The well segment (W6) in the middle of SL-5 is shown in Figure 4.13 (c). The well segment is ZB phase and defect-free. Figure 4.13(b) dispalys the barrier region (B9) between two wells, revealing a mixed phase region containing phase shifts, with a mix between WZ phase segments, TPs and SFs.

4.2.7   DF vs HR imaging

The various crystal phases and regions have been measured from DF-TEM images (Section 4.1). To find the resolution or uncertainty of these measurements, DF-TEM has been compared with HR-TEM for the same area of the same NW, as presented in Figure 4.14. The WZ lattice constant, c, of GaAs has been reported to be 6.57 Å [39]. This was used to calibrate the HR image. By using the newly defined pixel size from this calibration, the DF image of the same NW area was calibrated. The profiles of the area and the respective HR and DF images can both be seen in Figure 4.14.
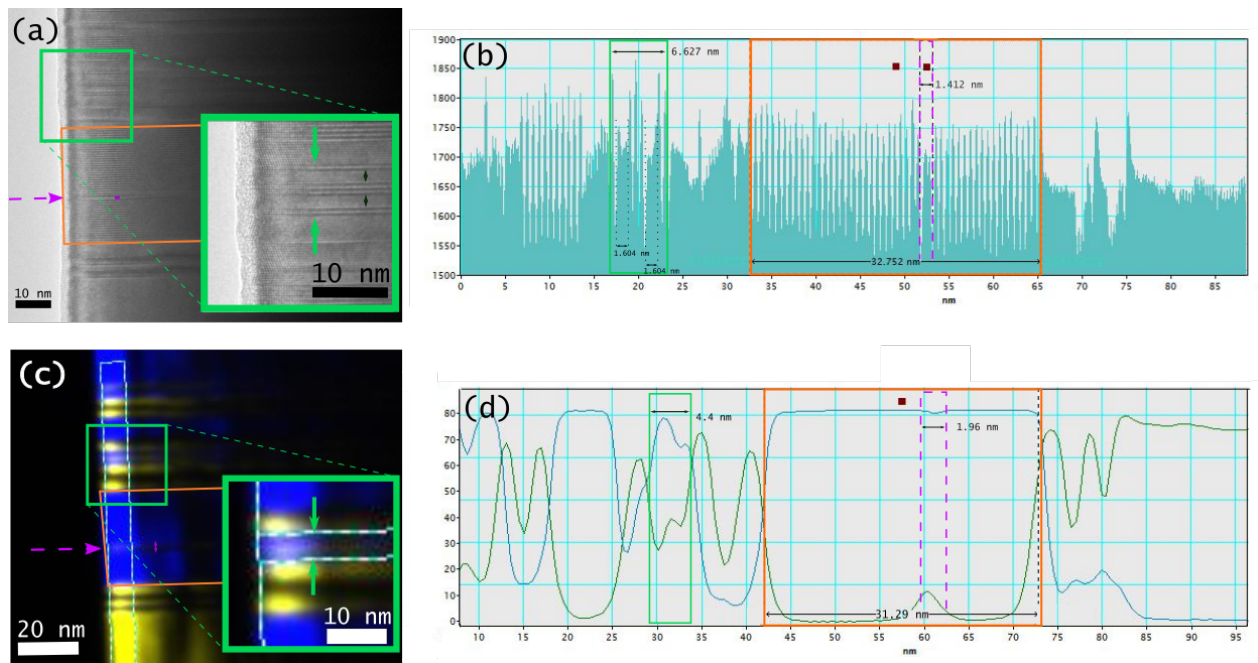

Figure 4.14: Data of spacer-4 from sample D. (a) HR-TEM image, (c) DF-TEM image, and (b) and (d) display the intensity profiles of (a) and (c) respectively. The green, pink and orange marked area represent the same regions in (a)-(d).

4.3   Various observations

The NWs analyzed contained different features and defects that have been studied using both DF-TEM and HR-TEM lattice images. Some features and defects observed are displayed in Figures 4.15 to 4.18 and **??**.

The analyzed NWs showed some circular features near the bottom of the NW in SL-1, as shown for the case of sample C in Figure 4.15. The features are only observed in the ZB phase segments of the DF-TEM images, with one in each larger phase stretch. The circular features are all oriented around the core of the NWs. The features closest to the bottom of the NW is the smallest, and then grow in radial direction towards SL-2. This same trending feature was found in samples B-D.
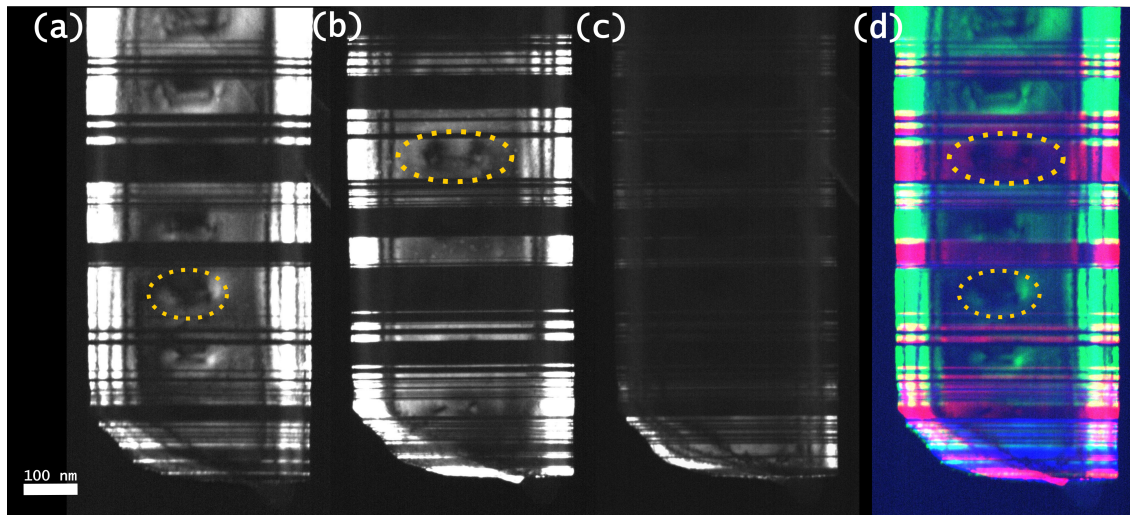

Figure 4.15: DF images of the bottom region of NW sample C. (a) $DF_{11\bar{1}_{ZB-1}}$. (b) $DF_{\bar{1}\bar{1}1_{ZB-2}}$. (c) $DF_{\bar{1}110_{WZ}}$. (d) RGB DF composition of (a), (b) and (c) reflections. The images are oversatuated to reveal the features along the middle of the NW.

To study the effects of relative electron beam direction to the NW surface planes, a NW from sample D was studied in both the original [110] beam direction and a [112] beam direction by tilting the sample 30 degrees around the growth axis. Figure 4.16 presents the BF-TEM images of the NW with beam direction [110] displayed in (b) and [112] displayed in (d). RGB images, from DF images of spacer-5, are presented in Figure 4.16(e) for [110] and (f) for [112], with their respective DPs in (g) and (h).
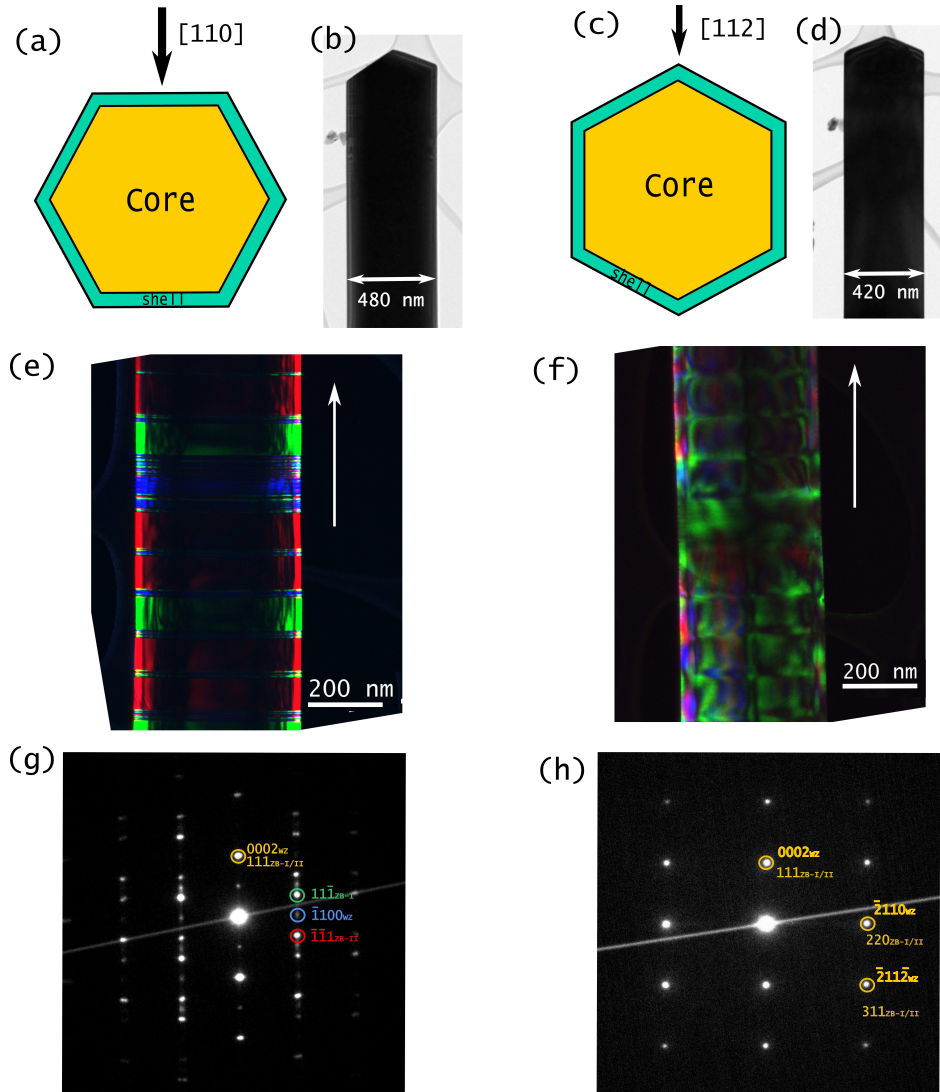
Figure 4.16: Sample D before and after a 30 degrees tilt. (a) and (c) illustrates the crossection of the core shell NW and it's different orientations with respect to beam direction [110] and [112], respectively. (b) and (d) shows NW tip area for respectively beam direction [110] and [112]. (e) and (f) is the RGB DF-TEM of spacer-5 with beam directions [110] and [112] respectively. The diffraction spots used for the two RGB images are indicated on the respective DPs in (g) and(h).

Figure 4.17 shows some other types of defects that were seen in different degrees of prominance in all the NWs analyzed. These local changes in NW thickness have been observed in areas with phase changes with WZ phase or mixed phase regions, most commonly seen in between two defect-free ZB phase segments or at the start and end of a spacer region. Figure 4.17(b) displays a particularly prominant case in between two ZB phase segments in SL-5 of the sample B NW. From the HR-TEM lattice images, this difference in prominance varies withing one NW, but there is also a difference between the samples. Sample B has the most prominant cases of this width change, while sample D show very little change in projected width of the NW. Sample A show such thicknedd variations with both moderate and prominant nature, and sample C show defects with moderate prominance. However, the changes in diameter of sample C NWs might be caused by an other factors than for the other NWs, as presented in the following paragraph and discussed in Chapter 5.

From HR images of the sample C NW some featurs were observed that were not seen in the other samples. Some of these features can be seen in Figure 4.18, where the HR image of a region in SL-4 is displayed. These features were only seen in sample C NWs, and were observed along the entire length of the NWs with a relatively eaven distribution.
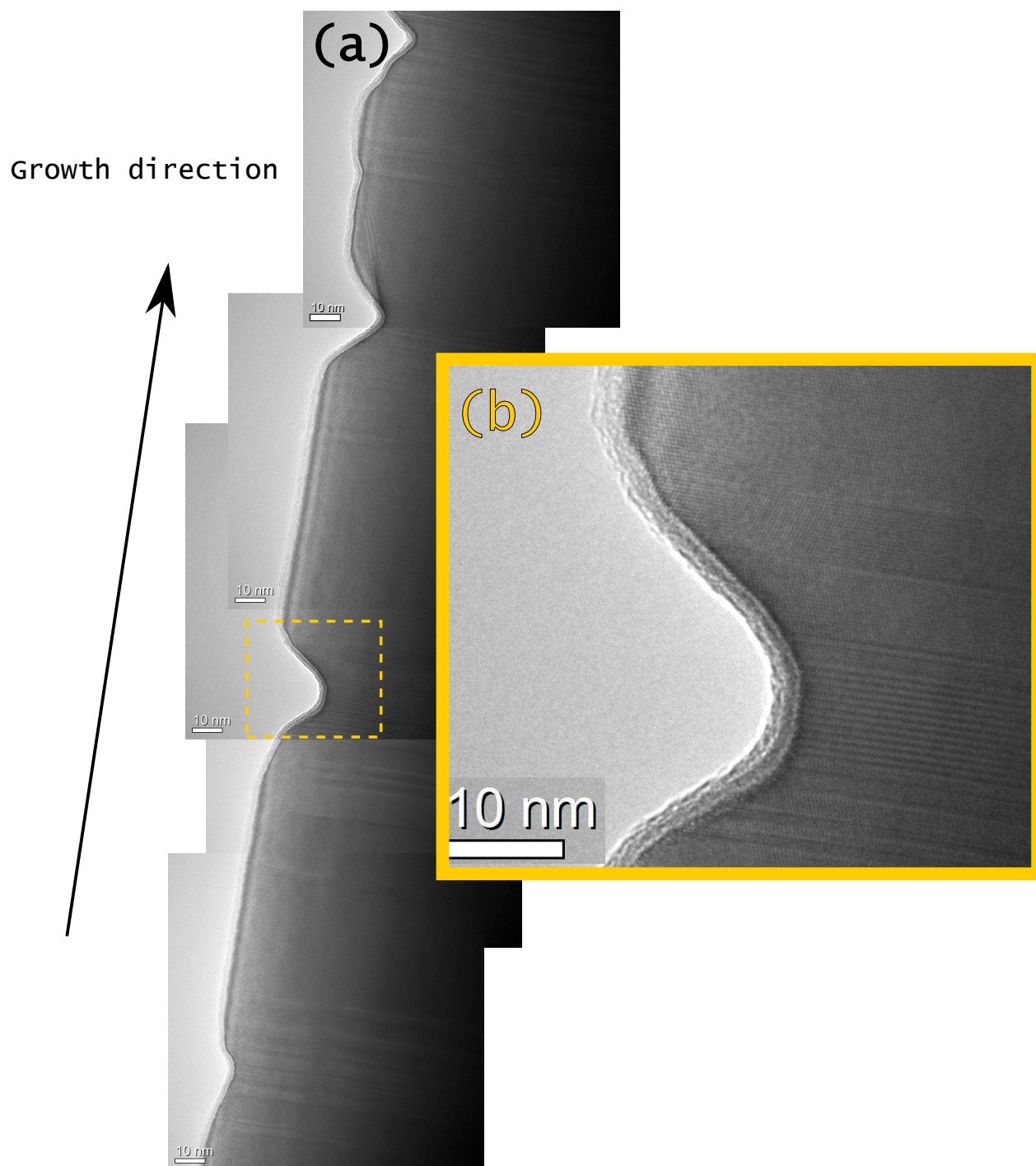
Figure 4.17: (a)HR-TEM lattice images from SL-5 of the sample B NW. (b) striped area in (a).
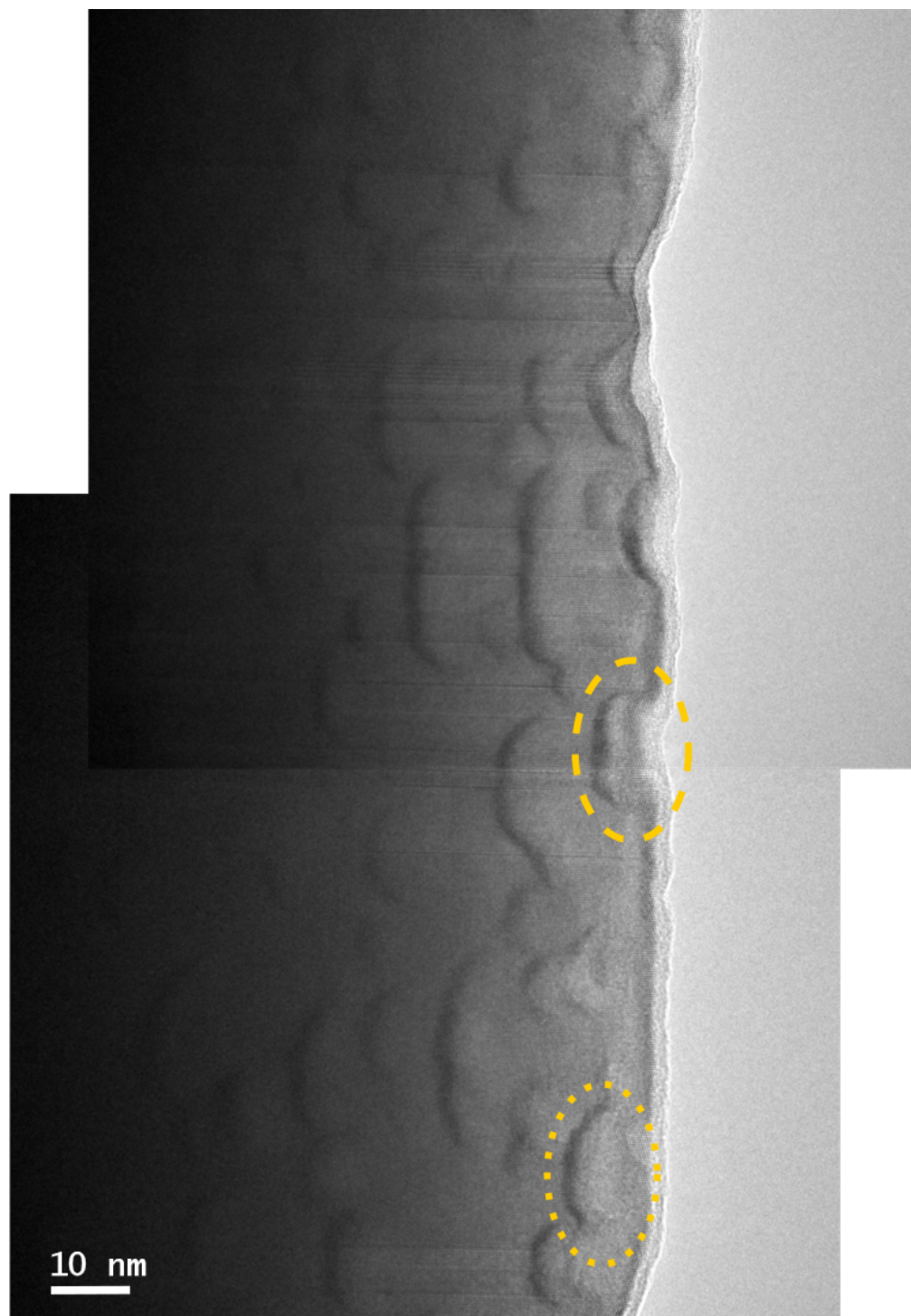
Figure 4.18: HR-TEM images of W1 and B1 from SL-4.

Chapter 5

Discussion

The results presented in Chapter 4 will be discussed in this chapter. The aim of this work has been to characterize and compare the cystal structure of four differently grown NWs, to see what the difference Sb concentration has resulted in for the phase structures of the NWs, and compare these findings to measurements of their optical properties that have been found in a study by PhD candidates Dingding Ren and Lyubomir Ahtapodov (Appendix E).

In this discussion, the following properties will be considered: general observations of the NW morphology, structure and end facets, the superlattice crystal phases and defect distribution, and som anomalies observed. The chapter will end with a discussion of the possible consiquences these aspects might have for laser application in light of the recent optical studies presented in Appendix E.

5.1   General observations

Sample A-D have been analyzed using conventional TEM methodes, and the findings about their general structure and morphology are interpretations of the data presented in Figures 4.4 to 4.7 and 4.15.

It is important to control the dimensions and morphology of a NW as these are factors that can influence the lasing effects and wavelengt [32, 28]. All the concidered NWs have comparable morphology, with varying length and thickness. The NWs are straight, but display a slight anti-tapered morphology, as can be seen qualitatively in in display (a) of Figures 4.4 to 4.7, and quan-

titativly from Table 4.1. This may be related to change in catalyst droplet size during growth. Sample A has ~ 18% increase in projected width towards the end of SL-6, while the increase in width for sample D is only ~ 8%. Thus the degree of anti-taperedness decline with increased Sb concentration. The thickness of the four NWs are, hence, different, where the average projected width increase with increased Sb concentration, with the exception of sample D which is thinner than sample B and C, but also the least anti-tapered. This is likely related to a difference in growth condition, and thus a dependence on Sb concentration. The length of SL-6 is generally shorter than SL-3-5, that have a similar length, in all measured NW structures (Figure 4.9). Since the NWs might not have been broken off at the same position during sample preparation, the lengths that have been compared between the samples are the SL-5 lengths. From Figures 4.10 and 4.11, samples C and D have the same SL-5 lengths, while the NWs with the lowest Sb flux has the longest. An increase in Sb flux during growth is known to increase the radial growth of self-catalyzed GaAsSb NWs[14]. Work by Ren et al. (2016) has reported a dependence in the droplet contact angle with the growth rate of a NW. Sb reduce the droplet contact angle, and leads to enhanced radial growth and a decrease in axial growth rate [40]. This can explain why sample C and D have shorter SL regions than the samples grown under a lower Sb flux as well as why the last SL in the structure (SL-6) is shorter. EDS studies by PhD candidate Julie S. Nilsen (Appendix D) confirm this, as Figure D.3 show a slight increase in the measured Sb% of SL-6 (of all samples) compared with the other SLs. As there is a build up of Sb content (to be further discussed), SL-6 can be expected to have a generally higher Sb. The higher amount of Sb from increased Sb flux and time during the GaAsSb insert growth seems to, not only increase the radial growth, and thus diameter of the NW, but also stabilize it, resulting in a less anti-tapered morphology (Table 4.1). This does, however not explain why sample D has a smaller thickness than sample B and C, and further investigation is needed to explain this. However, no further measurements were done on this matter, and it cannot be known for sure if the change in thickness is from a radial change during growth of the core NW, or if it is the cause of an uneavenly grown shell and/or cap.

To achieve a predictable laser structure with the desired lasing properties, a stable super-lattice structure is advantageous. As opposed to the target structure of the NW superlattices presented in Chapter 3, the sample NWs all display variations in both SL and spacer lengths

(of various degrees), and changes in average length of ZB segments and mixed phase segment. This change in superlattice structure can be seen from the plotted length measurements in Figures 4.9 and 4.10, where the NWs phase structure of the SL generally seem to stabilize around SL-3, with some variations towards the very tip ($\sim$ SL-6). This stabilization might be partly related to the diffusion length of Ga for the part of the NW growing close to the substrate surface. As the NW grows further away from the surface of the substrate, the diffusion effects from the surface will be reduced. The diffusion length from the substrate surface onto the NW can therefore explain why there is a stabilization of the superlattice growth around SL-3 [41].

SL lengths and spacer lengths values are, from Figures 4.9 and 4.10, most constant in regions 3-5 in the compared NWs (Appendix B). In addition this is an area that is well represented in HR images for most of the samples. Because of this stabilization tendency for the higher superlattices, SL-5 is chosen as region of analyzation and comparison for the properties of the four NWs. All DF and HR-TEM images were taken at [110] beam direction, to be able to destinguish the crystal phases (Figure 4.16).

5.1.1 End facets

The lasing threshold condition is directly correlated to the end facet reflectivity Equation (2.36). It is therefore important that the end facets are of high quality. Estimating the end facet reflectivities is not an easy task, and it will not be attempted in this text. However, from the results showing the shape and atomic structure of the NW end facets, it is possible to make a qualitative discussion about the end facets.

The tips of the four sample NWs (Figure 4.2(a)-(d)), have similar morphology. Estimations of the angles between the facets of the tip and the NW growth plane, suggest that the NW tips mainly consist of facets in the 110- and 112- planes. The photons reflected off these facets might then scatter off at an angle relative to the NW growth direction. This contributes to a less paralell photon beam, and may lead to photons being reflected and hitting the NW side surface and become absorbed or further reflected.

The bottom facets of samples A-C also show have similar shapes from the BF-TEM images, displayed in Figure 4.2(f)-(h). Sample D (Figure 4.2(e)) has a foot-shape that is not present in the other samples, but other than that they look very similar. Rough measurements of the bottom

Table 5.1: The angle between planes in a cubic unit cell in degrees.

hkl	111	112	110	120	100
111	0	19.47	35.26	39.23	54.74

end facets, suggest that they generally consist of a 111- plane. The large 111- plane facet makes the bottom more likely to act as a mirror reflecting the photons without angular deviations from the 111 direction. Another feature is encircled in the images of the NW bottoms (Figure 4.2(e)-(h)), showing a chipped edge on one side of all four samples in either the 110 or 100 type of plane. A suggested explination for this is that this NW edge has been molded by the edge of the substrate hole where they were grown out of, but this cannot be concluded without further investigation.

The optimal situatuion, for laser applications, are entirely smooth end facets in the 111-plane for direct reflection of photons along growth direction. Altough the cleaved planes of the end facets are not optimal, the planes analyzed appear to be atomically smooth, judging from the HR-TEM images (Figure 4.3(b)-(c)) of the end facets, which all are found to have tips consisting of ZB phase. The end facets tend to consist of defect-free surfaces smoothly cleaved along cubic atom planes. This will more likely contribute to the reflection of photons, rather than absorption, as would have been the case with a rough or dented end facet surface. However, the measured angles are based on BF-TEM images, which lose important information about the faceting, as this is only a 2D projection of a 3D object. SEM images of a sample C NW array, PhD candidate Dingding Ren, clearly show these different facets of the NW tips (Figure E.2(a))

5.1.2 DF-TEM resolution from HR-TEM images

DF-TEM is the main source of data on the NW phase structures in this work. It is therefore important to know the error of this technique to determine the size of crystal phase sections. From Figure 4.14(a), the green arrows (in inset) mark a region with two WZ sequences, followed by five atomplanes of ZB phase, then three WZ sequences, followed by another five atomplanes in ZB phase and two new WZ sequences. The same region is outlined with a green box in Figure 4.14(a)-(d). This symmetrical section contains short phase segments and many phase shifts covering a small area. The DF image (fig:HRvsDF(c)) does not resolve these quick phase

changes. From the inset in Figure 4.14(c) the section appears to be mainly WZ with some ZB that appears to be located in the middle of a WZ region. The total region is estimated to be 4.4 nm from Figure 4.14(d), while the HR image (Figure 4.14(a)), reveals that the region is 6.6 nm long.

By measuring and comparing DF-TEM phase regions with their HR-TEM counterparts, the DF image has been found to have a general deviance of ± 3.5 nm from the HR images. The tendency is that phase segments of 4 nm or longer get shorter in DF, while shorter segments get longer in DF. In the profile of the DF image (Figure 4.14(d)), the intensity curves have an overlap. This causes a widening of short phase segments, which corresponds with the measurements, while longer phase segments appear shorter because of the spread of SFs by the intensity curves.

However, a small defect cause a crease in an otherwise stable intensity caused by a larger homogeneous phase segment. A large WZ phase, only containing one single SF (orange box Figure 4.14(a)-(d)) is measured to be 31.29 nm from the profile of the DF(Figure 4.14(d)), while it is 32.75 nm from the profile of the HR image (Figure 4.14(b)). Even though the WZ region only contains one single ZB sequence, the DF-TEM profile is still able to "see" it. It does not appear yellow (as a ZB region) in the DF image, but as a decrease in the blue color (WZ) intensity at the location of defect in the WZ phase. From Figure 4.14(d) (pink), the dip in WZ intensity is very small, but it is clear from the profile that there is a small ZB sequence at this position. By looking at the DF image, one can see the presence of a defect at this position (peak in ZB intensity), even though information about the nature of the defect is not available from the DF image. In this way, even defects that are smaller than 3 nm can be resolved in DF if they are surrounded by larger pure phased segments on either side. This means that DF imaging can be used to detect the presence of phase changes and SFs, but with a size error estimate of ± 3.5 nm for length measurements.

For the purose of this work it is not nessecary, nor realistic, to use HR-TEM to analyse the NWs. As 20 HR-TEM images were required to map one of the smaller SLs with one spacer (Section 4.2.6), one would need at least 120 HR images to cover all six SLs with containing spacers. For four NWs this would add up to more than 500 HR images. In addition, HR images from end facets would be desirable to get a full mapping of the entire NWs, increasing the necessary image amount even further. In addition, only one edge of the NW is being mapped from

this amount (of NWs the size of those in this work). This is unrealistic work to be conducted manually. Considering the resolution of DF image (±3.5 nm), this technique is sufficient for the purpose of giving an overview and characterize the tendency in the four different NWs. It is, however of use to have HR-TEM lattice images to analyse specific features of the NWs and to look in detail at atom planes and defects in the crystal structure for comparison to the DF-TEM images. An alternative and more automatic way of structural data gathering (and analyzation) is in development, and will be adressed in Chapter 7.

5.2   Crystal phases and defect distribution

In this section, the NWs structure will be described by their the spacers and superlattices, as they were defined in Chapters 3 and 4. Because of the high defect concentration on sample A, and the unability to define and measure the components of the superlattice structure, this sample is excluded from some of the following quatative measurements and comparisons. It is important to locate the GaAsSb inserts of the superlattice structure in the NW to better predict possible effects the defects and phase changes may have on the lasing properties of the NW. From Figures 4.5 to 4.7(b)-(d), one superlattice consist of ten pure ZB phase segments, separated by, in total, nine mixed phase regions between two spacers. Two orientations of ZB phase (ZB-1 and ZB-2) were observed in all mapped SL structures (Respectively green and red in (d) of Figures 4.5 to 4.7). These generally appear equaly distributed (Figure 4.8), and does not show any tendency in when one ZB phase orientation is favoured to another. The two ZB orientations are thus concidered equal in the rest of this text, as no affect of these were found in the data. From the growth information in Chapter 3 these ZB segments fits to the growth description, as the ten GaAsSb inserts intended as well material for the SL structure. Sb is know to influence the crystal structure by adopting or stabilizing ZB phase when added to GaAs [14], and others have reported of GaAsSb inserts always having ZB phase[27], which support this claim. This leads to the conclusion that the defect-free ZB regions of the SLs are the positions for the GaAsSb inserts. These segments will therefore be refered to as the inserts or the wells futher in the text.

Compositional analysis of the NWs is needed to say for certain if the ZB segments really are the Sb inserts, as well as if there exist Sb in the mixed phase regions (intended GaAs from Figure 3.1). EDS measurement was performed on a sample D NW on the JEOL 2100. The results can be found in Appendix C. However, these data show relatively little detected Sb in all three measured areas displayed in Figure C.1, with just a small peak in Sb% of the targeted insert area. However, these EDS measurements were not taken under optimalcircumstances as the resolution of the 2100 microscope is not suited to undertake tasks of this scale and thickness. Thus, material around the desired area might been detected aswell, and nothing can be concluded. A more accurate measurement is needed to say anything for sure, but it is suggested that we can expect the ZB regions to be Sb richer than that of the mixed phase regions. Such sophisticated EDS measurements have been executed by PhD candidate Julie Stene Nilsen and can be found in Appendix D. These studies does, indeed, show that there are ten distinct peaks in Sb% in one SL (Figure D.3). When compared to the measured lengths of the defect-free ZB phase regions found in this work, they seem to agree, concluding that these regions do contain a higher Sb concentration than the mixed phase regions. However, these mixed phase regions also contains Sb, although at a less percentage than the ZB regions. This may suggest that the Sb need to reach a certain percentage for the ZB phase to develop. However, from the comparison of the l_W and l_B to the widths of the Sb% peak and bottom widths, this percentage threshold seem to change within one SL. Further analysis of the data might therefore be interesting to study if there exist such a threshold purely dependent on the Sb concentration, or if and when the dynamical change in droplet contact angle affects this threshold as it develops through growth. Rough measurements and calculations by the author suggest the latter, but further study is needed.

The difference between the four growth batches are the length of the superlattice, spacers, well segments and barrier segments, and the amount of defects and twinning in the spacer regions and barrier segments. From Figure 4.11 it is evident that the Sample D NW posessed the longes and most stable ZB phase (well) regions. Sample B show smaller insert regions, some even containing a TP (Figure 4.8), as compared to sample D. These TPs generally occur in the early SLs, and reduce in numbers towards SL-6, where no TPs were detected in well segments for any of the samples. The ZB regions become more unstable and shorter with decreased Sb flux of the (NWsFigure 4.10(a)), and the well areas of sample A are indistiguishable from the barrier

regions. As sample B and D are grown with the same Sb flux, the extra length of the sample D inserts is believed to come from the addition in GaAsSb growth time, so that a higher Sb flux during insert growth produce longer defect-free ZB phase regions. Sample C(Figure 4.11(C)), show stable and defect-free inserts, but with shorter length than those of sample D. It seems, therefore, that Sample C either was grown with higher Sb flux than sample B and D, or had a longer GaAsSb insert growth time than that of sample B, leading to an overall higher Sb concentration compared with sample B, but lower then sample D. This is in accordance with previous studies of GaAs/GaAsSb heterostructured NWs by Ren et al. (2016), where they concluded that Sb concentration over a certain threshold leads to defect-free ZB phase. Under this threshold, the Sb still favoured a ZB phase, but TPs and SFs was present [14]. To conclude, the increase in Sb concentration leads to longer defect-free ZB phase.

It is not only the ZB phase segments of the superlattices that changes in size with increased Sb of the sample NWs. From the images in Figure 4.11, and the plot in Figure 4.10(b), it is clear that the mixed phase regions separating the inserts become smaller with increased Sb concentration of the sample NWs. Mixed phase regions are stretches with phase layers of only a few nm, and are therefore rich in SFs and TPs. Sample A can from this be concidered to concist of only mixed phase. As Sb favours ZB phase, an explination for the change in size of the mixed phase region may be that the Sb concentration of the droplet remains above the earlier mentioned threshold to produce pure ZB phase. When the knudsen cell for Sb_2 closes, the Sb concentration will have hit a peak, and then drop as the NW continues to grow. The Sb concentration might then stay over the ZB phase threshold some time after the closing, before dipping below and create a mixed phase region. When comparing these results to the compositional results of PhD candidate Julie S. Nilsen, it appears that this, indeed, is the case (Appendix D). Figure D.3(a) show how sample A has low Sb concentration throughout the whole superlattice, with small variations between Sb% extremas and minimas, which have been observed to result in many stacking faults without stable crystal phase segments. In contrast, Figure D.3(d) has a much higher detected Sb%, with distinct maxima and minima at respectively the wells and barrier regions. The Ga droplet size acts in determining the phase structure of the NW. For a catalyst droplet with a small contact angle, WZ phase is the most energetically favourable phase, while a ZB phase is favourable for larger catalyst droplet sizes [27, 40]. When it is not obvious

which phase that is the most favoured, the phases become unstable and a mixed phase region occurs. Sb reduces the Ga catalyst droplet contact angle [27], but the compositional influence of Sb concentration dominates the contact angle criteria, and produces a ZB phase inspite of that [14]. This suggests a transition to WZ phase after the insert, as the droplet contact angle has been reduced, and the Sb concentration decrease. If the Sb concentration gets low enough, WZ segments will be produced. From this we can conclude that the mixed phase regions separating the pure ZB phase regions decrease in size as the peak of Sb concentration during insert growth increase. NWs show less mixed phase and SFs with increased Sb concentration.

From the above statement, it may seem that the increase in Sb concentration would produce less WZ phase. However, a third difference in crystal phase tendencies of the samples is that there is more pure WZ phase in the NW samples with higher Sb concentration. This is depicted in Table 4.2, where the percentage of WZ phase in spacer-4 and -5 presented. Here, the two spacers in sample D comprise of 70% WZ phase concentration, compared to 57% for sample B. This can be explained by the same reasoning as for why the mixed phase regions decrease. The Sb reduces the droplet contact angle which makes the WZ phase more favorable once the Sb concentration drops below a critical value. It is likely that there will be less mixed region before the phase settles at a more stable WZ phase in a case of high Sb flux. A NW with inserts grown under lower Sb flux, the contact angle might not be as reduced by the growth of the GaAsSb insert as is the case with a high Sb flux. From this, it would be less obvious which crystal phase that is favourable, and result in a longer mixed phase region with shorter and less stable WZ phase regions. This explains why we see more stable phase segments of WZ in the spacers of sample D (and sample C) as opposed to the samples grown under a lower Sb flux. It can thus be concluded that the WZ concentration increase with Sb concentration.

The growth parameters of sample C are unknown, but it is assumed to be somewhere in between sample B and sample D in Sb concentration. This assumption is based on the measured lengths of the various crystal phases and components of the SL structure (Figures 4.9 to 4.11). As already discussed, the crystal phases of the SL structure stabilize with the increase of Sb content. Sample C consistently show results in phase measurements between those of sample B and sample D. It is thus believed to have been grown under a higher Sb flux and/or a longer GaAsSb growth time than sample B, but not exceeding the combined Sb content of sample D. This hy-

pothesis is further strengthened by the EDS measurements of PhD candidate Nilsen (Appendix D) where Figure D.3 show that the Sb% of sample C contains concentration peaks of values between those of sample B and D.
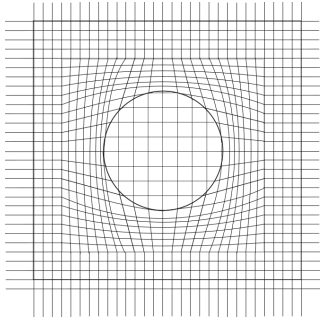
5.3 Anomalies

Figure 5.1: Illustration of atom matrix with a deposit of higher lattice parameter.

The bottom region of the NWs from samples B-D show some circular shapes, as presented in Figure 4.15. These intesity contrast start off as small oval-shapes, that grow in size along the axial direction of the NW. Since the shapes appear to be centered in the middle of the NWs where thickness is high (~ 400 nm), the images had to be oversatuated to reveal the buble shapes. The features only appear within the defect-free ZB phase segments, and not in the mixed or WZ phase regions. From this, these features are believed to be strain-field contrasts from change in crystal structure. An explination for the strain fringes is that they occur where the Sb inserts are.

The difference in lattice parameter of GaAsSb compared to that of GaAs (Figure 2.13) creates strain in the insert region [23]. The strain created by a circular insert of higher lattice parameter than it's surroundings is illustrated in Figure 5.1. The strain contrasts observed in the analysed NWs increase in size in radial NW direction (into a more oval shape) as the NW grows. During growth the droplet gets larger, and thus the Sb insert gets larger futher up the NW. This part of the NW is close to the substrate surface, leading to radial growth from Ga diffusion from the substrate, embedding the anti-tapered Sb inserts. This, and the fact that these quantum dot-like features are only observed in SL-1 and within the defect-free ZB phase segments, supports the statement that the defect-free ZB phase segments are the Sb insert regions of the superlattices. However, strain-field contrasts are hard to characterize in segments with lots of defects. This can explain why they were not observed in sample D NWs. Yet, it might be that the strain features are only visible, and not excusively present, in the pure phased regions, but this would then be a different phenomena and would need more investigation to explain.

From the HR-TEM lattice images some local changes in the NW thickness was observed in certain areas. An example of this from sample-B is displayed in Figure 4.17(c). The NW has a distinct decrease in diameter in the segments of WZ phase. As the phase changes from a pure Zb phase, via a mixed phase segment and transist into WZ phase, there is a gradual decrease in NW diameter. The thickness then increase as the WZ phase transist to a ZB phase, and stabalize at more or less the same diameter that it had before the WZ segment. This tendency in tchickness change occur (of different degrees) in most of the WZ segments of the NWs, and are, thus, more prominent in sample B than in sample-D. These local abrupt changes in NW width seem directly linked to the phase change between ZB and WZ phase. This can be explained by an increased radial growth with added Sb. This has been reported for work showing that, while both show a stronger adsorbtion on a (110) surface for the Ga adatoms, Sb enhances a higher surface diffusion than As [14]. The NW with lower insert growth time has has a higher radial growth difference for well and barrier growth, as compared with a NW with longer GaAsSb growth time, which locally show a more stable thickness.

The HR-TEM images of the sample C NW revealed features that were not found in the NWs from other samples. Figure 4.18 shows an HR-TEM lattice image presenting these features, marked with dotted circles. There seems to be no correlation with the crystal structure in the area of the features and the occurance of the features, as well as they appear to be present consistently throughout the whole HR-mapped area of this NW. The features appears to be intensity contrasts from crater-like features in the NW surface. Hence, the sample C has holes and dents in the surface of the NW. Since this defect appears on all the NWs of the sample that has been observed, something might have faultered the making of this NW batch. One theory is that the adding of the protective GaAs protective cap covering the shell was unsuccessful, or did not cover the entire NW surface. Absence of, or unsufficient capping leaves the AlGaAs shell exposed to oxidation. This may explain the holes on the surface of the NW. Sample C is therefore believed to have an insufficient cap layer, and thus show surface damage caused by oxidation of the AlGaAs shell. This may hav a negative effect on the lasing properties of these NW, that will be discussed further in the following section.

5.4   Consequences for laser application

From the growth procedure presented in Chapter 3, each superlattice was grown with 10 segments where Sb was introduced, intended to create a superlattice of GaAsSb quantum wells with GaAs barrier segments in between (Figure 3.1), because of the difference in BG energy of the two semiconductors (Figure 2.13). As previously discussed, the Sb inserts appears to be located where the defect-free ZB phase segments are. Thus, for the NW characterized in this work, these pure ZB segments are the well material, and the mixed phase regions separating them acts as the barrier material.

The variation in phas dimentions, particularly the well size, found in the different NW samples suggest that they will emitt light of different wavelengths, where the Sample D (with longest wells) light would have a red shift compared with the other samples. This is also what was found when PhD candidated Dingding Ren and Luybomir Ahtapodov conducted optical measurements of the sample NWs (Appendix E). Figure E.1 show that all the NWs emitted light when optically pumped above their respective lasing thresholds, with sample A emitting the shortest and sample D the longest wavelength. This is in accordance with what was expected from the structual analyses.

Previously it was concluded that the sample C NWs have defected shells. The question then arised as if these NW would be able to achieve lasing. Since the lasing in the NW happens in the core (FP cavity), and along the growth direction, this might not affect the lasing properties conciderably. There is even a possibility that it favors a paralell beam, as photons deviating from the growth direction would more likely be absorbed than reflected by the uneaven NW surface. However, the AlGaAs shell shell has the intended purpose of preventing trapped surface states along the NW [15]. Oxidation of the shell enables trapped surface states in the exposed core regions. This can affect the lasing properties of the sample C NWs negatively, because of a loss of mobile charges, and thus a decrease in efficiency. At a low pumping power, the sample C NW emitted a slightly longer wavelength than sample B, as expected since sample C show longer wells and generally more stable phase structures. However, when increasing the pumping power, sample C has a stronger blue shift than that of sample B (Figure E.1). By combining these findings it therefore seems like the surface damage observed on sample C (Fig-

ure 4.18), indeed, has a negative impact on the lasing performance, which becomes evident at higher pumping power. This states the importance of a sufficiently covering protective cap for the NW lasing efficiency.

The mixed regions comprise of a lot of defects, TPs, phase shifts and WZ regions with SFs. As some phases are very narrow, they might give rise to confinement effects (trapping electrons and holes) causing the BG energy of these regions to rise. The well material sections need to have a certain length to avoid confinement effects, which would be unfortunate for lasing effects (a confined electron would need more energy to recombine) [16]. Considering the sample A NW one would then think that the superlattice contains so many defects that there will be a loss of mobile charges. To achieve lasing with this type of NW one will the have to pump harder. If lasing, the resulting wavelength would then be blue shifted relative the emitted light of the three other NWs with welldefined defect-free stretches of well material. The need for extra pumping would, however, make the NW less efficient energy wise for laser applications. This is confirmed in Figure E.1, where sample A emitts a relatively short wavelength compared to the other samples. As assumed from the structural analyses, this sample show the lowest efficiency of the four samples, however, it does show lasing. This show that the well-defined well and barrier area is less crucial for achieving lasing than was assumed before this study.

From the findings of this work, and in light of the studies presented in Appendices D and E, it can be concluded that sample D show the NW SL structure most closely related to the target structure (Figure 3.1), and is most prefered for laser application. From this, an adjusted structure of the NW is presented in Figure 5.2 based on sample D to summarize the crystal phase structure found to be most efficient for lasing application of the samples studied in this work.
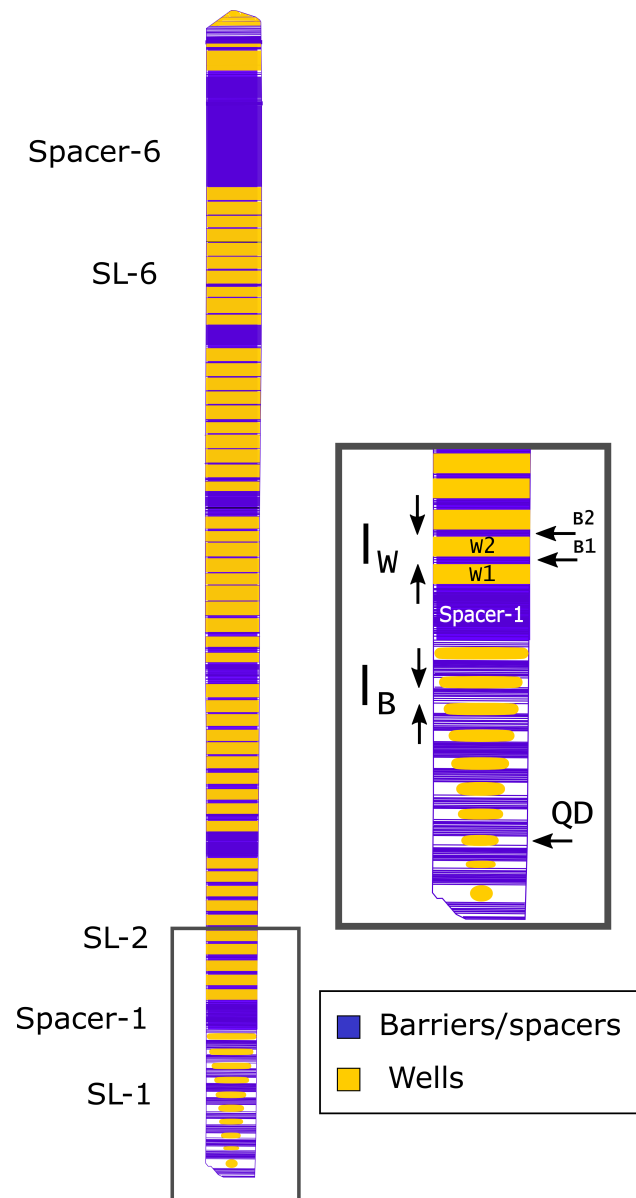
Figure 5.2: Schematics of adjusted NW superlattice structure based on findings on the sample D NW

Chapter 6

Conclusion

In this study, structual characterization of four self-catalyzed GaAs NW, grown with six GaAsSb/GaAs SLs at different Sb fluxes and/or growth time of GaAsSb inserts, has been perfomed by the use of conventional TEM (BF, DF, SAED and HR-TEM). The NWs were around 10 μm long and 400 nm thick. Quantization of crystal phase distribution were mainly based on DF images. By comparing the DF images to HR-TEM images it was found that the DF phase technique have a resolution of ~ 3.5 nm. All samples have similar morphology, but vary slightly in length and thickness, with a decrease in length and increase in thickness with increasing Sb flux.

When comparing the grown NWs with the target structure for the SLs, the crystal phases were found to be highly dependend on the Sb content. Sample A was excluded from the quantitative phase measurements because of it's high (> 2 SFs per 10 nm NW length on average) defect concentration caused by low Sb content. Samples B-D showed six SLs, each containing 10 ZB phase (well) segments, of equal but randomly occurances of ZB_1 and ZB_2 phase, separated by 9 mixed phase (barrier) segments of various sizes (Figure 4.10). Generally, the superlattice structures stabilized around SL-3, with the following SL showing relatively similar well sizes and crystal phases. Thus SL-5 was compared between the sample SL structures as this was a well-represented region in HR-TEM for most samples. An increase in Sb flux and GaAsSb growth time showed a stabilizing effect on all crystal phases within the NW, both for the ZB phases at the inserts, and for the WZ phase for GaAs barrier segments. Increase in Sb concentration is, thus, found to give longer defect-free ZB segments, smaller mixed phase regions and SFs, and a higher WZ concentration in grown NWs.

Other features of the NWs were also studied, like the NW tips. They were found to have similar morphology in all four samples and atomically smooth surface planes in distinct directions (mainly 110 and 112). Quantum dot-like features were observed as circular strain contrats in SL-1 of the NWs and increased in width towards SL-2, seemingly caused by the GaAsSb inserts. This indicates whitnessing of an increasing catalyst droplet size, anti-tapered NW morphology and supporting the hypothesis of the Sb inserts being located at the ZB phase segments. A variation in local thickness of the NWs were found, and explained by the higher radial growth of Sb, as the increase in NW diameter occoured regularly at the ZB phase segments, to then reduce at WZ segments. In addition, sample C were found to have surface defects caused by oxidation of the AlGaAs shell intended to prevent trapped surface states. This is believed to be the cause of the blue-shift of this sample's emitted wavenlength, as harder optical pumping is needed to achieve lasing. A sufficient capping of the NW is therefore important for the lasing efficiency.

All of the studied samples depicted lasing when optically pumped, with the tendency of longer emitted wavelength for higher Sb concentration, seemingly caused by the decrease in mixed phase regions and stabilization of the crystal phases. This give insight for the continuation of developing semiconductor NW lasers. Further studies are needed to find the optimal growth condition for NW based lasers, as well as work to achieve electrically pumped lasers for better implementation into current technological devices. Also, the experimental work and data gathering for this study would greatly benefit from a more automatical method of NW mapping, as the method persented in this text is very time consuming and thus limited to poor statistical representation of the data.

Chapter 7

Future work

Growth and laser optimization

From the adjusted model of the NWs given in Chapter 5 it is clear that the NWs presented in this work are not ideal compared to the target structure given in Chapter 3. Since the first couple of superlattices showed phase instabilities, as compared to the SL-3 and up, a possible solution can be to increase the length of the stem, i.e. the length before SL-1, that is grown before the first superlattice structure. If the cause of the instabilities and variations compares to the other SLs in these first superlattices are due to a varying diffusion of Ga from the substrate surface, then a longer stem might help stabilizing. TEM characterization on several NWs can then be done to see if the superlattice structures have improved in uniformity.

As found in this study, the NWs should be grown with a certain Sb concentration to achieve stable and defect-free ZB phases. A longer growth time for the well and barrier step might result in a more stable growth. For the lasing, a larger difference between the well and barrier energy could be beneficial. Thus, if the stacking fault density is reduced by a higher Sb concentration then it follows that the well material has to be Sb richer. This could require a longer well growth time. Further experimentation regarding sufficient Sb flux or GaAsSb growth time, followed by conventional TEM and EDS, is therefore needed to achieve an optimal superlattice structure. To optimize lasing, the growth, TEM and optical studies should be well integrated.

The next big step would be to achieve electrical pumping of NW arrays. For this, the substrate is required to be one of the electrodes. A Bragg grating should be integrated in the substrate as a reflector, and a transparent top contact can be placed on the top. Such design features will require advanced device fabrication.

Improving quantitative crystal phase mapping

All crystal phase characterization, the retrieving and interpretation of DPs, DF-TEM and HR-TEM images, was done manually in this work. This has been an extremely time-consuming process, producing complete and detailed data on only four entire NWs. Both amount of NWs analyzed, as well as objective selection of probed NW is desired. Improvements, towards automatization, of the collecting and interpreting of data would therefore be highly advantageous. This would open for the possibility to gain more statistics in similar studies. An alternative to an all-manual method is already under development and is based on Scanning Precession Electron Diffraction (SPED). This technique can offer semi-automatic phase mapping of whole NWs. In SPED, every pixel of the image of a NW is a precessed electron diffraction pattern. Thus, the data consist of a stack of many DPs. This offers a variation of advantages, like the possibility to achieve kinematic-like patterns, especially from the thinner NW edges and thereby making phase identification easier(Figure 2.5), since every pixel get DPs from different beam angles and only a few angles have strong dynamic features such as the forbidden 0001 reflection for WZ. From this one can by take advantage of the kinematically forbidden reflections and use computer programs (either based on matching to calculated patterns or classification into groups using machine learning) to determine crystal structures and orientation automatically. Another advantage is that the rotation of the beam leads to less diffraction contrast effects, like bending contrasts, in the images, in addition to the impressive DP concentration such an automatization can provide.

The DPs gathered can further be used in a computer program to generate virtual DF images by the insertion of a virtual aperture as shown in Figure F.1. This way, the data will be stored for the user to come back and gather new information from the collected data, instead of having to start over by mapping a new entire NW manually on the microscope. This can both be extremely time saving and enable further exploitation of collected data sets. This is only one, semi-automatic, method of analyzing SPED data sets. Two other, and less manual alternatives are template matching and machine learning (more elaborated in Appendix F), where especially machine learning show great potential for the future of NW mapping. However, SPED currently requires a lot of memory space and computer power. SPED mapping of one single superlattice costs about 1.6 GB of computer memory (i.e. the file size), as it contains around 9000 DPs.

Processing them can be computationally demanding and only a fraction of this set was analyzed further by matching to calculated structure s or machine learning. To scan and map a whole NW such as the ones studied in this work, the data would take more than, at least, 6 GB of memory. Computer power is therefore currently an issue, but it might become practical in the future.

Bibliography

[1] E. D. Minot, F. Kelkensberg, M. van Kouwen, J. A. van Dam, L. P. Kouwenhoven, V. Zwiller, M. T. Borgström, O. Wunnicke, M. A. Verheijen, and E. P. A. M. Bakkers. Single quantum dot nanowire LEDs. *Nano Letters*, 7(2):367–371, 2007.

[2] J. Wallentin, N. Anttu, D. Asoli, M. Huffman, I. Aberg, M. H. Magnusson, G. Siefer, P. Fuss-Kailuweit, F. Dimroth, B. Witzigmann, H. Q. Xu, L. Samuelson, K. Deppert, and M. T. Borgstrom. InP nanowire array solar cells achieving 13.8% efficiency by exceeding the ray optics limit. *Science*, 339(6123):1057–1060, 2013.

[3] M. Yao, N. Huang, S. Cong, C.-Y. Chi, M. A. Seyedi, Y.-T. Lin, Y. Cao, M. L. Povinelli, P. D. Dapkus, and C. Zhou. GaAs nanowire array solar cells with axial p–i–n junctions. *Nano Letters*, 14(6):3293–3303, 2014.

[4] J.-P. Colinge, C.-W. Lee, A. Afzalian, N. D. Akhavan, R. Yan, I. Ferain, P. Razavi, B. O'Neill, A. Blake, M. White, A.-M. Kelleher, B. McCarthy, and R. Murphy. Nanowire transistors without junctions. *Nature Nanotechnology*, 5(3):225–229, 2010.

[5] T. H. Maiman. Stimulated optical radiation in ruby. *Nature*, 187(4736):493–494, 1960.

[6] A.V. Maslov and C.Z. Ning. Modal gain in a semiconductor nanowire laser with anisotropic bandstructure. *IEEE Journal of Quantum Electronics*, 40(10):1389–1397, 2004.

[7] S. Hirano, N. Takeuchi, S. Shimada, K. Masuya, K. Ibe, H. Tsunakawa, and M. Kuwabara. Room-temperature nanowire ultraviolet lasers: An aqueous pathway for zinc oxide nanowires with low defect density. *Journal of Applied Physics*, 98(9):094305, 2005.

[8] P. Yang, R. Yan, and M. Fardy. Semiconductor nanowire: What's next? *Nano Letters*, 10(5):1529–1536, 2010.

[9] Y. Zhang, J. Wu, M. Aagesen, and H. Liu. III–V nanowires and nanowire optoelectronic devices. *Journal of Physics D: Applied Physics*, 48(46):463001, 2015.

[10] F. Qian, Y. Li, S. Gradečak, H.-G. Park, Y. Dong, Y. Ding, Z. L. Wang, and C. M. Lieber. Multi-quantum-well nanowire heterostructures for wavelength-controlled lasers. *Nature Materials*, 7(9):701–706, 2008.

[11] G. Koblmüller, B. Mayer, T. Stettner, G. Abstreiter, and J. J Finley. GaAs–AlGaAs core–shell nanowire lasers on silicon: invited review. *Semiconductor Science and Technology*, 32(5):053001, 2017.

[12] X. Yan, W. Wei, F. Tang, X. Wang, L. Li, X. Zhang, and X. Ren. Low-threshold room-temperature AlGaAs/GaAs nanowire/single-quantum-well heterostructure laser. *Applied Physics Letters*, 110(6):061104, 2017.

[13] D. Ren, L. Ahtapodov, J. S. Nilsen, J. Yang, A. Gustafsson, J. Huh, D.-C. Kim, G. Conibeer, A. T. J. van Helvoort, B.-O. Fimland, and H. Weman. High-Q factor, wavelength-tunable, room-temperature lasing from GaAsSb-based nanowire superlattices. [Unpublished work, in preparation, part of PhD thesis D. Ren].

[14] D. Ren, D. L. Dheeraj, C. Jin, J. S. Nilsen, J. Huh, J. F. Reinertsen, A. M. Munshi, A. Gustafsson, A. T. J. van Helvoort, H. Weman, and B.-O. Fimland. New Insights into the Origins of Sb-Induced Effects on Self-Catalyzed GaAsSb Nanowire Arrays. *Nano Letters*, 16(2):1201–1209, 2016.

[15] H. J. Joyce, Q. Gao, H. H. Tan, C. Jagadish, Y. Kim, J. Zou, L. M. Smith, H. E. Jackson, J. M. Yarrison-Rice, P. Parkinson, and M. B. Johnston. III–V semiconductor nanowires for opto-electronic device applications. *Progress in Quantum Electronics*, 35(2-3):23–75, 2011.

[16] D. Vvedensky, E. Johnson, M. Blencowe, A. MacKinnon, J. Nelson, C. Phillips, A. Khan, P. Stavridou, G. Parry, T. Thornton, and J. Harris. *Low-Dimensional Semiconductor Structures*. Cambridge University Press, December 2008.

[17] C. Kittel. *Introduction to Solid State Physics.* University of California, CA, 8th edition, Wiley, 2005.

[18] E. J. Samuelsen. Material physics lecture notes; structure, diffraction, imaging and spectroscopy. Department of Physics, NTNU, 2006.

[19] J. W. Edington. *Monographs in Practical Electron Microscopy in Materials Science.* Macmillan, Department of Metallurgy and Material Science, University of Cambridge, Cambridge, England, 1976.

[20] Y. A. D. et al. Rojas. Structural defects in cubic semiconductors characterized by aberration-corrected scanning transmission electron microscopy. *Ultramicroscopy*, 176:11–22, 2017.

[21] P. C. Hemmer. *Faste stoffers fysikk.* Tapir, 2 edition, 1987.

[22] L. S. Ramsdell. Studies on silicon carbide. 32:64–82, 1947.

[23] D. B. Williams and C. B. Carter. *The Transmission Electron Microscope.* Springer US, Boston, MA, 2009.

[24] JEOL. *JEM-2100: Electron microscope, TEM user manual*, 2012.

[25] H. Kauko, C. L. Zheng, Y. Zhu, S. Glanvill, C. Dwyer, A. M. Munshi, B. O. Fimland, A. T. J. van Helvoort, and J. Etheridge. Compositional analysis of GaAs/AlGaAs heterostructures using quantitative scanning transmission electron microscopy. *Applied Physics Letters*, 103(23):232111, 2013.

[26] R. S. Wagner and W. C. Ellis. Vapor-liquid-solid mechanism of single crystal growth. *Applied Physics Letters*, 4(5):89–90, 1964.

[27] A. M. Munshi, D. L. Dheeraj, J. Todorovic, A. T.J. van Helvoort, H. Weman, and B.-O. Fimland. Crystal phase engineering in self-catalyzed GaAs and GaAs/GaAsSb nanowires grown on si(111). *Journal of Crystal Growth*, 372:163–169, 2013.

[28] S. W. Eaton, A. Fu, A. B. Wong, C.-Z. Ning, and P. Yang. Semiconductor nanowire lasers. *Nature Reviews Materials*, 1(6):16028, 2016.

[29] D. Kleppner. Rereading Einstein on radiation. *Physics Today*, 58(2):30–33, 2005.

[30] J. Hecht. Laser: light amplification by stimulated emission of radiation., 2015.

[31] Nakamura, S. and Senoh, M. and Nagahama, S. and Iwasa, N. and Yamada, T. and Matsushita, T. and Kiyoku, H. and Sugimoto, Y. InGaN multi-quantum-well-structure laser diodes with cleaved mirror cavity facets. *Japanese Journal of Applied Physics*, 35(2B):L217–L220, 1996.

[32] C. Couteau, A. Larrue, C. Wilhelm, and C. Soci. Nanowire lasers. *Nanophotonics*, 4(1):90–107, 2015.

[33] JC Johnson, HQ Yan, RD Schaller, LH Haber, RJ Saykally, and PD Yang. Single nanowire lasers. *Journal of Physical Chemistry B*, 105(46):11387–11390, 2001.

[34] A. M. Munshi. *Epitaxial Growth of Self-Catalyzed GaAs Nanowire by Molecular Beam Epitaxy*. PhD thesis, NTNU, 2014.

[35] D. Ren, J. Huh, Y. Chen, J. S. Nilsen, D. L. Dheeraj, A. T. J. van Helvoort, H. Weman, and B.-O. Fimland. High-yield heterostructured GaAsSb/GaAs nanowire arrays on silicon for optoelectronic applications. [Unpublished work, in preparation, part of PhD thesis D.Ren].

[36] Inc. Gatan. Digital micrograph (2.32.888.0), http://www.gatan.com/, 1996-2015.

[37] B. Harrington et al. Inkscape (0.91), http://www.inkscape.org/, 2004-2005.

[38] H. L. Zhou, T. B. Hoang, D. L. Dheeraj, A. T. J. van Helvoort, L. Liu, J. C. Harmand, B. O. Fimland, and H. Weman. Wurtzite GaAs/AlGaAs core–shell nanowires grown by molecular beam epitaxy. *Nanotechnology*, 20(41):415701, 2009.

[39] Daniel Jacobsson, Fangfang Yang, Karla Hillerich, Filip Lenrick, Sebastian Lehmann, Dominik Kriegner, Julian Stangl, L. Reine Wallenberg, Kimberly A. Dick, and Jonas Johansson. Phase transformation in radially merged wurtzite GaAs nanowires. *Crystal Growth & Design*, 15(10):4795–4803, 2015.

[40] D. Ren, J. Huh, D. L. Dheeraj, H. Weman, and B.-O. Fimland. Influence of pitch on the morphology and luminescence properties of self-catalyzed GaAsSb nanowire arrays. *Applied Physics Letters*, 109(24):243102, 2016.

[41] L. T. T. Giang, C. Bougerol, H. Mariette, and R. Songmuang. Intrinsic limits governing MBE growth of Ga-assisted GaAs nanowires on si(111). *Journal of Crystal Growth*, 364:118–122, 2013.

Appendix A

Nanowire structural data

Measurements of phase structure of the NWs studied in this work are given in Tables A.1 to A.6

Table A.1: Measured lengths of SL and spacers of sample B, and average l_W and l_B from DF images.

SL-n	l_{SL} (nm)	$l_{spacer-n}$ (nm)	Average l_W (nm)	Average l_B (nm)
SL-1	1143	312	61	59
SL-2	1249	390	81	49
SL-3	1160	285	68	53
SL-4	1244	263	67	64
SL-5	1206	247	62	65
SL-6	1054	242	57	54

Table A.2: Sample B well measurements from DF images. "*" marks well containing single TP.

SL-n	l_{well-1} (nm)	l_{well-2} (nm)	l_{well-3} (nm)	l_{well-4} (nm)	l_{well-5} (nm)	l_{well-6} (nm)	l_{well-7} (nm)	l_{well-8} (nm)	l_{well-9} (nm)	$l_{well-10}$ (nm)
SL-1	60	59	64	66	68*	60	72	55	59	51
SL-2	92	89*	85	67	88	87	77	82*	63	76*
SL-3	74	59	63	71	57	64	71*	71	85	64
SL-4	60*	73	71	71	68	53*	68	86*	62	57
SL-5	46*	43	65*	74	73*	52	70	77	53	71*
SL-6	26*	57	61	64	49	61	63	51	75	65

Table A.3: Measured lengths of SL and spacers of sample C, and average l_W and l_B from DF images.

SL-n	l_{SL} (nm)	$l_{spacer-n}$ (nm)	Average l_W (nm)	Average l_B (nm)
SL-1	1292	193	83	51
SL-2	1477	305	100	53
SL-3	1384	271	87	58
SL-4	1291	241	72	64
SL-5	1100	168	73	41
SL-6	907	229	75	18

Table A.4: Sample C well measurements from DF images. "*" marks well containing single TP.

SL-n	l_{well-1} (nm)	l_{well-2} (nm)	l_{well-3} (nm)	l_{well-4} (nm)	l_{well-5} (nm)	l_{well-6} (nm)	l_{well-7} (nm)	l_{well-8} (nm)	l_{well-9} (nm)	$l_{well-10}$ (nm)
SL-1	60	120	95*	64	70	76	60	157	88	61
SL-2	131*	93	95	100	105	90	93	95	90	108
SL-3	80	92	88	77	82	82	77	92	96	100*
SL-4	58	76	77	81	71	68	86	73	72	55
SL-5	70	57	72	70	75	77	70	81	72	85
SL-6	51	80	75	78	58	75	88	77	75	90

Table A.5: Measured lengths of SL and spacers of sample D, and average l_W and l_B from DF images.

SL-n	l_{SL} (nm)	$l_{spacer-n}$ (nm)	Average l_W (nm)	Average l_B (nm)
SL-1	1046	274	45	67
SL-2	1083	222	69	43
SL-3	1100	208	76	37
SL-4	1118	206	86	28
SL-5	1108	186	85	28
SL-6	1070	NA	93	16

Table A.6: Sample D well measurements from DF images. "*" marks well containing single TP, and $\diamond$ marks combined wells with no mixed region in between.

SL-n	$l_{\text{well}-1}$ (nm)	$l_{\text{well}-2}$ (nm)	$l_{\text{well}-3}$ (nm)	$l_{\text{well}-4}$ (nm)	$l_{\text{well}-5}$ (nm)	$l_{\text{well}-6}$ (nm)	$l_{\text{well}-7}$ (nm)	$l_{\text{well}-8}$ (nm)	$l_{\text{well}-9}$ (nm)	$l_{\text{well}-10}$ (nm)
SL-1	73	31	48*	39	41	39	42	40	44	50
SL-2	69	65	62	73	56	77	75	73	72	71
SL-3	71	80	75	67	89	84	76	70	79	73
SL-4	60	80	88	91	104	84	86	95	88	88
SL-5	61	99	96	89	90	87	86	76	77	99
SL-6	80	96	83	88	99	204$\diamond$	$\diamond$	92	93	94

Appendix B

HR-TEM images

The HR-TEM images of sample A-C are presented in Figures B.1 to B.3.
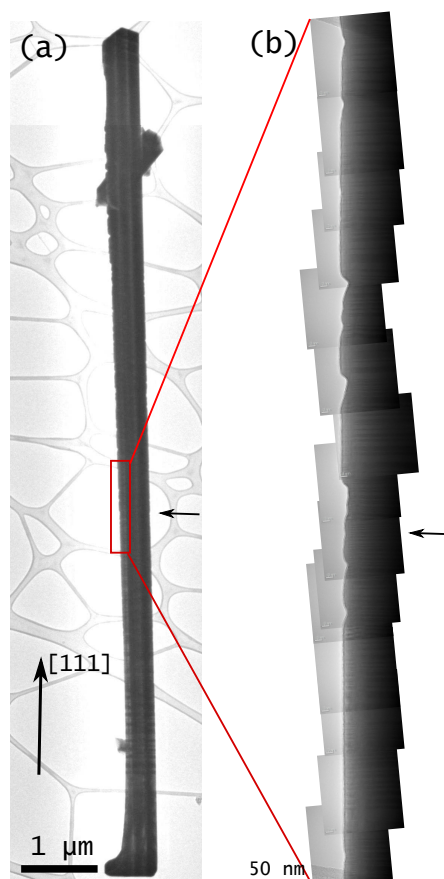
Figure B.1: (a) BF-TEM of Sample A. (b)-(d) compilation of 14 HR-TEM images from area marked with red square in (a). (b) estimated W3 (indicated with arrow).
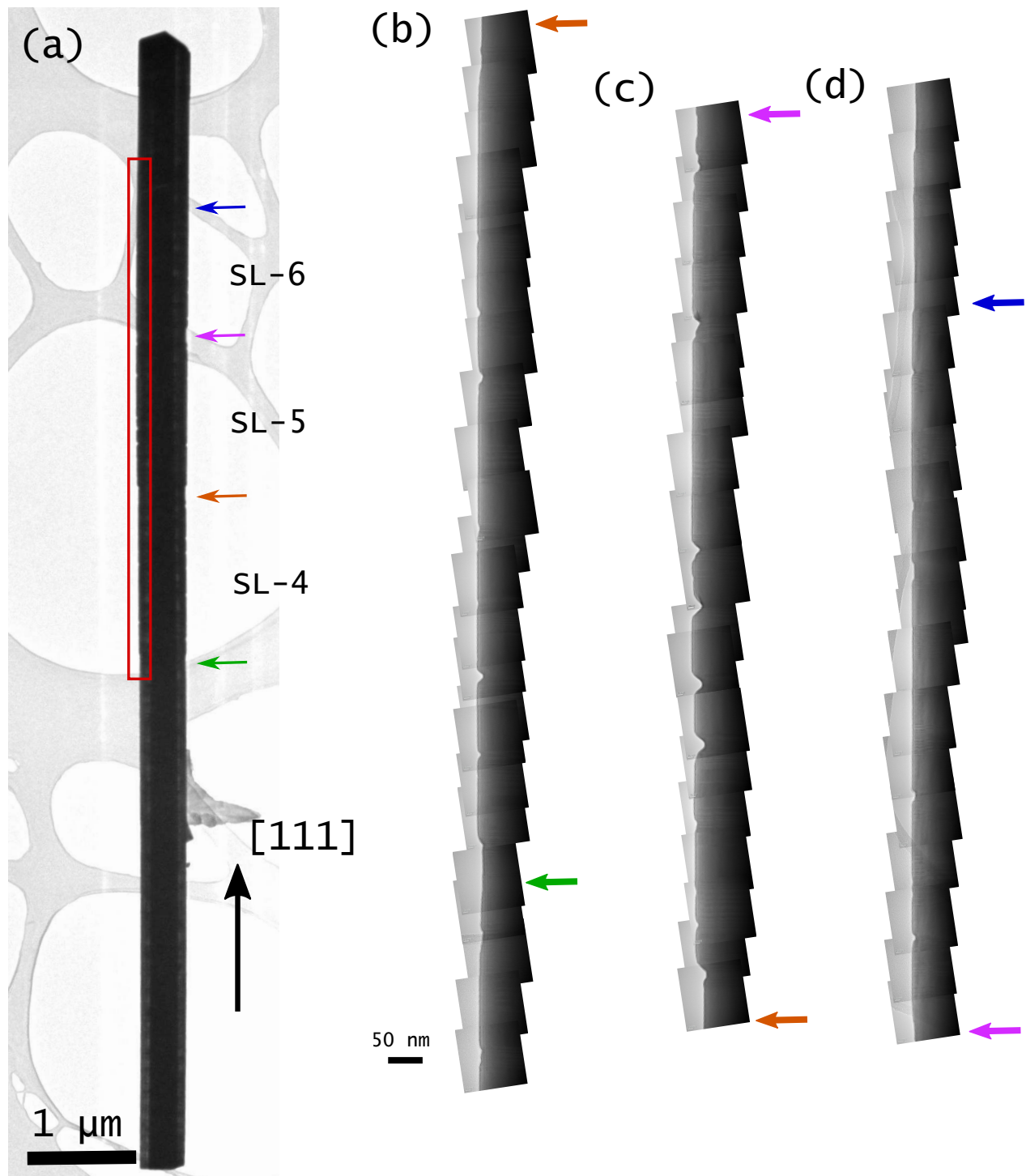
Figure B.2: (a) BF-TEM image of Sample B NW. (b)-(d) compilation of 64 HR-TEM images from area within red square in (a). (b) SL-4. (c) SL-5. (d) SL-6. Color coded arrows Black arrows indicate W3 (green), W4 (orange), W5 (purple) and W6 (blue).
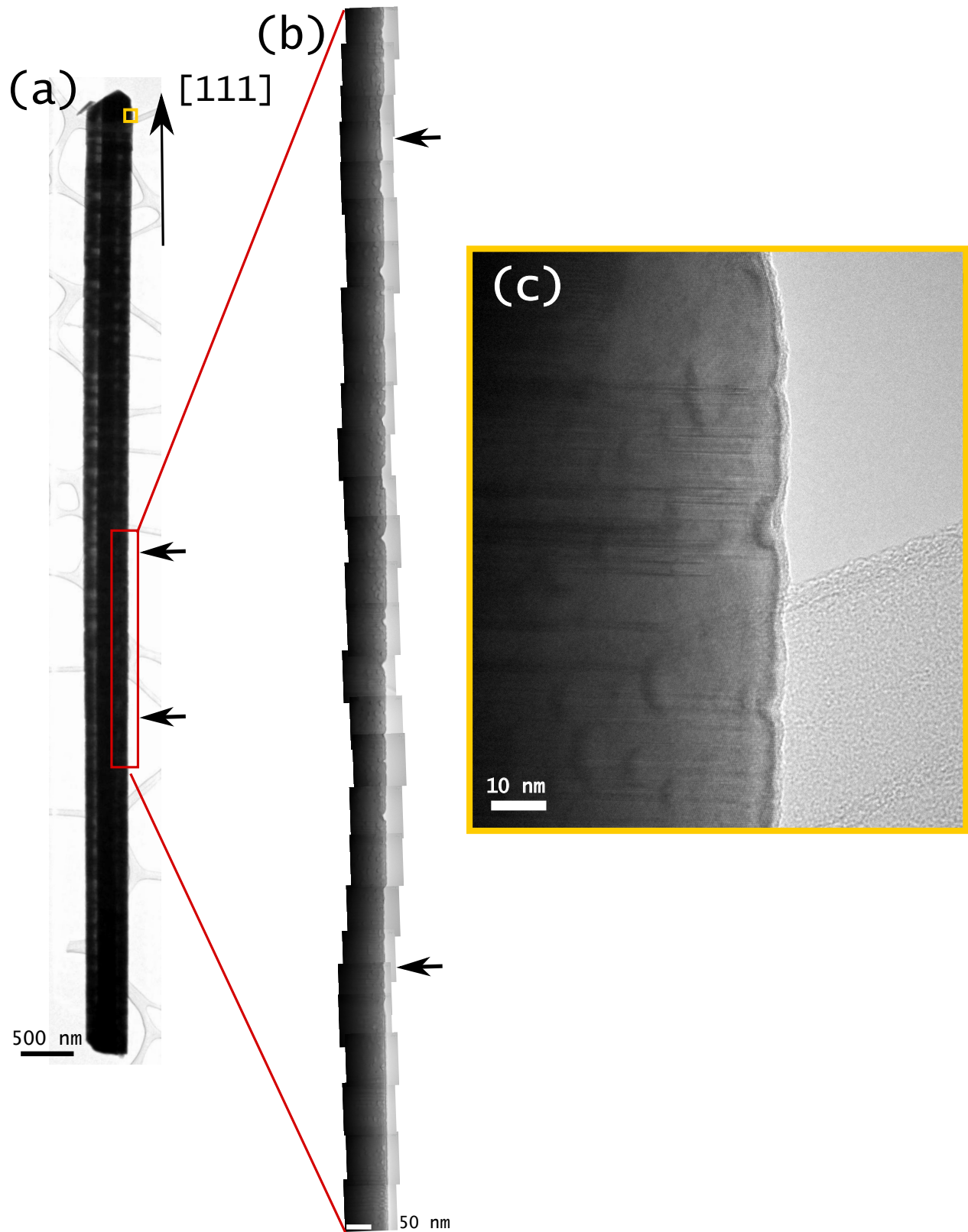
Figure B.3: (a) BF-TEM image of Sample C NW. (b) compilation of 28 HR-TEM images from area within the red square in (a). (c) HR-TEM image of the yellow square marked in (a). Black arrows indicate the start and end of SL-3.

Appendix C

EDS

Figure C.1 shows the results from EDS measurements of three different locations on a sample D NW, as indicated in insets (b) and (c) of the figure. The EDS measurements were taken on a spacer, a pure ZB phase insert and a larger pure WZ stretch near the NW tip, respectively marked as area 1, 2 and 3.
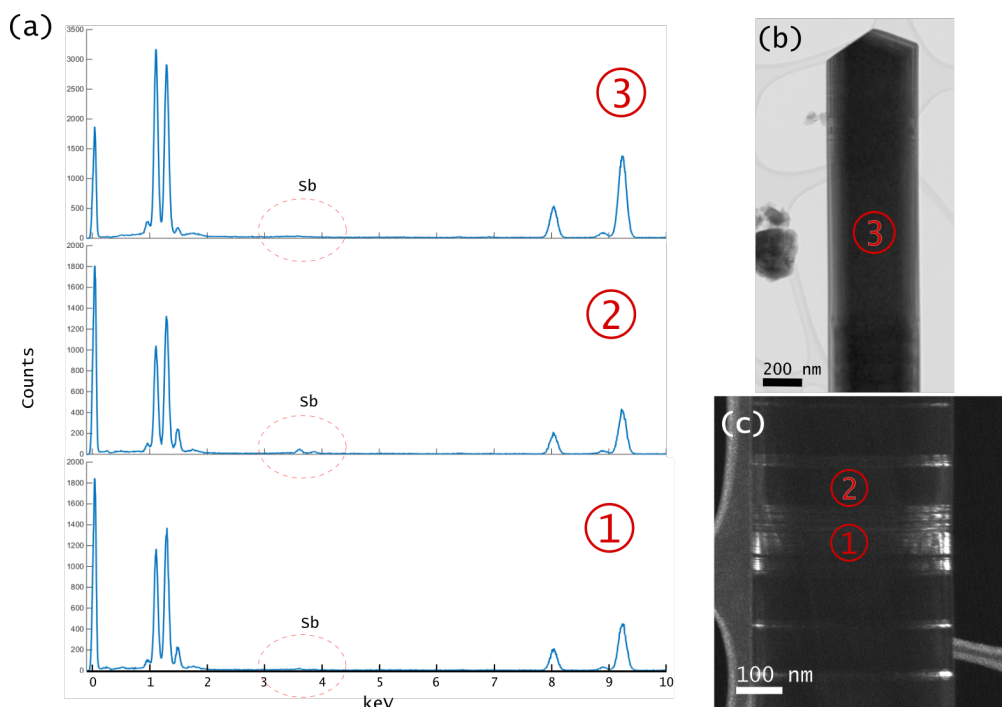
Figure C.1: EDS spectra from JEOL JEM-2100 TEM. (a) Energy vs counts of the EDS from regions 1, 2 and 3 indicated in (b) and (c). Region 1 is a WZ rich region, 2 ZB phase section and 3 a longer stretch of pure WZ phase.

Appendix D

STEM and EDS analysis of FIBed nanowires

Text by Antonius T. J. van Helvoort and Ingrid Marie Andersen.

To analyze the compositional variations within the nanowires, more elaborated TEM studies were done by PhD candidate Julie Stene Nilsen. The NWs were transferred from the substrate to a 50 nm thick SiN thin window TEM grid using a diamond scraper and isopropanol. Representative NWs were selected by conventional TEM using a JEOL JEM-2100F. To reduce beam broadening during EDS analysis, where the spatial resolution deteriorates, a TEM lamella was extracted from the center of a NW using focused ion beam (FIB) (FEI Helios NanoLab Dual-Beam). The prepared TEM lamellas were about 12 µm long and 100 nm thick, and included the entire NW laser. The specimens were characterized with HAADF STEM and EDS using a JEOL JEM ARM200F at 200 kV with a Centurio SDD EDS system (solid angle 0.98 sr). EDS data were acquired with the NW laser specimen on the [112] zone. EDS data analysis based on the Cliff-Lorimer method was performed using the Python based platform HyperSpy. Figure B1 depicts the 5th SL in sample B at the 112-zone ((a,b)) and tilted 15° from zone ((c,d)), imaged by HAADF STEM and BF STEM.

On zone the HAADF STEM images have a periodic contrast (Figure D.1(a)). Here atomic number contrast is expected to be dominant. For example, the AlGaAs passivation shell is clearly visible in the 112 orientation. On the upper side both AlGaAs shell and GaAs cap are visible. For BF STEM, with a similar contrast as would be present in BF TEM, some weak strain contrasts are visible on the 112-zone. As is show in Figure 4.16(b) in the report, in this orientation there is
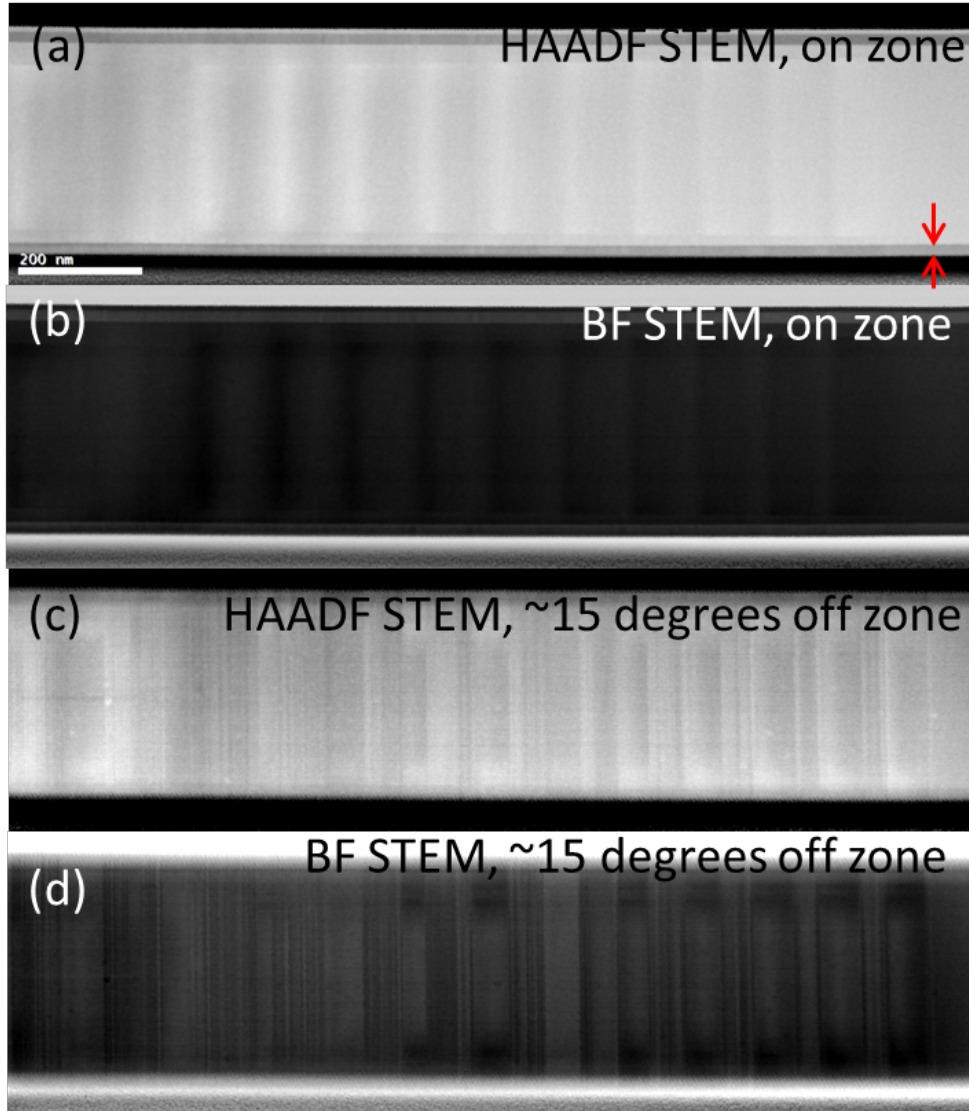
91

Figure D.1: SL-5 in sample B. (a) HAADF STEM and (b) BF STEM on 112-zone. (c) HAADF STEM and (b) BF STEM on tilted 15 degrees around [111] from 112-zone. The layer marked by arrows in (a) is the AlGaAs passivation layer.

hardly any contrast between the different crystal phases. However, if the NW is rotated around the 111-growth axis (i.e. off zone, however the interfaces between the different crystal phases still edge on), the variation in crystal phases become dominant in both HAADF (Figure D.1(c)) and BF (Figure D.1(d)) STEM. The irregular crystal distribution is similar to what is observed in conventional TEM reported in the main text.

EDS analysis across a SL shows a regular decrease in the As content and a corresponding increase in the Sb signal, whereas the Ga signal is about constant (Figure D.2(a)). This indicates

formation of GaAs$_{1-y}$Sb$_y$. There are ten maxima in the Sb signal. Between these wells (maxima) are barriers with a lower Sb content, although it seems not to be 0% as in the spacer (Left in Figure D.2(a)). This is more pronounced when only the Sb signal is plotted (Figure D.2(b)). Please note that the at.% values have a pronounced error, clearly notable for the GaAs spacer. The spacing between the maxima in Sb signal is 150 nm and except the first well, all wells have roughly the same maximum Sb composition. This is similar as the period observed in HAADF STEM at the 112-zone (Figure D.1(a)).
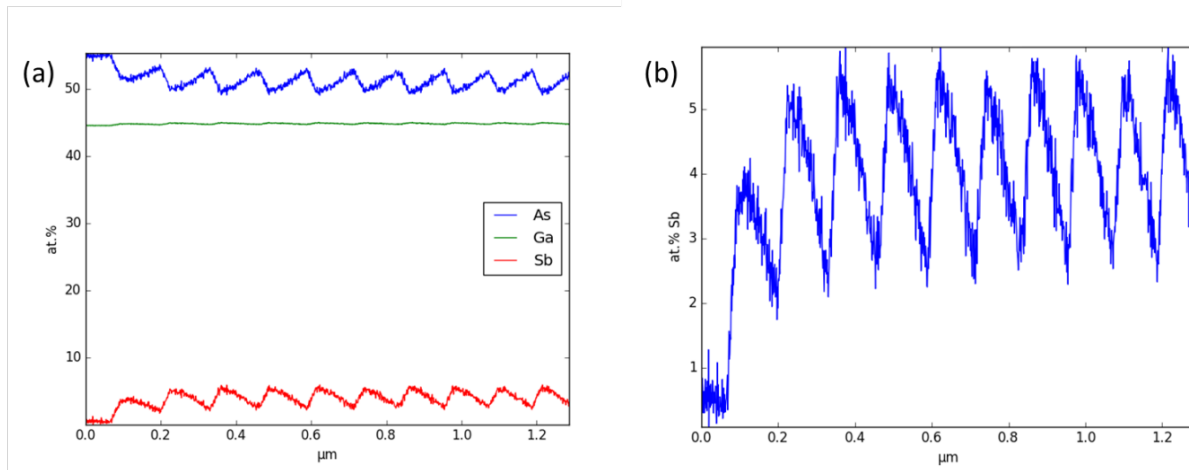
Figure D.2: EDS profiled over SL-5 in sample B. (a) Compositional plot based on Ga$_K$, As$_K$ and Sb$_L$ lines. (b) The Sb profile enlarged. The tip of the NW is toward the right.

The EDS profiles for all six SLs of all four NW samples were recorded and can be seen in Figure D.3. From this figure it is clear that sample A has the lowest Sb content and that the profile is very noisy. Sample D has the highest maxima and the most pronounced fluctuations. One can see that the first SL in all four samples is building up Sb % and is distinctly different from all other SLs. SL-2 is the most regular: the maxima are all similar, the minima in between might display a slight increase towards the tip. SL-3 to SL-5 in samples B, C and D have the same trend with a lower Sb content in the first well. SL-6 in B, C and D has a similar profile, but seems to have a slightly lower total length. What these profiles demonstrate is that between the different samples (except sample A) and for the different SLs (excluding SL-1) a similar profile is obtained. This indicates robust growth conditions in which the SB content can be tuned.
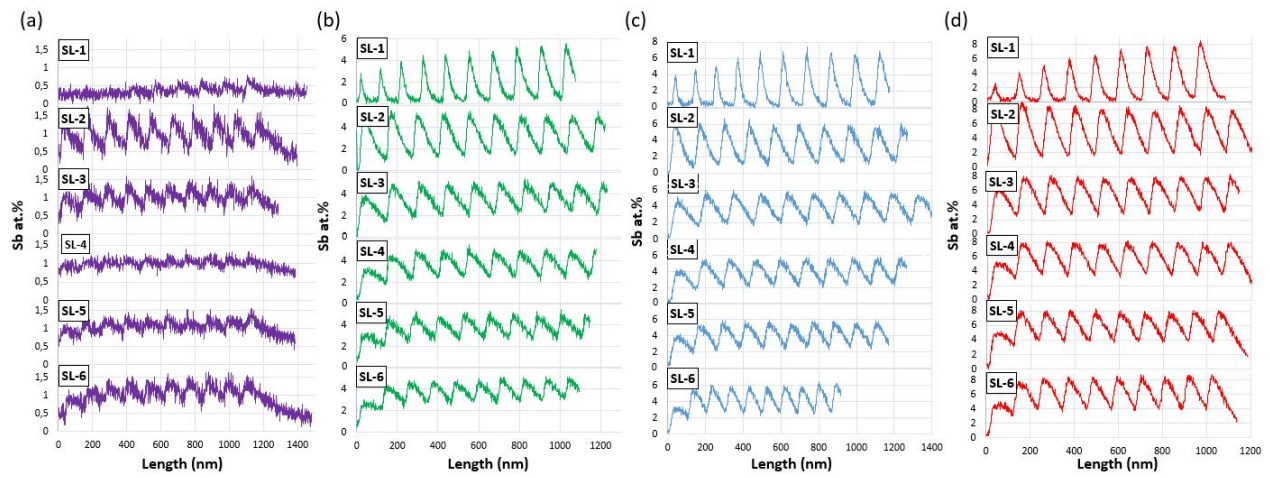
Figure D.3: EDS profiles for (a) sample A, (b) sample B, (c) sample C, and (d) sample D.

Appendix E

SEM and Optical measurements

Text by Ingrid Marie Andersen and Dingding Ren.

To test the lasing properties of the nanowires optical pumping and photoluminescence measurements were conducted of the NW samples by PhD candidates Dingding Ren and Lyubomir Ahtapodov. They recorded and analyzed the data. The NWs were transferred from the Si substrate to a 300 nm thick SiO_2/Si substrate by the use of a diamond scraper. A mode-locked Spectra Physics Tsunami Ti:Sapphire laser (300 fs pulses at 800 nm with 50% excitation power loss from the collective objective used) was used to optically pump the NWs, and the photoluminescence signal was dispersed by a spectrometer and then detected with an Andor Newton EMCCD camera.

Lasing was detected from all the NW samples (Figure E.1), with relatively small (ca. 100 nm) variations in emitted wavelength. Figure E.1 depicts the measured emitted wavelengths versus the intensity for the sample NWs for optical pumping above the lasing threshold. Generally, samples with higher Sb% emit light with a higher wavelength relatively samples of lower Sb concentration, with the exception of sample C. Compared to sample B, the spontaneous emission of sample C shows a longer wavelength at low pumping power, which indicate that the NW is of higher Sb content. By increasing the pumping power, however, we observed a more pronounced blue shift of the spontaneous emission in sample C before lasing, which is due to band filling effect at high pumping power. Considering also a relatively higher lasing threshold in general for sample C than sample B. This suggests that the sample B has better lasing performance than
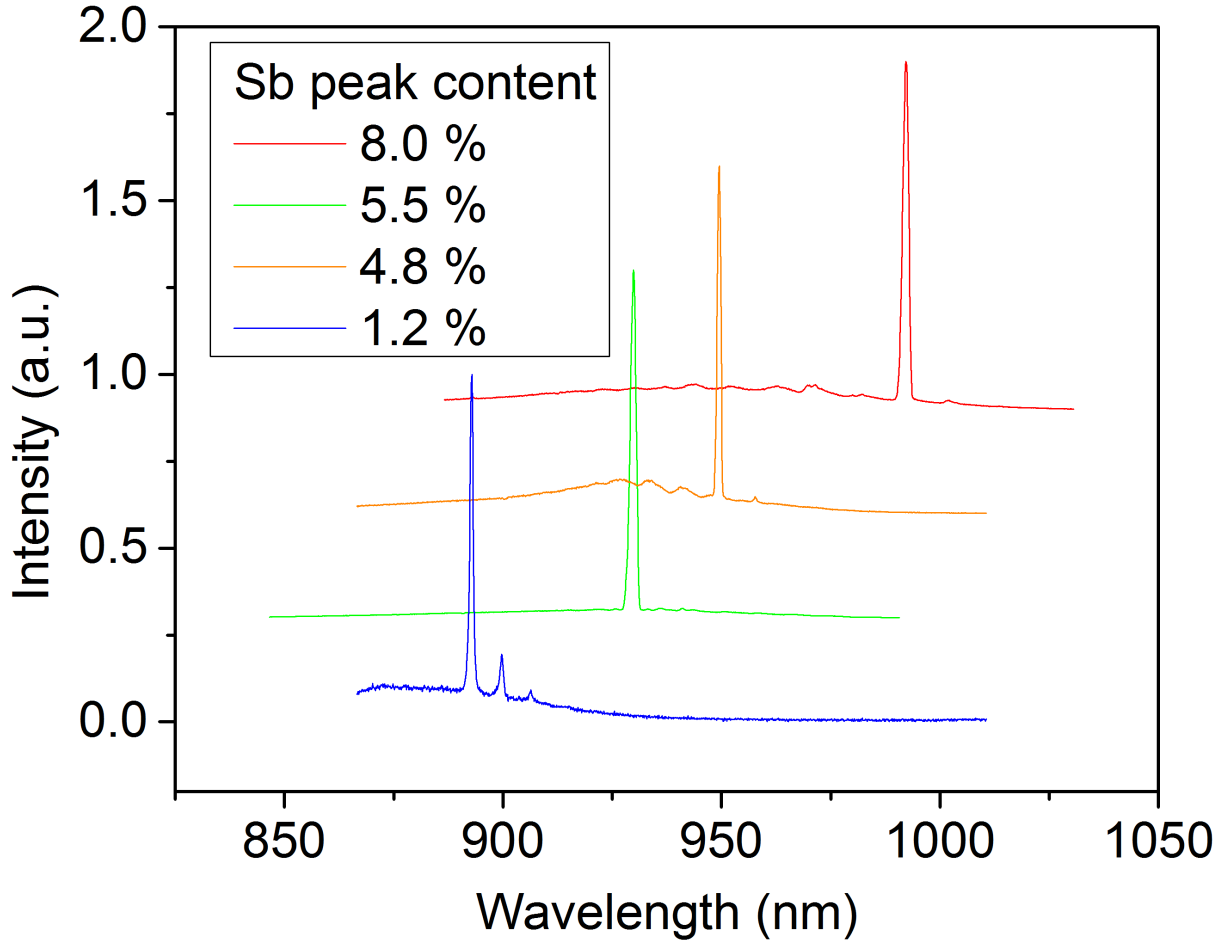
sample C. This is what is depicted in Figure E.1.

Figure E.1: Emitted lasing wavelength vs intensity for sample A (1.2% Sb), B (4.8% Sb), C (5.5% Sb), and D (8.0% Sb) above lasing threshold.

The NW samples were studied in the SEM by PhD candidates Dingding Ren. Figure E.2(a) show the tips of a sample B NW array, where one can clearly see how the NW tips have facets in certain planes. An image of the lasing sample B is depicted in Figure E.2(b). For sample B the lasing threshold is around mw/cm^2 of pumping power, which can clearly be seen from the plot in Figure E.2(c).
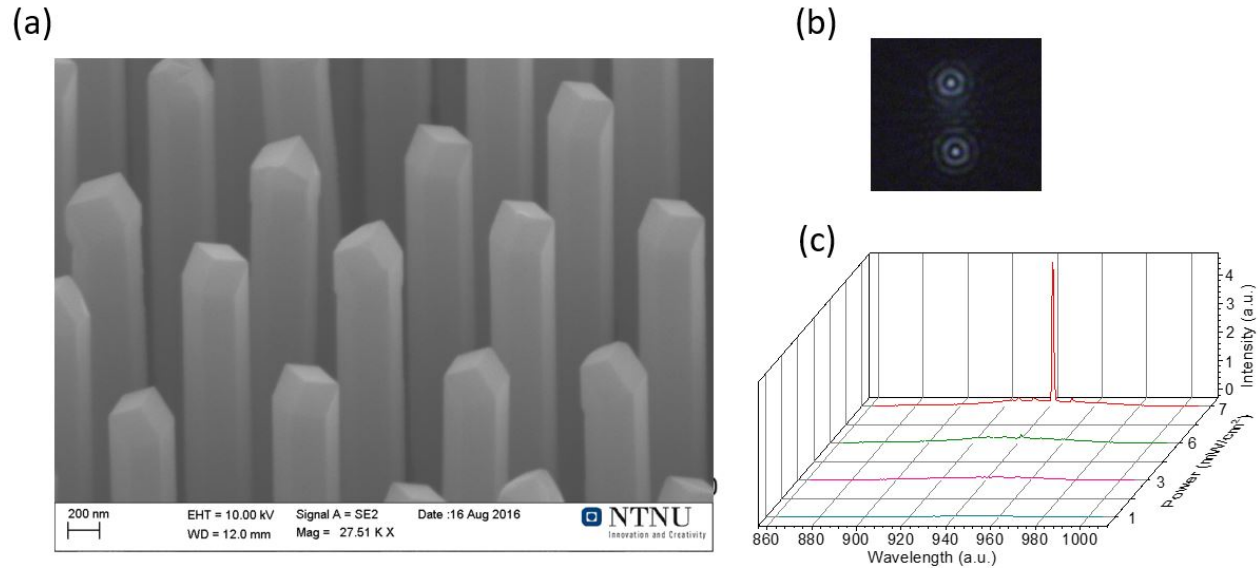
Figure E.2: (a) SEM image of array of NWs from sample B. Image is taken by PhD candidate D. Ren in the NTNU Nanolab. (b) image of a lasing sample B NW (c) The emitted wavelength vs intensity for increasing optical pumping power of sample B.

With the exception of sample C, these optical measuements show that this type of heterostructures NWs with GaAs/GaAsSb superlattices show lasing and that the emitted wavelength can be tuned by the Sb % of the NWs (i.e. the Sb flux or the growth time of GaAsSb inserts).

Appendix F

Scanning Precession Electron Diffraction

Text by Antonius T. J. van Helvoort and Ingrid Marie Andersen.

To test if the phase identification can be done via scanning precession electron diffraction (SPED) a test was done by Håkon Ånes and Antonius T. J. van Helvoort, who both recorded and analyzed the data. SPED was taken from SL-5 in sample D (the same TEM grid as used in main project). Data was collected with a Nanomega ASTAR system on a JEOL 2100F microscope. A 1 nm probe and 0.5° precession was used. Data processing was done in Python based platform HyperSpy and Nanomega's INDEX for template matching.

Figure F.1 depicts the virtual dark-fields (VDF) for ZB in two different orientations, and WZ. The virtual aperture was slightly too large, and consequently some WZ reflections were (partly) selected and appear in the ZB images. There is a this wedge at the very edge of the NW, where a diffraction pattern similar to a kinematic pattern can be obtained. In the thicker parts (ca. 400 nm) the pattern can still be extracted, by which the different phases/orientations can be distinguished, but here dynamical effects are apparent.
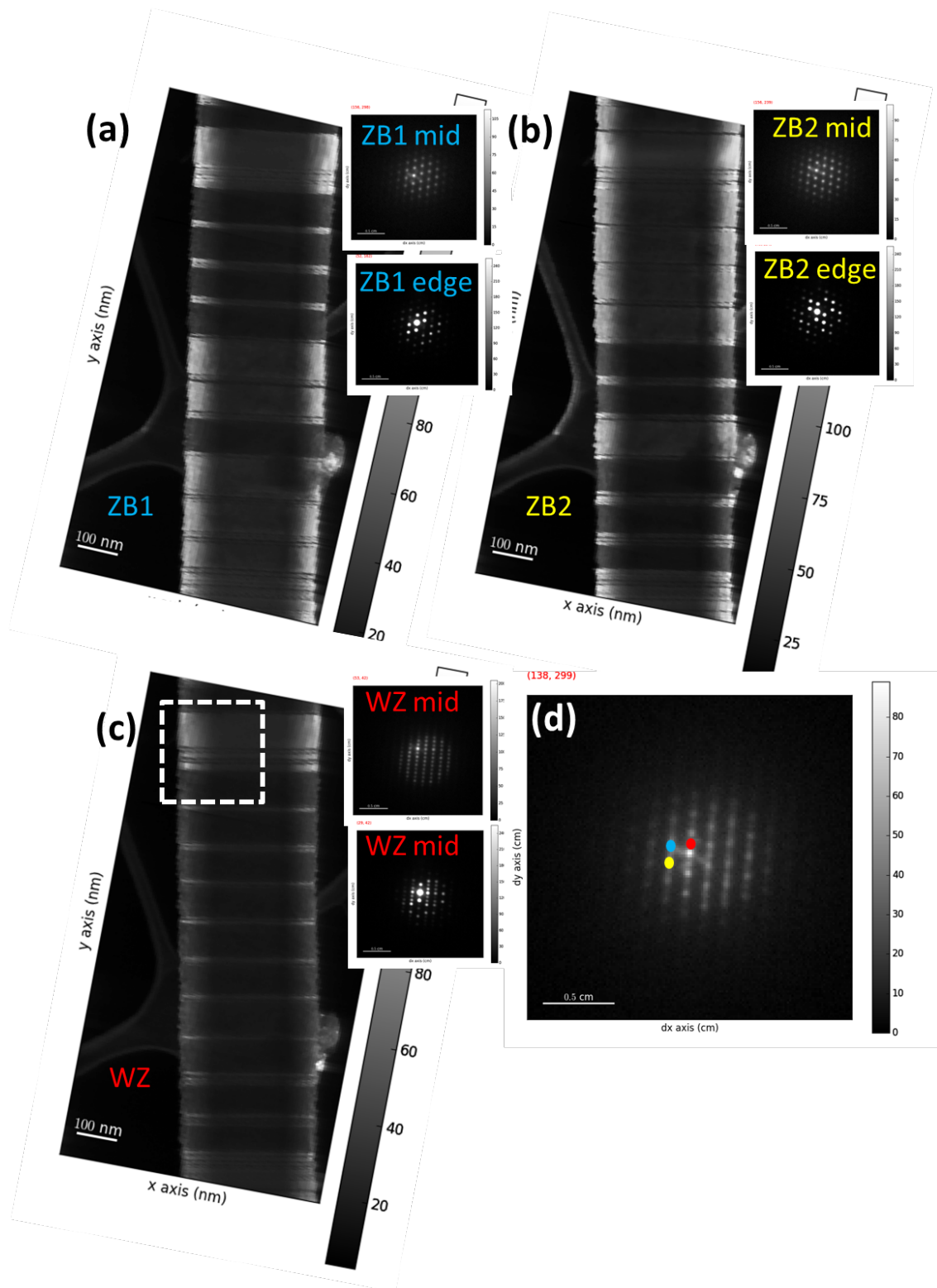
Figure F.1: SL-5 in sample D. VDFs of (a) ZB, (b) ZB twinned orientation and (c) WZ. The pattern from the marked area in (d) has the reflections marked from which (a-c) were constructed. The inserts in (a-c) marked patterns taken in the middle (thick) and on the edge (thin) of the nanowire.

The same data set is analyzed by template matching to a ZB and WZ GaAs DP bank. Figure F.2(a) depicts a BF TEM image where the analyzed region is marked by a red box. This area is a part of the set shown in Figure F.1 and was selected to reduce the data size (from ca. 1.6 to 0.8 Gb) and the template matching time (to ca. 2 hours). The reliability is defined as how well the best fit is compared to the second best fit. In this case, the reliability is poor (Figure F.2(c)), but the index (matching or fitting) score (Figure F.2(d)) is acceptable, with the exception of the WZ phase and the thicker regions within the wells. The phase map (Figure F.2(e)) does not depict the WZ parts and the WZ template bank has to be verified or a more extensive template matching routine should be attempted. The orientation maps (Figure F.2(f-h)) for ZB GaAs distinguish the different ZB segments in the Y-direction.
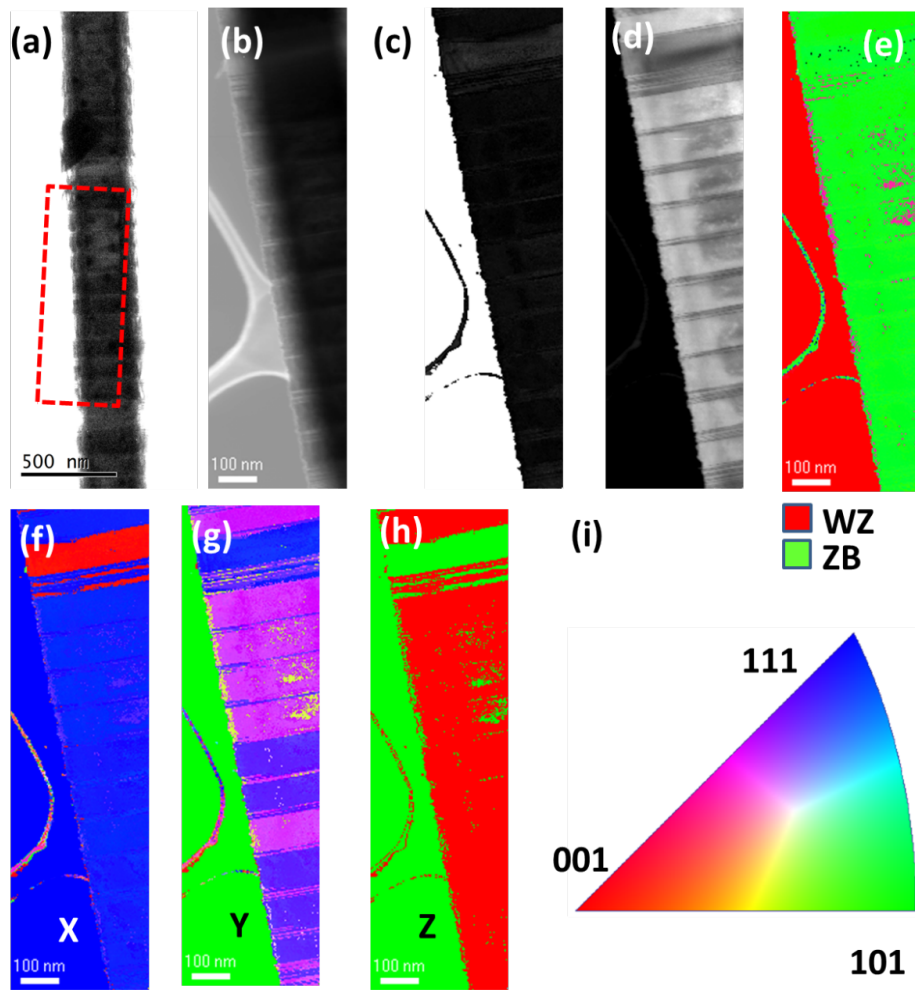

Figure F.2: (a) BF TEM with area SPED is taken marked. (b) Virtual bright-field, (c) reliability score, (d) Index score, (e) ZB-WZ phase map, (f-h) orientation maps for three directions labeled as shown in the inverse pole figure in (i).

The reduced data set for template matching was also analyzed by machine learning (no candidate phases given). This is computationally more intensive and hence only parts of the set were analyzed. In this case, non-negative matrix factor (NMF) was used with 5 components. The results are shown for the upper part of SL-5, which include a WZ spacer (Figure F.3) and a section from the middle where ZB is dominant and the C-foil support is included (Figure F.4).
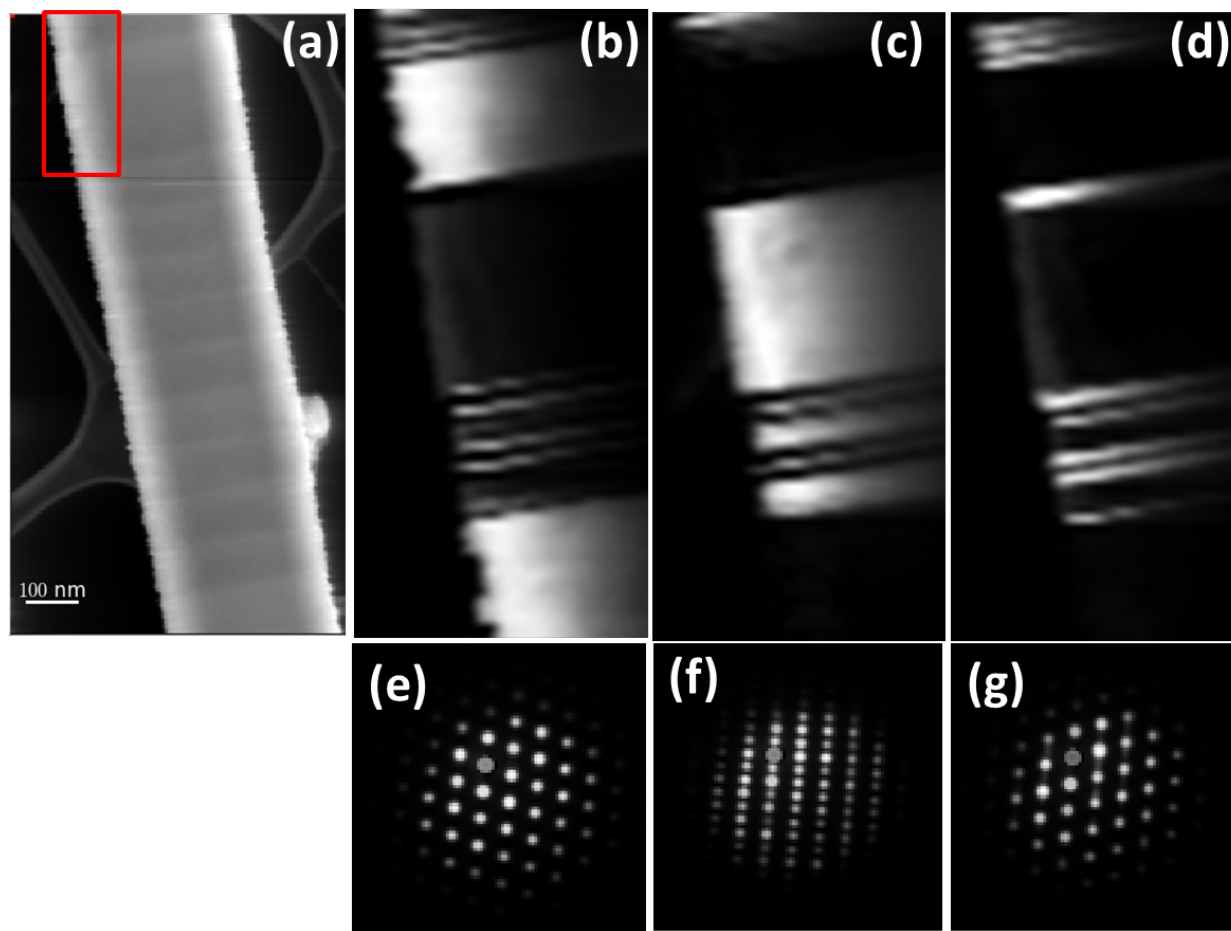

Figure F.3: (a) Intensity SPED data set/overview. Area in the top (b) loading map component 2, (c) loading map component 3, (d) loading map component 4 and (e-g) the corresponding components. The red box in (a) marks the selected region for the NMF analysis.
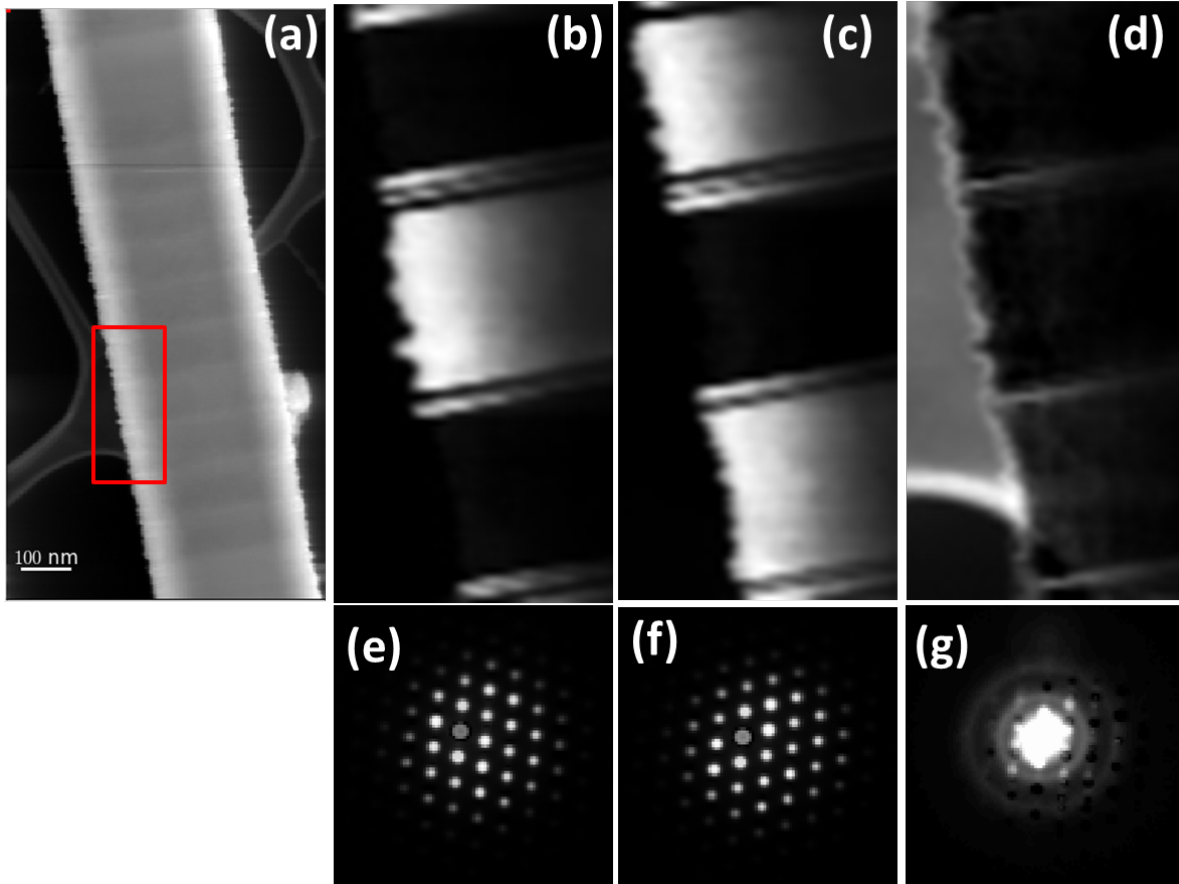
Figure F.4: (a) Intensity SPED data set/overview. Area in the middle (b) loading map component 2, (c) loading map component 3, (d) loading map component 4 and (e-g) the corresponding components. The red box in (a) marks the selected region for the NMF analysis.

These three ways to analysis the SPED data set demonstrate that phase mapping can be an alternative to conventional DF TEM, for both thin and thick areas. VDFs is a fast method which enables the used to come back to the data set to retrieve new information. Template matching with an extensive pattern bank is not really required for this simple case, with the NW on the 110-zone and hence three different candidate patterns, and the resolution is reduced. This is, however, an ideal case for machine learning. Compared to diffraction mapping (i.e. VDFs) the intensity and contrast in the loading (location) maps is better. Because of precession there are less intensity variations due to bending and thickness variations. This should help template matching and especially machine learning. However, all three methods need further refinement to reliably analyze the entire 10 um long NW. The storage and computational demand can currently cause problems.